Department of Physics and Astronomy

University of Heidelberg

Bachelor thesis

in Physics

submitted by

Kim-Louis Simmoteit

born in Munich

2017

Development of an X-Ray based Energy Calibration Method for High Voltage Monolithic Active Pixel Sensors

This Bachelor thesis has been carried out by

Kim-Louis Simmoteit

at the

Physikalisches Institut Heidelberg

under the supervision of

Prof. Dr. Andrè Schöning

Zusammenfassung

Das Mu3e-Experiment plant nach dem Leptonfamilienzahl verletztenden Zerfall $\mu^+ \to e^+e^-e^+$ zu suchen. Dieser Zerfall ist nach dem erweiterten Standard Modell durch Neutrino-Mischung mit einem Verzweigungsverhältnis kleiner als 10^{-54} möglich, jedoch nicht beobachtbar. Das Ziel von Mu3e ist es, mit einer Sensitivitẗ von 1 in 10^{16} Zerfällen ein solches Signal zu suchen. Wird das Ereignis detektiert, so weist dies eindeutig auf neue Physik hin.
Im Detektor zerfallen die Myonen in Ruhe, was eine Trennung des Zerfalls vom Untergrund mittels Impuls- und Energieerhaltung erlaubt. Hierbei ist die Energie eines entstehenden Teilchens auf 53 MeV beschränkt, wodurch Coulomb-Mehrfachstreuung den dominierenden Faktor bei der Impulsauflösung wird. Um diesen Effekt zu reduzieren und den Anforderungen des Experiments gerecht zu werden, ist ein sehr dünner, sowie schneller Pixelsensor erforderlich. Eine Technologie, welche diese Voraussetzungen erfüllt, sind hochspannungsbetriebene monolithischen aktiven Pixelsensoren (HV-MAPS).
In dieser Arbeit wird die Energiekalibration der Signalhöhe des HV-MAPS-Chips MuPix7 durch Röntgenstrahlung vorgestellt und diskutiert. Für die Kalibrierung wird zum einen die Endpunktsenergie des Bremsstrahlungsspektrums bei verschiedenen Anodenspannungen und zum anderen die K_α-Linien der Röntgenfluoreszenz diverser Metalle verwendet. Mit beiden Methoden ergeben sich übereinstimmende Kalibrationskurven. Mittels einer kombinierten Eichkurve ergibt sich eine Signalhöhe von 0.16 V für Elektronen des Myon-Zerfalls. Eine Möglichkeit zur Überprüfung der Kalibration wird mittels einer radioaktiven Eisen-55 Quelle vorgestellt.

Abstract

The Mu3e experiment plans to search for the charged lepton flavour violating decay $\mu^+ \to e^+e^-e^+$. This decay can be mediated in the extended standard model via neutrino mixing but is heavily suppressed to a very small branching ratio of less than 10^{-54}. The goal of the experiment is to achieve a sensitivity of 1 in 10^{16} decays. Detection of such an event would be a clear sign for new physics beyond the standard model.
In the detector, the muons are stopped and decay at rest, which allows a separation of signal decays from background via momentum and energy conservation. The maximum energy of 53 MeV of the decay electrons leads to multiple Coulomb-scattering dominantly limiting the momentum resolution in the reconstruction. To reduce the influence of this effect and fulfil the requirements of the experiment, a very thin and fast pixel sensor is needed. For this purpose, High Voltage Monolithic Active Pixel Sensor (HV-MAPS) will be used as pixel sensors.
In this thesis, an energy calibration via X-rays of the HV-MAPS based prototype MuPix7 is presented and discussed. The calibration is performed on the one hand by using the endpoint of the continuous X-ray spectrum at different anode voltages. And on the other hand by using the characteristic K_α-lines from X-ray fluorescence of various metals. With both approaches similar results are achieved. A combined calibration curve yields an expected signal height of 0.16 V for electrons from the signal decay. In addition, the calibration curves are validated using an Fe-55 source.

Contents

Table of Contents 5

I Introduction & Theory 9

1 Introduction 10

2 The Mu3e-Experiment 11
2.1 Theory . . . 11
2.1.1 Standard Model . . . 11
2.1.2 Muon Decay . . . 12
2.2 Signal Decay Characteristics . . . 13
2.3 Background . . . 13
2.4 Detector Concept . . . 14

3 Interaction of Particles with Matter 17
3.1 Photons . . . 17
3.2 Charged Particles . . . 18
3.3 Multiple Coulomb Scattering . . . 21

4 Introduction to X-Rays 22

5 Semiconductor based Pixel-Detectors 24
5.1 Semiconductor Physics . . . 24
5.1.1 Semiconductors . . . 24
5.1.2 pn-junction . . . 25
5.1.3 Signal Detection . . . 27
5.2 HV-MAPS Pixel Sensor . . . 27

II Experimental Setup 29

6 MuPix Sensor 30
6.1 Pixel Electronics . . . 30
6.2 Digital Part . . . 31
6.3 Pulse-Shaping . . . 31

7 Lab Setup **34**
7.1 Single Setup . . . 34
7.1.1 PCB . . . 34
7.1.2 Software . . . 34
7.2 X-Ray Source . . . 35

III Methods **39**

8 Measuring Methods **40**
8.1 Measured Quantities . . . 40
8.1.1 Time-Over-Threshold . . . 40
8.1.2 Digital Hit Information . . . 40
8.2 Measurement Process . . . 40
8.2.1 Threshold Scan . . . 40
8.3 Signal Sources . . . 42
8.3.1 X-Rays . . . 42
8.3.2 Iron-55 Source . . . 43
8.3.3 Injection . . . 43

IV Measurements & Results **45**

9 Energy Calibration with X-Ray Endpoint-Energies **46**
9.1 General Curve Inspection . . . 46
9.2 Influence of Tuning . . . 47
9.3 Baseline Shift Due To Noise Tuning . . . 48
9.4 Calibration . . . 52
9.5 Investigation on Energy-Saturation . . . 53
9.6 Absorption Studies . . . 54
9.7 Calibration Fit . . . 57

10 Energy Calibration with X-Ray Fluorescence **60**
10.1 Curve Characteristics . . . 60
10.2 Background Estimation . . . 61
10.3 Fluorescence Calibration . . . 62
10.4 Calibration Fit . . . 64

11 Comparison of Methods **68**
11.1 ToT-Histograms . . . 68
11.2 Calibration Curves . . . 69
11.3 Combined Calibration . . . 69
11.4 Validation . . . 72

V Discussion 75

12 Summary & Discussion 76
12.1 Summary . . . 76
12.2 Discussion . . . 76
12.3 Outlook . . . 77

VI Appendix 79

13 Appendix 80
13.1 Properties of Silicon . . . 80
13.2 DAC-Values . . . 80
13.3 MuPix Measurement Settings . . . 81
13.4 Materials for X-Ray Fluorescence . . . 82
13.5 Prefits . . . 82
13.6 Mean Free Path in Silicon . . . 83

14 Bibliography 85
14.1 List of Figures . . . 90
14.2 List of Tables . . . 93

Part I

Introduction & Theory

1 Introduction

The Standard Model of Particle Physics (SM) is the main choice of explaining the composition of our universe. Over years, theoretical predictions were experimentally proven and new particles discovered, which made the standard model more and more consistent. Still lot of physical phenomena can't be explained with help of the SM. Therefore, new physics theories evolved to cover the understanding of such processes, which have mostly not been verified experimentally yet. A possible way to search for physics beyond the SM is the usage of high rate experiments, used to detect rare decays. The Mu3e experiment is such an experiment in the high rate sector, trying to determine a branching ratio of the charged Lepton Flavor Violating Decay (cLFV) $\mu^+ \to e^+ + e^- + e^+$ within a sensitivity of 10^{-16} with 90% Confidence Level (CL). To realize this experiment in a practical time, a muon beam is needed, which is capable of $2 \cdot 10^9$ muons per second. Therefore, Mu3e is carried out at the Paul Scherer Institut (PSI), where a high intensity muon beamline is planed and a muon beam with 10^8 muons per second is currently available. To achieve the desired sensitivity, detector concepts with precise vertex and timing resolutions and background suppression have to be used. Due to the low momentum decay products, multiple Coulomb scattering is significantly affecting vertex and momentum resolution. For keeping scattering influences low, the detector is designed to be as thin as possible, which can be fulfilled by the HV-MAPS technology.

HV-MAPS are monolithic semiconductor pixel detectors collecting charge via drift in a thin depletion zone. The process allows to place the readout directly in the pixel and reduce material budget a lot. Including the metal layers the chip can be thinned down to about 50 µm. The currently available HV-MAPS sensor prototype is the MuPix7, which has already been characterized in many aspects in previous studies. A characteristic value to compare pixel detectors is the number of electrons for a given signal and threshold. For the determination of this value, an energy calibration of the signal heights has to be done. Yet, only energy calibrations for the Time-over-Threshold (ToT) were done for the MuPix7 in [1], [2]. The aim of this thesis is to achieve an energy calibration curve for signal heights. X-rays are the method of choice due to a variety of well defined energies over a wide range. With X-ray fluorescence and endpoint energies from Bremsstrahlung spectra, two different calibration approaches have been used and compared to iron-55.

2 The Mu3e-Experiment

The search for charged Lepton Flavor Violating Decays (cLFVs) started in the 1950s. Since then, several experiments [3] tried to find such events through decays of muons. Until today, no hints on detected cLFVs were found, but excluding limits could be determined. A more precise search for a cLFV is planned by the Mu3e experiment, which searches for the decay $\mu^+ \to e^+ + e^- + e^+$ with a desired sensitivity of 10^{-16} Branching Ratio (BR) and 90% CL. In the following, the concepts and theory behind Mu3e are presented.

2.1 Theory

2.1.1 Standard Model

The Standard Model of Particle Physics (SM) describes the elementary particles and the fundamental forces. Every particle is individually defined and identifiable through its properties, i.e. its mass, charge, spin and several other quantum numbers. A schematic overview of all particles is given in Figure 2.1.
All particles can be classified in two groups via their spin quantum number S, meaning in fermions, particles with a half-integer spin and bosons, particles with an integer spin. Fermions are subdivided into six quarks and six leptons with respectively corresponding anti-particles. The interaction between fermions are mediated by three forces and their related particles, the gauge bosons:

- electromagnetic force (γ)
- weak force (Z, W^+ and W^-)
- strong force (gluons)

The last particle not covered is the higgs boson, which was a missing piece until its discovery in 2012 [5]. Albeit its apparent consistency, the SM still cannot explain many physical phenomena. Therefore, the standard model can be extended by new particles and physics like neutrino oscillations. Neutrino oscillation has already been observed by multiple experiments like Super-Kamiokande [6]. With this discovery at least two of the neutrinos were proposed to have masses, which implies the possibility of the violation of lepton flavor conservation. Even cLFVs are possible via neutrino oscillation but with the addition of a very unlikely decay caused by enormous small branching ratios. With physics beyond the standard model, higher branching ratios for cLFVs are predicted. The next step is therefore to search for cLFVs experimentally. For investigations of this type muons are preferred due to

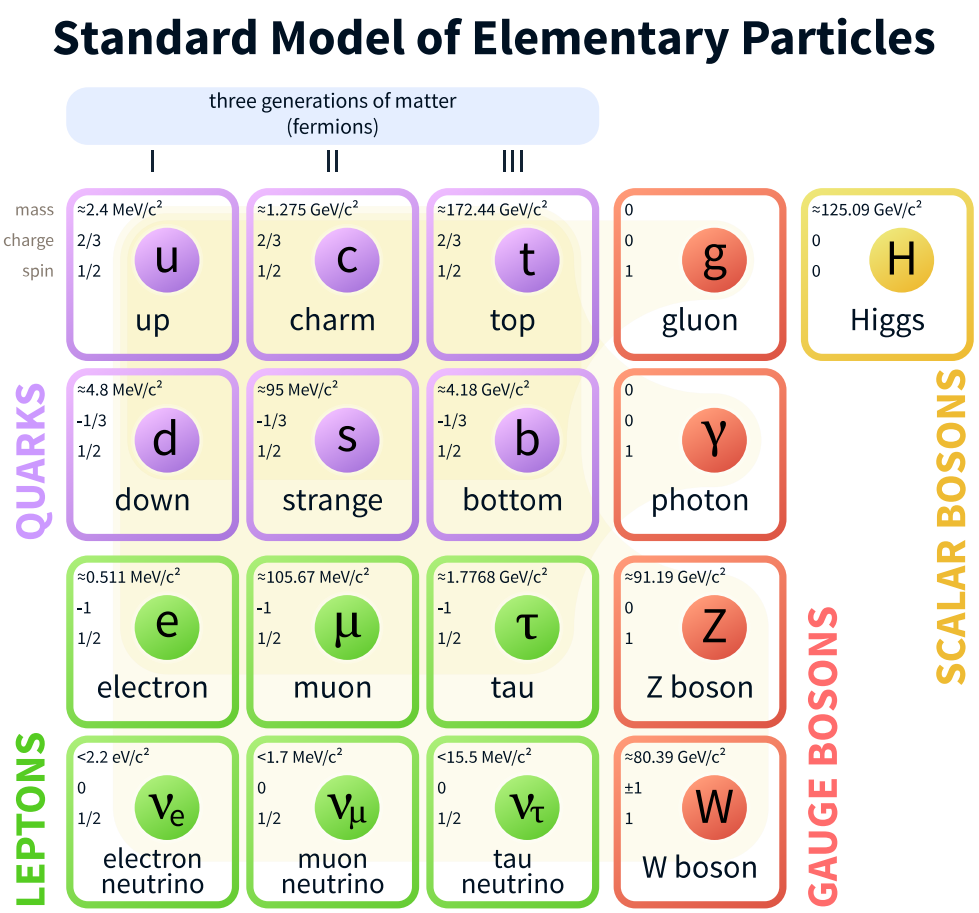

Figure 2.1: Table of elementary particles in the Standard Model [4]

their small mass compared to the tauon, which can decay to non leptonic particles, for instance hadrons. Furthermore, muons are easily available at high rates.

2.1.2 Muon Decay

The SM provides few possible decay modes for muons [7], with the most dominant decay mode being the Michel decay: $\mu^+ \rightarrow e^+ + \nu_e + \overline{\nu_\mu}$. Along the Michel decay, a muon can create an additional photon during the decay process, the so called radiative decay: $\mu^+ \rightarrow e^+ + \gamma + \nu_e + \overline{\nu_\mu}$. Radiative decays have a branching ratio of roughly 1.4% [8]. For even higher energies of the muon, the photon of the radiative decay decays into an electron-positron pair $\mu^+ \rightarrow e^+ + e^- + e^+ + \nu_e + \overline{\nu_\mu}$. Respective decays for μ^- can be derived from the decays listed above with usage of the corresponding anti-particles. In the extended standard model further decays are possible via neutrino oscillation, which can also break the conservation of lepton flavor. An exemplary decay is $\mu^+ \rightarrow e^+ + e^- + e^+$, which is not visible due to a branching ratio of $< 10^{-54}$. The Feynman diagram of such a decay can be found in Figure 2.2.

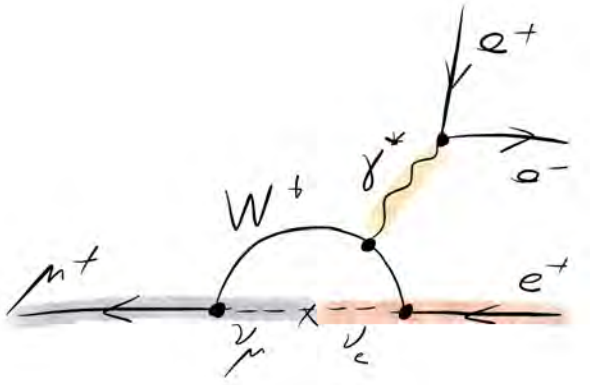

Figure 2.2: SM Feynman graph of muon decay via neutrino oscillation

However additional decay modes are predicted with even higher branching ratios using physics beyond the standard model, but were not detected yet. Experiments like MEG and Mu3e ([3]) try to set excluding branching ratios or even better find the signal for decays of $\mu^+ \to e^+ + \gamma$ or $\mu^+ \to e^+ + e^- + e^+$ respectively, which would indicate new physics beyond the SM.

2.2 Signal Decay Characteristics

The decay of a muon into three electrons $\mu^+ \to e^+ + e^- + e^+$ shares one vertex. Therefore, applying momentum conservation result in a total momentum $|\vec{p_{tot}}|$ of zero in the muons center of mass system.

$$|\vec{p_{tot}}| = |\sum_{i=1}^{3} \vec{p_i}| = 0 \tag{2.1}$$

Since the muon decays at rest, the total energy E_{tot} of the electrons has to be equal to the muon mass ($m_\mu \approx 105.658\,\mathrm{MeV}$, [8]) to satisfy energy conservation:

$$E_{tot} = \sum_{i=1}^{3} E_i = m_\mu c^2 \tag{2.2}$$

Momentum conservation limits the energy range of a single electron E_e to:

$$m_e c^2 \leq E_e \leq \frac{m_\mu}{2} c^2 \approx 53\,\mathrm{MeV} \tag{2.3}$$

2.3 Background

Not only the signal itself but also background can generate events in the detector. The understanding and suppression of background is therefore crucial to distinguish fake events. The Mu3e-Experiment has to deal with two groups of background:

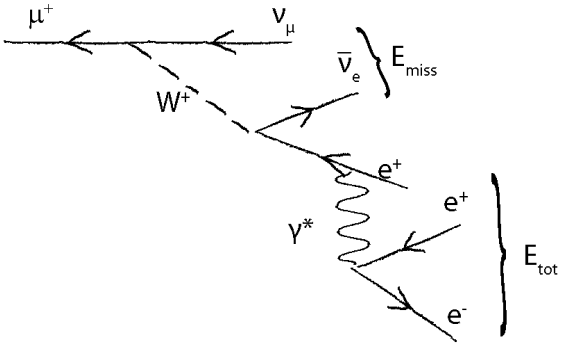

Figure 2.3: Feynman graph of internal conversion.

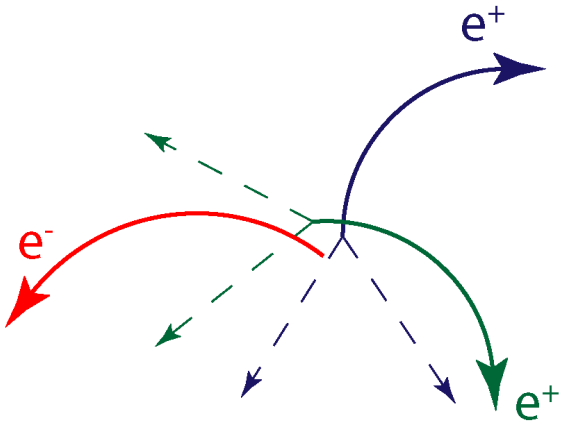

Figure 2.4: Combination of Michel decay and electron.

Internal Conversion: Irreducible physics background is produced by the decay $\mu^+ \rightarrow e^+ + e^- + e^+ + \nu_e + \overline{\nu_\mu}$, pictured in Figure 2.3. Due to the creation of neutrinos, which are not detectable in Mu3e, the total energy and momentum of the electrons is lower than the expectations from the signal decay. To achieve the desired sensitivity for the branching ratio of 10^{-16} at a confidence level of 90%, a energy resolution better than 1 MeV is needed [9].

Combinatorial Background: Decay products of different decays can fake signal events, illustrated in Figure 2.4. For instance, electrons from Michel decays, Bhabha scattering and radiative decays can look together as they are coincident in time, despite having a complete different origin. Also, wrong reconstruction of tracks can generate fake events. Due to the high rate of the muons this background has a significant influence in the experiment. To filter random background, a good temporal and spacial resolution and also low detector noise is important.

2.4 Detector Concept

The concept of the detector for Mu3e Phase I can be found in Figure 2.5. Muons with a rate up to $2 \cdot 10^8$ particles per second are stopped at a hollow double cone target and decay at rest. The charged decay products perform helix trajectories through an applied external solenoidal magnetic field with field strength of 1 T. Several cylindrical detection layers are placed around the target, which the decay products have to pass. The inner and outer double pixel layers are used for precise vertexing and momentum measurements. Additional layers of scintillating fibres in between are giving detailed time information and suppressing combinatorial background. Through the high magnetic field particles can recurl back and hit secondary recurl pixel and scintillating tile layers, improving the momentum detection and tim-

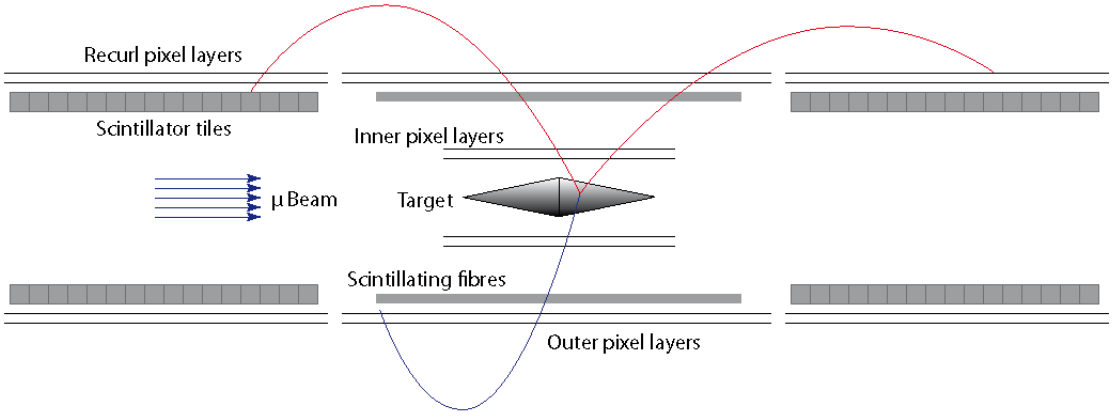

Figure 2.5: Detector concept for the Mu3e experiment

ing resolution. Due to the low momentum electrons having to pass several layers, multiple Coulomb scattering is the dominating effect in the Mu3e detector. Therefore, the detector layers are designed to be as thin as possible, which can be achieved through usage of HV-MAPS and Kapton® foil. Helium is used as cooling medium because of its low multiple scattering attribute.
The experiment is divided into two phases because a muon beam with the required rate is currently not existent at the PSI (Figure 2.6), but planned. Therefore, protons from πE5-beam have to be used to generate muons for Phase I. Protons hit a carbon target and creat pions, which are instantly decay into muons. This results in muons with a momentum of 23 MeV/c and a rate of 10^8 muons per second. Phase II uses the planned High intensity Muon Beamline (HiMB), which provides more than $3 \cdot 10^9$ muons per second, enough for the intended sensitivity of Mu3e.

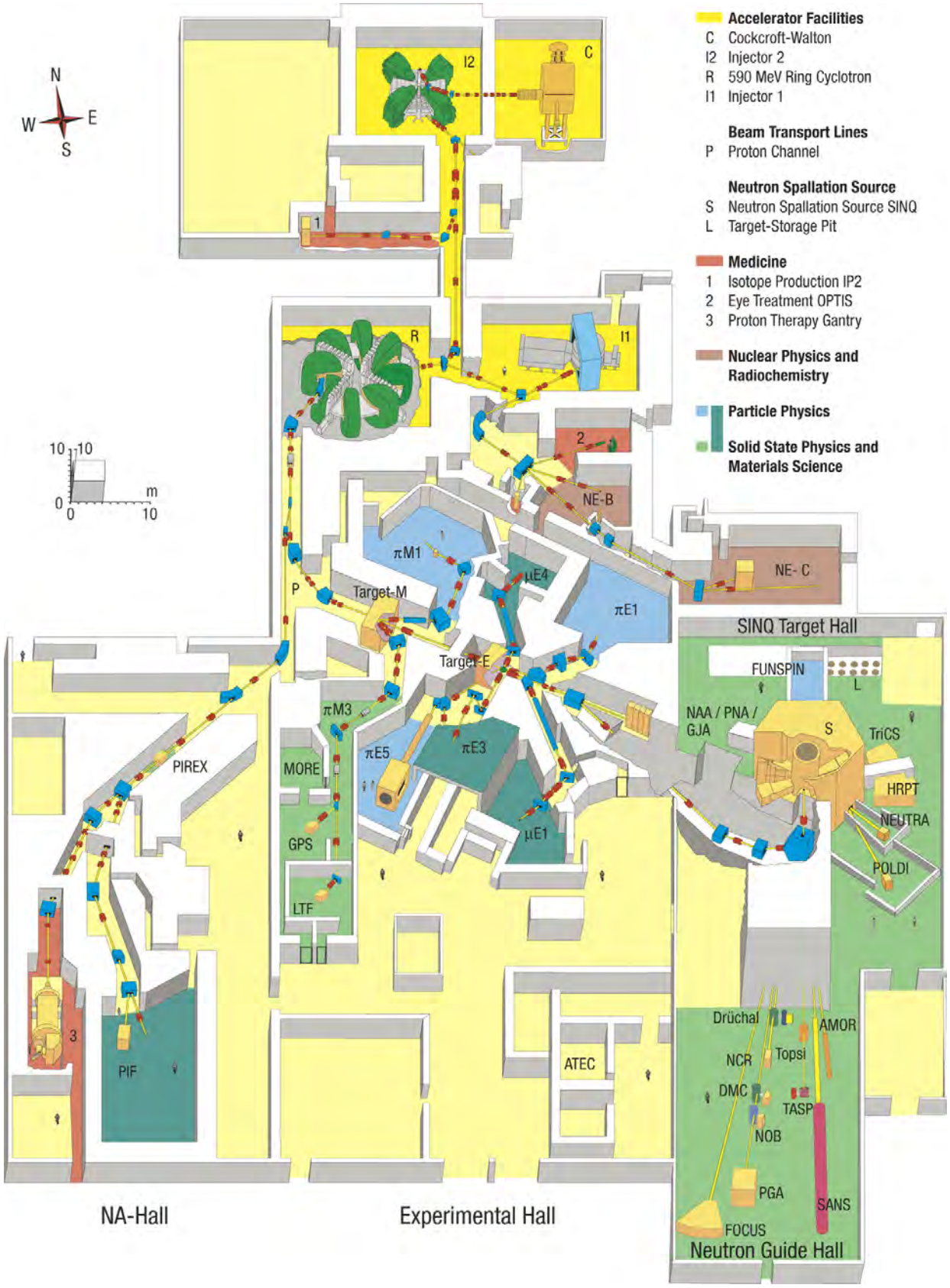

Figure 2.6: Experimental hall of the PSI with the πE5 beam.

3 Interaction of Particles with Matter

Different particles interact in many possible ways with matter. The most basic interactions needed for the Mu3e experiment and the energy calibration measurements are listed below.

3.1 Photons

The interaction of photons with matter is described by three important effects [10]:

Photoelectric Effect: When a photon with energy E_{Ph} hits matter, it can be fully absorbed by an electron inside an atom shell. The gathered energy is used to overcome the binding energy W of the material and if the energy is high enough, a photo-electron is ejected and obtains kinetic energy from the leftover energy.

Compton Scattering: Compton scattering describes the scattering process of photons at quasi-free electrons. Quasi-free electrons are, for instance, electrons bound inside atom shells. During the scattering process the photon loses energy and both particles proceed in different directions.

Pair Creation: If a photon has energy higher than two times the mass of electron m_e, the photon can decay into a electron positron pair. Pair creation is only possible with an additional particle which holds the recoil momentum.

The total cross-section σ_{tot} is the sum of all single cross-sections for different photon interactions. Single cross sections for silicon are shown in Figure 3.1, cut to the used energy range in this thesis. As visible, the dominant contribution is given by the photo electric absorption, whereas other effects like pair creation are negligible. The intensity I of a γ-beam with particle density n passing through a target has the following dependency to the thickness x [10]:

$$I(x) = I_0 \cdot \exp^{-n\sigma_{tot}x} \tag{3.1}$$

The inverse of $n\sigma_{tot}$ is also known as the attenuation length λ

$$\lambda = \frac{1}{n\sigma_{tot}} \tag{3.2}$$

which is describing the mean free path at which the intensity of the beam has dropped to $1/e$.

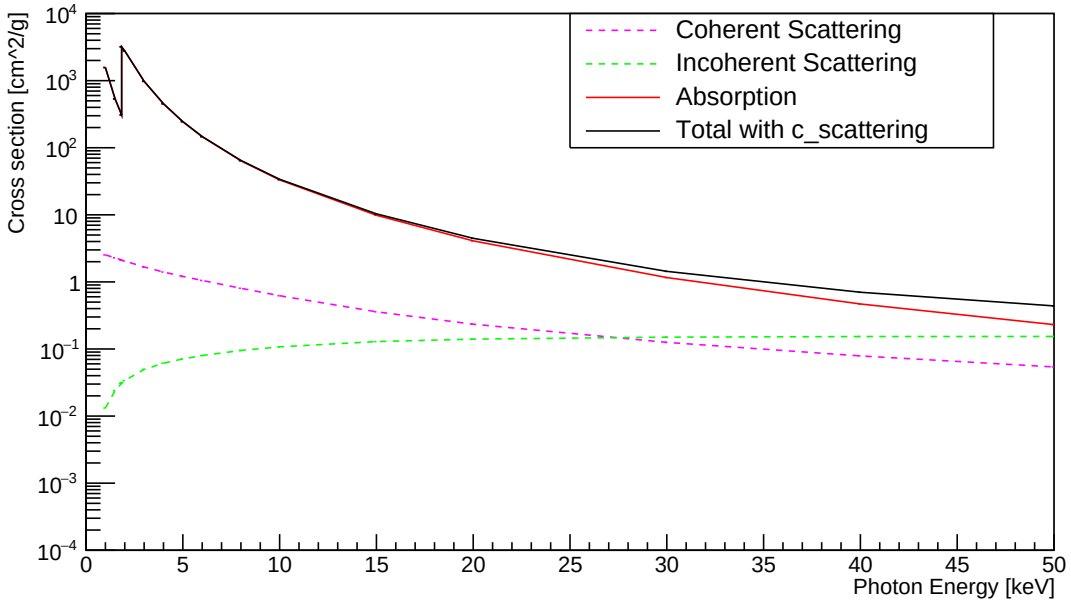

Figure 3.1: Photon cross sections in silicium, based on data of [11]

.

3.2 Charged Particles

Heavy charged particles are losing their energy while passaging through matter mainly through ionisation, as it is described by the Bethe-Bloch formula [12]:

$$-\langle\frac{\mathrm{d}E}{\mathrm{d}x}\rangle = \frac{4\pi n z^2}{m_e c^2 \beta^2} \cdot (\frac{e^2}{4\pi\epsilon_0})^2 \cdot [ln(\frac{2m_e c^2 \beta^2}{I \cdot (1-\beta^2)}) - \beta^2] \tag{3.3}$$

- $\langle\frac{\mathrm{d}E}{\mathrm{d}x}\rangle \rightarrow$ mean energy loss per material thickness
- $c \rightarrow$ speed of light
- $\beta = \frac{v}{c} \rightarrow$ velocity relative to speed of light
- $m_e \rightarrow$ mass of the electron
- $z \rightarrow$ charge of particle
- $n \rightarrow$ electron density of the material
- $\epsilon_0 \rightarrow$ vacuum permittivity
- $I \rightarrow$ mean excitation energy of the material

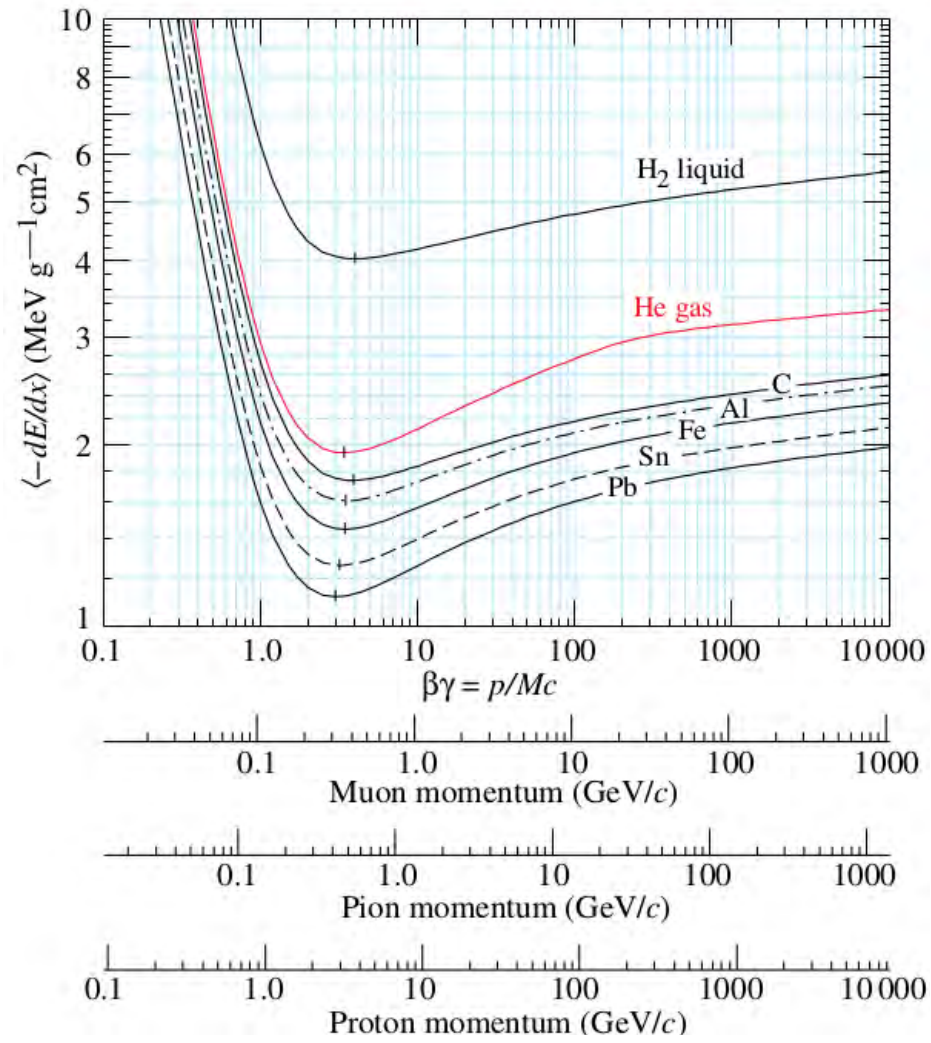

Figure 3.2: Mean energy loss in different materials [8]

The curve progression is exemplified in Figure 3.2. Characteristic for the curve is its minimum at $\frac{p_0}{m_0 c} \approx 3\beta\gamma$, where every particle loses least energy. A particle with this momentum is called Minium Ionizing Particle (MIP) [8]. Electrons and their corresponding anti-particles, the positrons, are light weight particles and therefore the Bethe formula is unsuitable. In this case the mean energy loss $\langle \frac{\mathrm{d}E}{\mathrm{d}x} \rangle$ is given by the Berger-Seltzer equation [13].

$$-\langle \frac{\mathrm{d}E}{\mathrm{d}x} \rangle = \rho \cdot \frac{0.153536Z}{\beta^2 A} \cdot (B_0(t) - 2ln(\frac{I}{m_e c^2}) - \delta) \tag{3.4}$$

- $c \rightarrow$ speed of light
- $\beta = \frac{v}{c} \rightarrow$ velocity relative to speed of light
- $m_e \rightarrow$ mass of the electron

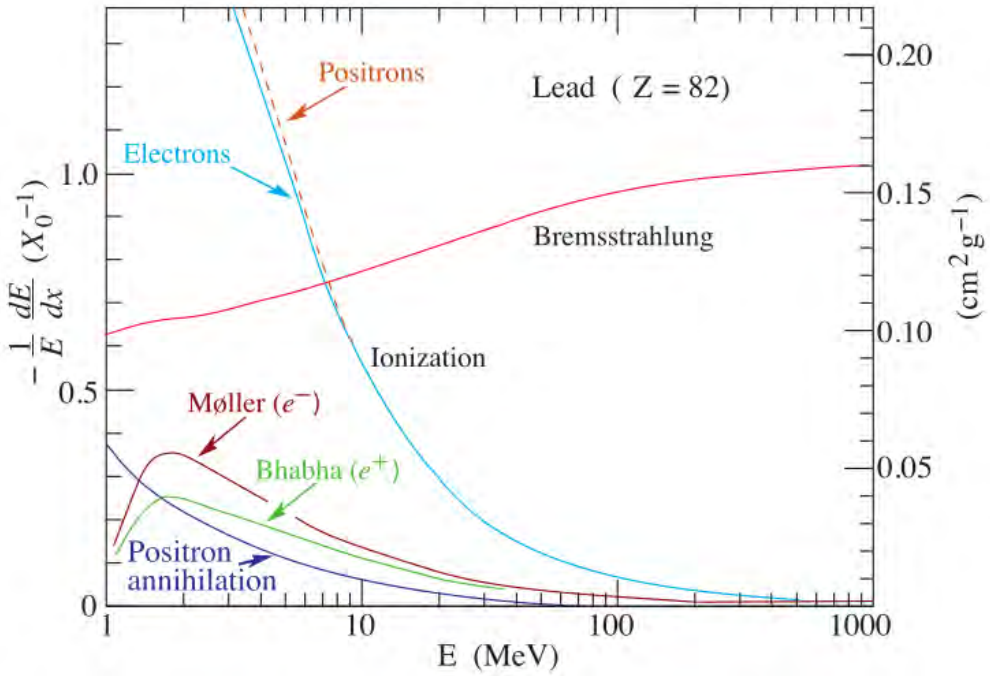

Figure 3.3: Different contributions of energy loss for electrons in lead [8]

- $Z \rightarrow$ number of protons in the nucleus
- $A \rightarrow$ number or nucleons
- $\rho \rightarrow$ density of the material
- $I \rightarrow$ mean excitation energy of the material
- $\delta \rightarrow$ density correction

For higher energies E, Bremsstrahlung, which is described in equation 3.5 [14] gives significant contributions to the energy loss.

$$\frac{\mathrm{d}E}{\mathrm{d}x} = -\frac{E}{X_0} \tag{3.5}$$

The radiation length X_0 is material dependent and can be approximated with [14]:

$$X_0 = \frac{716.4\,\mathrm{g/cm^2} \cdot A}{Z(Z+1) \cdot ln(\frac{287}{\sqrt{Z}})} \tag{3.6}$$

As shown in Figure 3.3, the effect of Bremsstrahlung dominates at a critical energy.

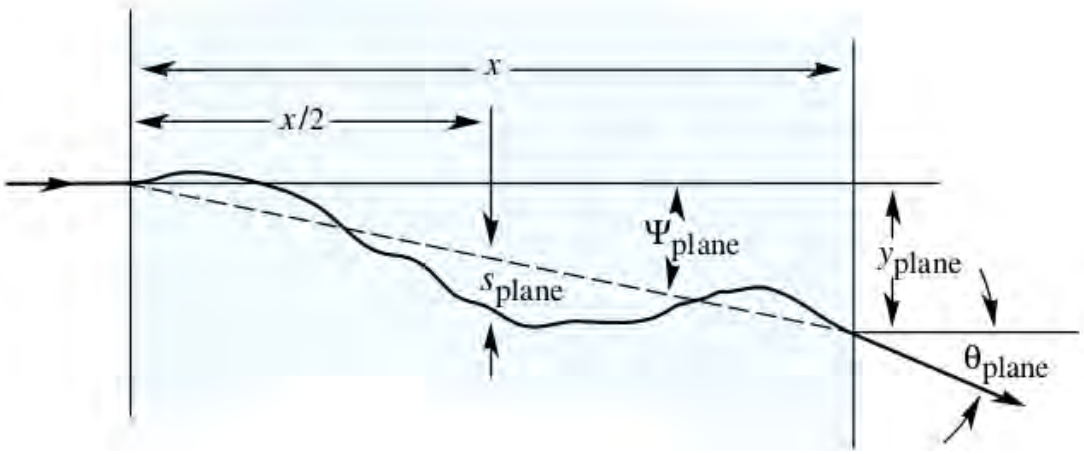

Figure 3.4: Graphical visualisation of multiple Coulomb scattering by [8]

3.3 Multiple Coulomb Scattering

If a charged particle with charge z passes through matter it scatters at the Coulomb fields of nuclei which leads to small angle deflections, as its illustrated in Figure 3.4. This evokes a change of primary direction of the particle, when leaving the medium. After the central limit theorem angles are Gauss distributed, yielding the following equation for the exiting angle θ_{rms} [8]:

$$\theta_{rms} = \frac{13.6\text{MeV}}{\beta cp} z \sqrt{\frac{x}{X_0}} [1 + 0.038 \ln(\frac{x}{x_0})] \tag{3.7}$$

As seen in equation 3.7 the influence of multiple Coulomb scattering strongly depends on the thickness of the medium for the same material and low momenta p. This explains why its important to keep the thickness x compared to the radiation length X_0 of the Mu3e detector as low as possible to decrease the dominant influence of multiple Coulomb scattering and prevent significant changes in particle tracks.

4 Introduction to X-Rays

X-Rays are photons with energies in a range of roughly 10 eV to several 100 keV. Depending on the energy, X-rays can be classified as soft (below 10 keV [15]) and hard X-rays. In this thesis an energy range of 4.5 keV to 35 keV is covered.
Albeit multiple ways of creating X-rays exist, only the X-ray tube is introduced below. An ordinary X-ray tube consists of a cathode and anode, mostly tungsten or copper, in vacuum. Applying a current to the cathode induces heat, allowing electrons to dissolve. In this connection the number of free electrons is proportional to the current. Through an electric field, produced by applied high voltage, the electrons accelerate towards the anode.
Two different types of X-ray radiation occur:

Bremsstrahlung

Electrons hitting the atoms of the anode are slowed down by the Coulomb field of the nuclei yielding to energy loss in terms of emitted photons. The resulting spectrum is continuous up to a endpoint energy E_{max}. At E_{max}, the full kinetic energy of a photon with wavelength λ_{min} is transferred:

$$E_{max} = E_{kin} = eU \implies \lambda_{min} = \frac{hc}{eU} \tag{4.1}$$

The spectral distribution I_0 can be appromixated with Kramers' law [16]:

$$I_0(\lambda)\ \mathrm{d}\lambda = K(\frac{\lambda}{\lambda_{min}} - 1)\lambda^2\ d\lambda \tag{4.2}$$

- $K \rightarrow$ Kramer constant, proportional to atomic number Z and tube current I
- $\lambda \rightarrow$ wave length of the X-ray photon

X-Ray Fluorescence

Accelerated electrons from the cathode can kick electrons out of inner shells of the anode material. Electrons from higher shells are used to fill this gap. During this process the electrons are falling from higher to lower energy levels, resulting in emission of X-ray photons with a characteristic wave length. The occurrence and therefore the intensity of the lines depend on the initial and final shell level, which is the likeliest for the transition of L- to K-shell equivalent to the K_α-line.

The final spectrum of the X-ray source is the superposition of the continuous and characteristic spectrum and is drawn in Figure 4.1.

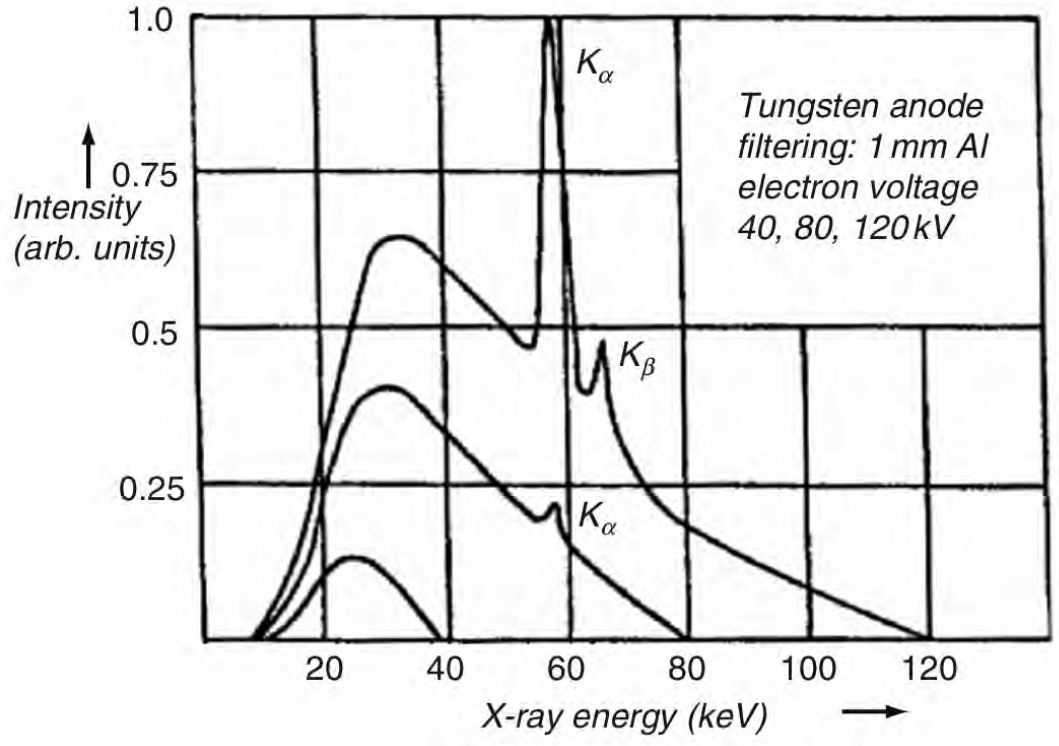

Figure 4.1: Spectrum of X-ray tube with tungsten anode [15]

5 Semiconductor based Pixel-Detectors

The pixel layers of the Mu3e detector are a crucial part of the experiment. The single components of the pixel layers are the MuPix chips, which are silicon based pixel detectors. In the following the basics of semiconductor physic and the HV-MAPS principle, used in the MuPix, will be explained.

5.1 Semiconductor Physics

Semiconductors are fundamental components in electronics and almost every electronic device is based on them. Also in detector physics semiconductors revolutionized the concept of detecting particles and radiation in a compact manner.

5.1.1 Semiconductors

In solid states, atoms in the crystal lattice are generating a periodic potential. Electrons moving inside this potential can be described through waves which undergo Bragg reflection at the Brillouin zone. This results in separated energy levels which are named bands. Between two bands a zone with no solution, referred as band gap, exist. At a temperature of 0 K all energy states below the Fermi energy E_F are fully occupied and states above are empty. The energy band below E_F is fully equipped and referred as valence band. Empty or partially occupied bands are called conduction bands. In the case of overlapping bands or if E_F is inside a band, as illustrated in Figure 5.1, those bands can only be partially filled and are therefore conductors. If the Fermi energy is in between a band gap, electrons can't fill the conduction band above because of missing energy, which results in an insulator. However, if the band gap is small enough, electrons can reach the conduction band through thermal excitation, defining a semi-conductor. Semiconductors can be categorized into two types:

Intrinsic Semiconductors If an electron is excited into the conduction band, it is leaving an empty space in the valence band, referred as hole. This hole can be seen as positive electron charge. Filling of a hole with electrons from other bands, is called recombination. Electrons from the band recombining with a hole, leaving a hole themselves, which makes them quasi free charge carriers. The conductivity in intrinsic semiconductors depends only on temperature and size of the band gap.

Extrinsic Semiconductors Through the insertion of atoms with more or less valence electrons, a higher number of holes or electrons can be used for recombination.

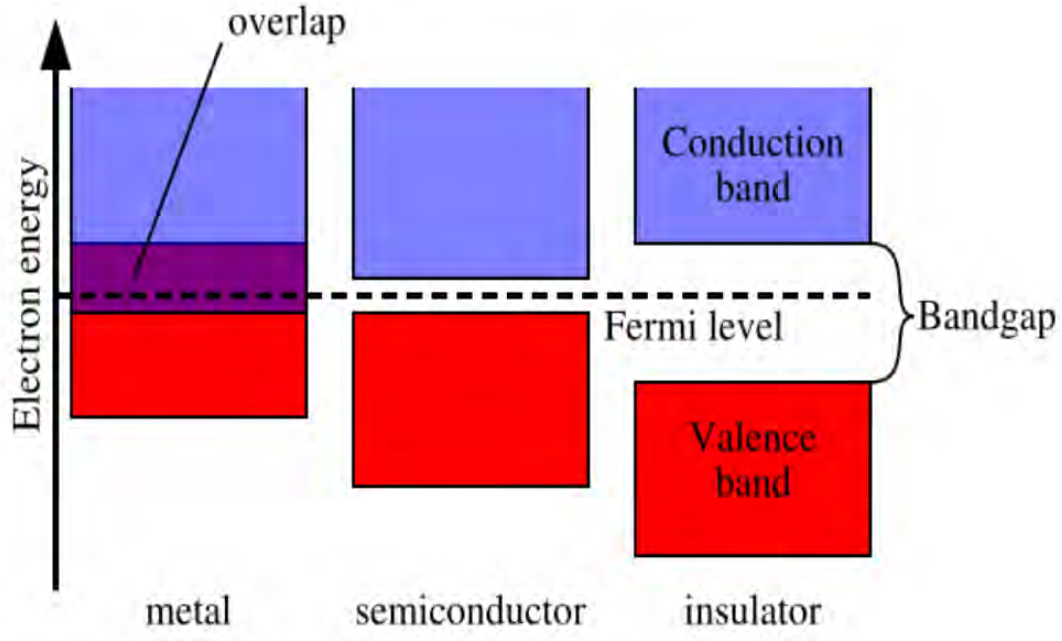

Figure 5.1: Band model for different conductor types [17]

With this the charge carrier density increases and additional energy levels were introduced, leading to a shift of the fermi energy towards the conduction or valence band depending on the majority carriers. Adding more holes through elements with one less valence electron gives a p-doped semiconductor (Figure 5.3), whereas elements with one more results in n-doping (Figure 5.2).

More about theory of conductivity and semiconductors can be found in [20] and [21].

5.1.2 pn-junction

A pn-junction is created through contact of p- and n-doped semiconductors. From both sides free charge carriers diffuse and recombine. The left over ions create an electric field, which induces a drift in the opposite direction of the diffusion. The system regulates itself until drift and diffusion are in equilibrium. This results in a charge free zone, the depletion zone, which makes up a diode. If an external voltage is applied, the depletion zone gets either bigger or smaller depending on the voltage sign as shown in Figure 5.4. If the diode is driven with a reverse biased voltage U_0, the zone width w increases and can be described with [22]:

$$w = \sqrt{\frac{2\epsilon_0\epsilon(U_{drift} - U_0)}{e} \cdot \frac{N_A + N_D}{n_i^2}} \qquad (U_0 < U_{drift}) \tag{5.1}$$

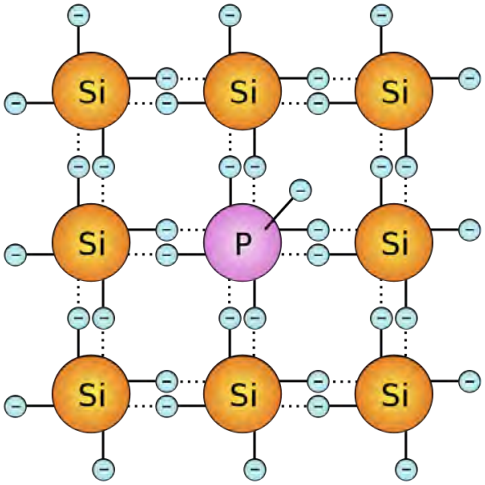

Figure 5.2: N doping of silicium [18]

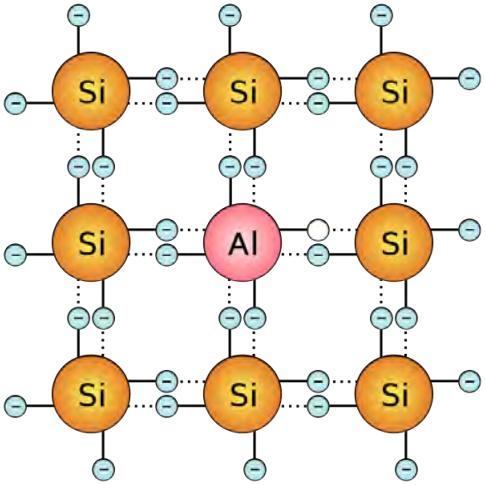

Figure 5.3: P doping of silicium [19]

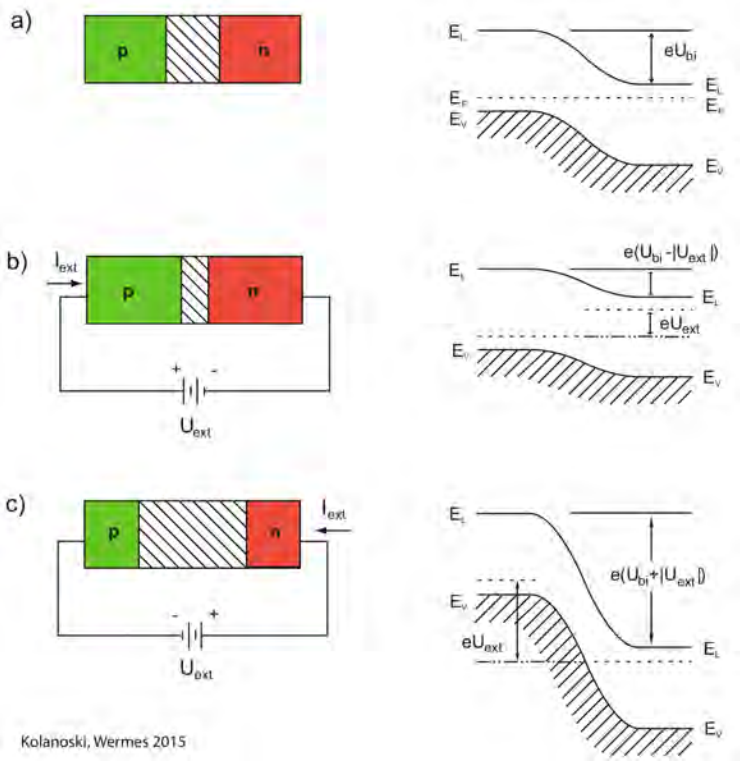

Figure 5.4: pn-junction and energy bands with different external voltages from [10]: a) no voltage b) forward bias c) reverse bias

- $\epsilon_0 \rightarrow$ electric field constant
- $\epsilon \rightarrow$ electric permittivity
- $U_{drift} \rightarrow$ diffusion voltage from the pn-junction
- $N_i \rightarrow$ doping concentration of acceptors and donators
- $n_i \rightarrow$ intrinsic charge carrier concentration

This would lead to a depletion zone width of $w \approx 8\,\mu\text{m}$ [22] when using a voltage of $-60\,\text{V}$, as calculated for the assumed doping concentration of the used HV-CMOS process.

5.1.3 Signal Detection

Particles passaging through matter are depositing energy in solid state detectors, as described in chapter 3. With energy deposit electron-hole pairs are created in the semiconductor. Inside the depletion zone, charges are collected via drift. The drift velocity v_{Di} for electrons and holes is determined through their mobility μ_i and the external electric field E [10]:

$$v_{Di} = \pm\mu_i \cdot E \tag{5.2}$$

Additional electron-hole pairs created outside of the depletion zone are likely to recombine before being collected. Still a few can diffuse into the depletion zone, where they are collected via drift. The charge collected via diffusion has a small portion compared to the drift charge. If the applied voltage reaches a specified level, the secondary electrons have enough energy to create new electron-hole pairs, leading to an avalanche effect.

5.2 HV-MAPS Pixel Sensor

Today, pixel detectors based on semiconductors are widely used in particle physics detectors due to their fast readout and great spatial resolution. Most times the detector is based on the hybrid pixel principle, where the sensor consists of an semiconductor detector itself and an additional readout electronics chip. Both layers are connected via bump bonding, which increases the radiation length of the sensor. For Mu3e, where thickness of the sensors is crucial due to multiple Coulomb scattering, this principle is not efficient. Therefore, the HV-MAPS technique [23] is used. Monolithic sensor means that both, readout and sensor, are merged into one unit, which reduces the thickness of the total detector a lot. To achieve this, a commercial CMOS process [24] is used, where the active region is not on top but inside the substrate as depletion zone. Hence, a single pixel consist of a deep n-well inside a doped p-substrate forming a p-n diode, as exemplified in Figure 5.5. By

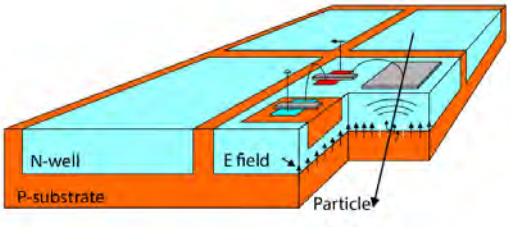

Figure 5.5: Drawing of the HV-MAPS design [23]

applying a high voltage the depletion zone increases, where charge can be collected via drift. This allows a fast readout compared to normal MAPS sensors, where charge is collected via diffusion.

Part II

Experimental Setup

6 MuPix Sensor

The MuPix-Chip is a family of pixel sensor prototypes for Mu3e based on the HV-MAPS principle. In this chapter version 7 of the MuPix sensor, which is used in this thesis, will be introduced.
The MuPix7 is the first sensor prototype which fulfils all necessary functionalities needed by the Mu3e-Experiment Phase I. Main parts of the sensor consist of a pixel matrix with 32×40 pixels with a following periphery containing the readout electronics at the bottom (Figure 6.1). The total chip has an overall size of 3.8×4.1 mm^2, whereas the size of a single pixel is 103×80 µm^2 resulting in an active region of 3.2×3.2 mm^2. Through usage of the HV-MAPS technology the chip can be thinned down to about 50 µm, relating to a relative radiation length of $\frac{x}{X_0} = 0.054\%$. The functionality is based on a standard CMOS-process where a deep N-well, located in a P-substrate, forms a depletion zone when high voltage is applied. Thus, charge is collected via drift, whereas in comparison a MAPS sensor uses diffusion to collect charge. This results in a very fast charge collection and thus a quick readout. With the electronics a good timing resolution of < 14 ns can be achieved.

6.1 Pixel Electronics

An overview of the read-out electronics is given in Figure 6.3.
The first part of the readout is the analogue part. It begins with the charge signal of the nine parallel coupled pixel diodes (Figure 6.2) which is amplified by a Charge Sensitive Amplifier (CSA). Instead of using the signal of the pixel diode, a test pulse can be injected as well. After the amplification the signal is send from the pixel to the chip periphery through a Source Follower (SF). In the periphery a second amplifier

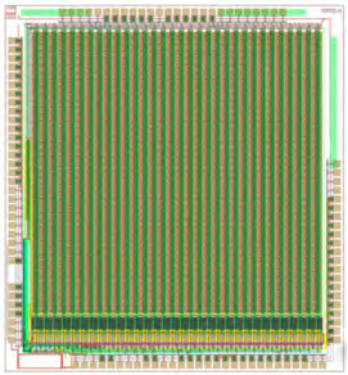

Figure 6.1: MuPix 7 Sensor Layout

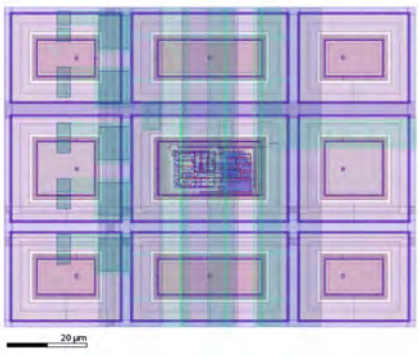

Figure 6.2: Layout of MuPix 7 pixel

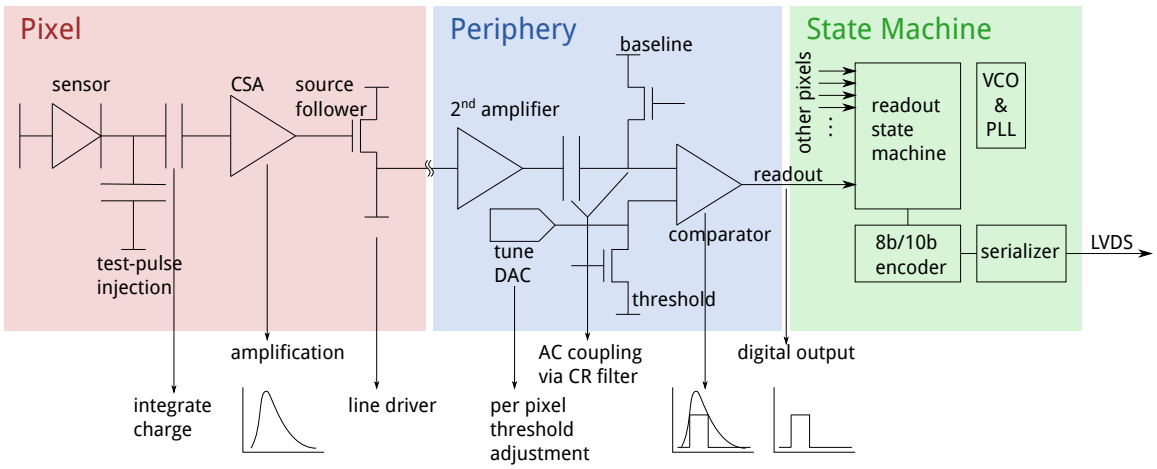

Figure 6.3: Read-Out Electronic of MuPix7

and a comparator follows for each pixel, where the analogue signal is converted into a digital one. At this juncture the signal is added to a bias voltage, the baseline, which is roughly at 0.8V. If the modified baseline is smaller than a second bias voltage, the threshold, the comparator generates an output. The duration of the output is as long as the signal is below the value of the threshold. This time is referenced as Time-over-Threshold (ToT). Here each pixel has the ability to individually adjust the threshold via a 4-bit Tune DAC (TDAC). Tuning of pixels allows a compensation of pixels inhomogenities through fabrication fluctuations towards each other, leading to a downscale of noise and a more steady signal response.
A complete overview of all bias voltages and their functionality can be found in section 13.2.

6.2 Digital Part

The comparator output of one pixel can be directly accessed via the so called hitbus or is forwarded to an edge detector which triggers on the rising edge of the outgoing signal. With the hitbus only one selectable pixel can be read out at the same time. At detection of the rising edge a timestamp of the hit is generated and sampled with a frequency of 62.5 MHz. This frequency is a fraction of the constant frequency 625 MHz established by the control circuit of the Voltage Controlled Oscillator (VCO) and the Phase Locked Loop (PLL). Furthermore this constant frequency is used by the serializer which sends the 8b/10b encoded data to an Field Programmable Gate Array (FPGA) over a serial link with a rate of 1.25 GBit/s.

6.3 Pulse-Shaping

Electronic circuits or components are limited by an characteristic frequency range, which causes a modulation /modification of processed signals. The development

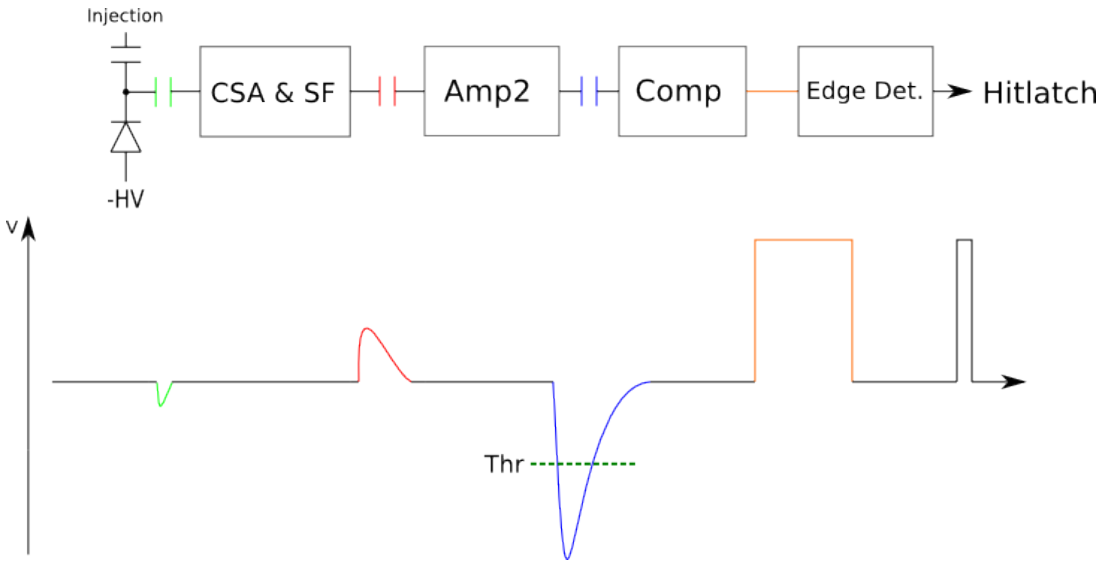

Figure 6.4: Pulse-Shaping of MuPix7

process of the form of an incoming signal passing through an electronic circuit is called pulse shaping.
The signal of the MuPix7 is undergoing several components (see Figure 6.3), before the analogue pulse is converted into a digital one through the comparator, as shown in Figure 6.4. These components working together as a high pass filter with a following low pass filter (short CR-RC-filter or shaper) [25], consisting each of a resistor R and capacitor C. The discharge of the high pass filter is described through the differential equation:

$$\frac{\mathrm{d}U_{CR}(t)}{\mathrm{d}t} = -\frac{1}{R_{diff} \cdot C_{diff}} \cdot U_{CR}(t) \tag{6.1}$$

Its solution is (with $\tau_{diff} = R_{diff} \cdot C_{diff}$):

$$U_{CR}(t) = U_0 \cdot \exp^{-\frac{t}{\tau_{diff}}} \tag{6.2}$$

Similarly the charge of the low pass filter is described with:

$$\frac{\mathrm{d}U_{RC}(t)}{\mathrm{d}t} = \frac{1}{R_{int} \cdot C_{int}} \cdot (U_0 - U_{RC}(t)) \tag{6.3}$$

and has the solution (with $\tau_{int} = R_{int} \cdot C_{int}$):

$$U_{RC}(t) = U_0 \cdot (1 - \exp^{-\frac{t}{\tau_{int}}}) \tag{6.4}$$

Using system theory, the resulting pulse shape can be achieved through the convolution integral of the input signal coming from the CSA and the CR/RC-filters:

$$U_{pulse}(t) = U_{electrode}(t) \star U_{CR}(t) \star U_{RC}(t) \tag{6.5}$$

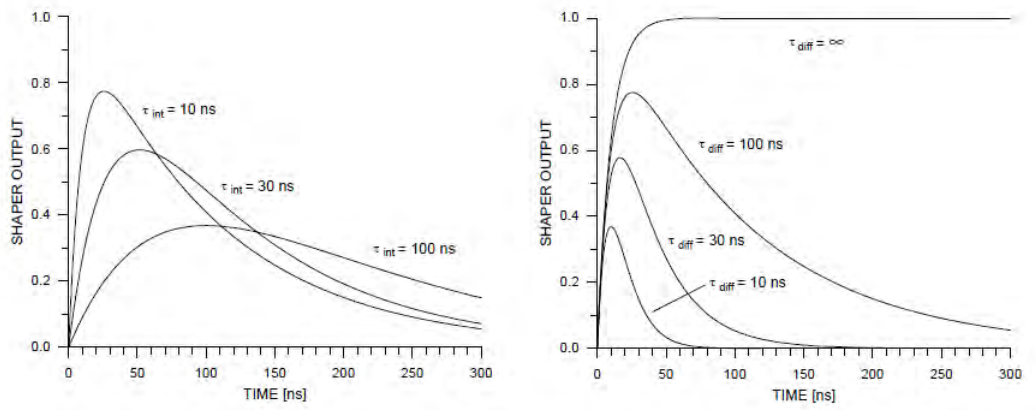

Figure 6.5: Pulse shapes for different time constants ($\tau_{diff} = 100\,\text{ns}$, left) and ($\tau_{int} = 10\,\text{ns}$, right) after [25]

Approximating the input signal $U_{electrode}$ as a rectangular function:

$$U_{electrode}(t) = 1 \forall t \in (0, a) \tag{6.6}$$

equation (6.5) gives two possible solutions:

$$U_{pulse}(t) = \begin{cases} U_0 \cdot \frac{\tau_{int}}{\tau_{int} - \tau_{diff}} \cdot (\exp^{-\frac{t}{\tau_{int}}} - \exp^{-\frac{t}{\tau_{diff}}}) & \tau_{int} > \tau_{diff} \\ U_0 \cdot \frac{t}{\tau} \cdot \exp^{-\frac{t}{\tau}} & \tau_{int} = \tau_{diff} = \tau \end{cases} \tag{6.7}$$

A visualisation of pulse shapes for different time constants τ_{int} and τ_{diff} is shown in Figure 6.5. It shows that for higher integration-times τ_{int} the signal height decreases but the pulse length is increasing. Also for a higher differentiation-time τ_{diff} the output has a longer duration but instead of shrinking, the signal height is increasing with τ_{diff}. However, a maximum output can't be exceeded. A detailed description of pulse shaping can be found in [25] and [10], whereas further information on pulse-shaping for other MuPix versions can be found in [22], [2] and [26].

7 Lab Setup

In this chapter the setup utilised for this thesis is explained. It includes the 'Single Setup' consisting of the necessary hardware and software needed to run and measure with the MuPix7 and miscellaneous attachments. Additionally the X-ray source used with the single setup is presented further.

7.1 Single Setup

Single setup is the term for collaboration of all hardware and software parts needed to operate a single MuPix sensor. Main component of the single setup is the Printed Circuit Board (PCB) designed by Dirk Wiedner. It contains all necessary in- and output interfaces for control and power of the MuPix sensor, whereas the chip itself is glued and bonded in the center of the board. Depending on usage of the setup, the PCB is fixed most times by custom holders crafted by the institute workshop. Two external power supplies are providing the necessary voltages and currents for the chip. The high voltage needed for the diode bias of the chip is delivered by the Keithley (Figure 7.1, red, [27]), whereas the low voltage is made available by the HAMEG (Figure 7.1, blue, [28]). To retrieve and send data to the chip, the PCB is connected to a FPGA which is plugged into the computer via a PCI-E slot. For the connection itself two High Speed Mezzanine Card (HSMC) slots are available on the FPGA. The FPGA maps its data into the Random Access Memory (RAM) of the computer, where data can be easily accessed via software. Further, the PCB and the used software will be presented a bit more in detail.

7.1.1 PCB

Components and slots of the PCB are colored in Figure 7.2. A detailed description of each single part can be found in [26] and [2].

7.1.2 Software

Processing of data and control of the FPGA is done via software. The software is written in C++ with the usage of Boost [29],QT [30] and ROOT [31] libraries. A picture of the Graphical User Interface (GUI) is presented in Figure 7.3.

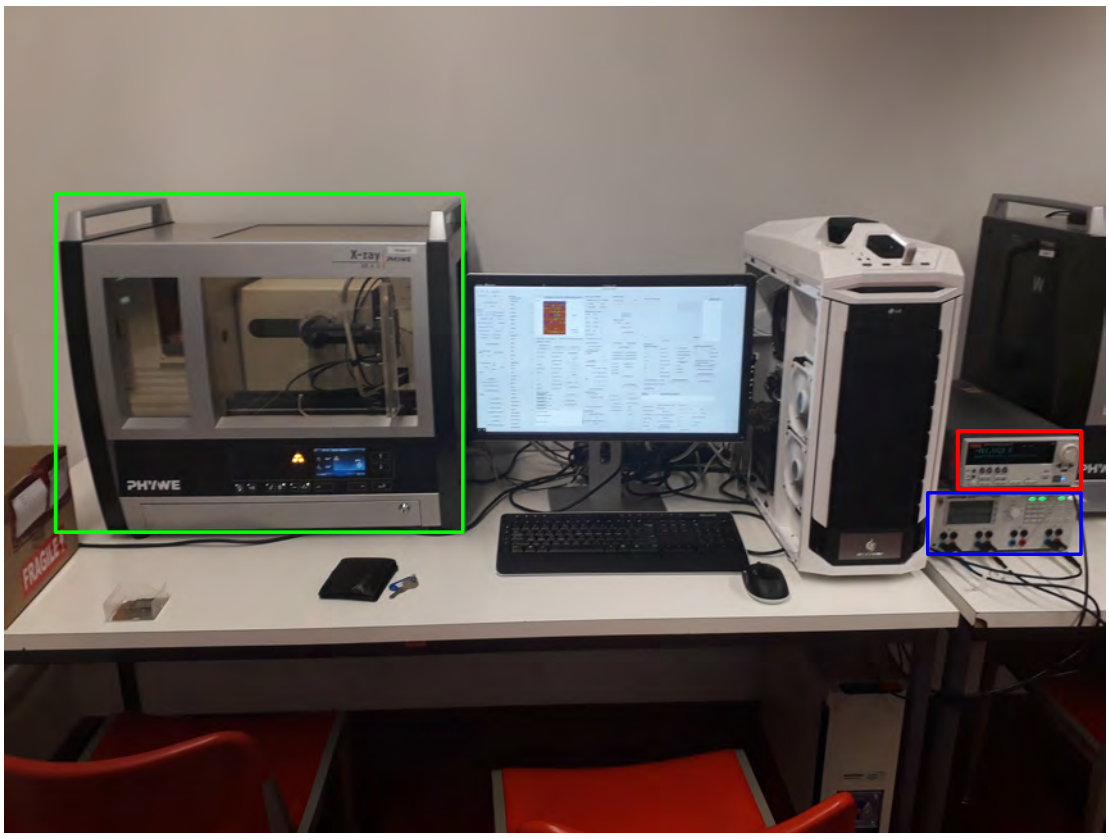

Figure 7.1: The single setup with the x-ray spectrometer (green), the sourcemeter (red) and the power supply (blue)

7.2 X-Ray Source

The X-ray source used within the single setup (Figure 7.1, green) is a PHYWE XR 4.0 expert unit Röntgengerät [32] with a tungsten anode. The X-ray unit has a tube voltage range of $U_{min} = 0.0\,\mathrm{kV}$ to $U_{max} = 35.0\,\mathrm{kV}$ which defines the energy of the X-ray photons and a current of $I_{min} = 0.01\,\mathrm{mA}$ to $I_{max} = 1.00\,\mathrm{mA}$ to control the intensity of the emitted spectrum. The equipment was originally designed for various X-ray diffraction experiments. Therefore, the apparatus contains a rotatable goniometer with a CCD-camera, which is not needed and therefore dismounted. The MuPix-PCB is mounted at the goniometer via a special manufactured fixture, which allows the rotation of the sensor, needed for the fluorescence measurements. Furthermore a special probe holder can be applied to the goniometer to carry the fluorescence probes. Both the fixture and the probe holder are presented in Figure 7.4 and Figure 7.5. An example of the X-ray tube spectrum is shown in Figure 7.6

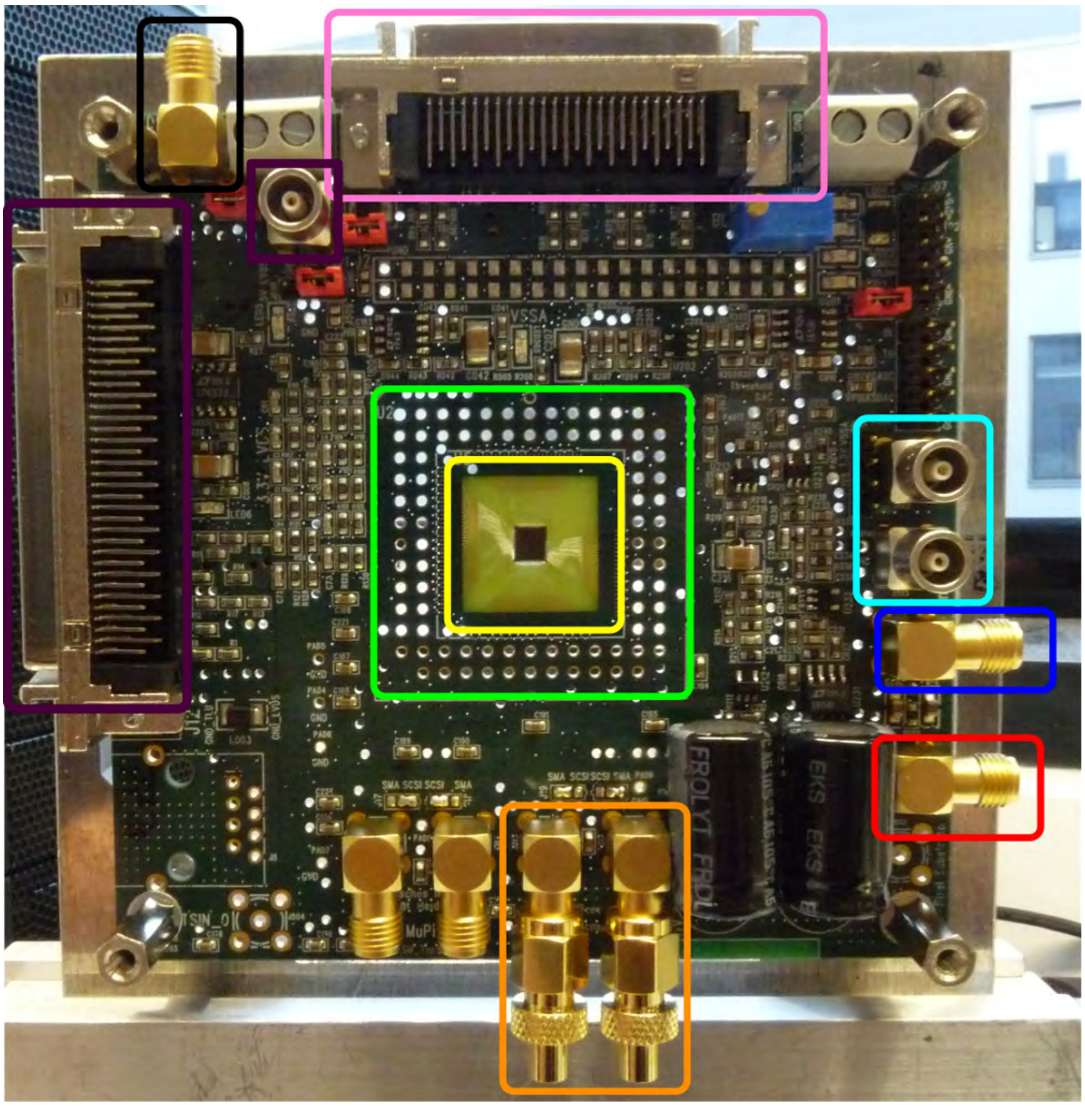

Figure 7.2: Picture of the PCB with colored components, taken from [26] and edited. (yellow) MuPix7, (light green) carrier socket, (black) single LVDS, (blue) low voltage, (red) high voltage, (purple) hitbus, (pink) readout/control, (orange) clock, (cyan) injection

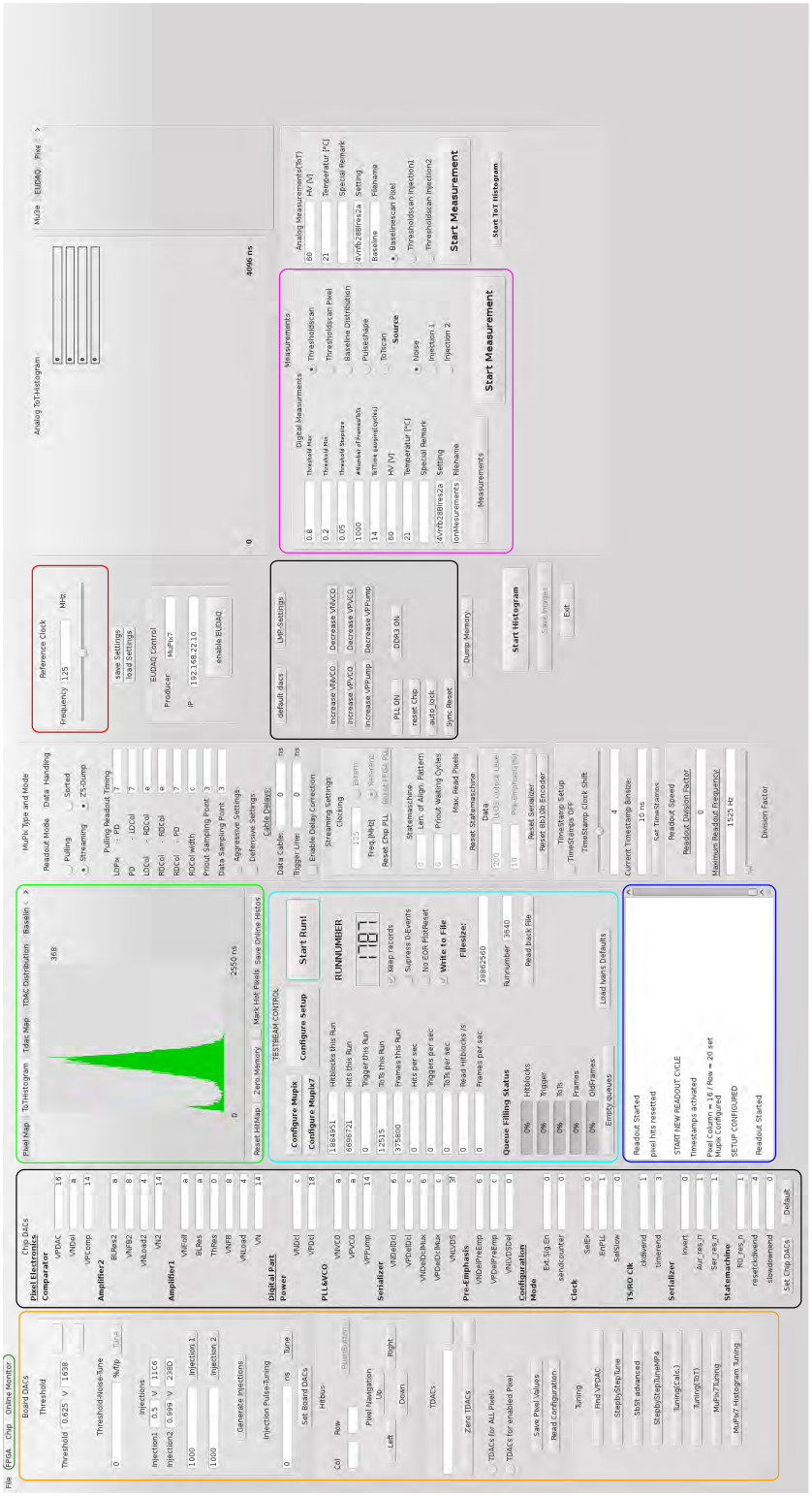

Figure 7.3: Screenshot of the GUI from the single setup software with different constituent parts colored from [26].
(orange) Board DACs, (black) Chip DACs, (light green) Monitoring, (cyan) Testbeam Control, (blue) Information Console, (red) Clock, (magenta) Measurements, (dark green) Additional Controls

Figure 7.4: Fixture for the PCB

Figure 7.5: X-ray fluorescence probe holder and example probes

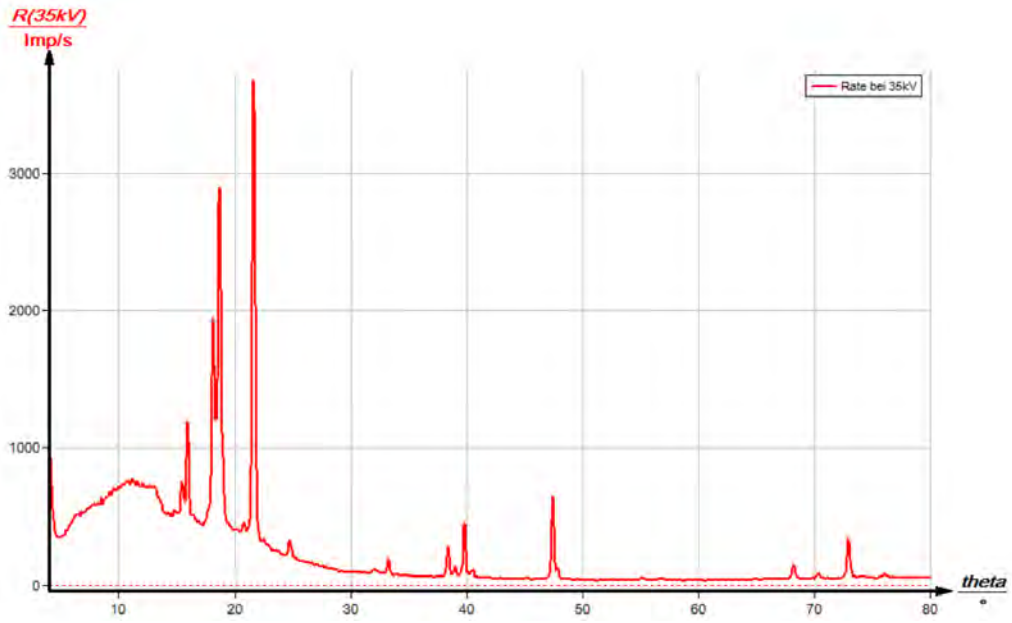

Figure 7.6: Measured X-ray spectrum by the vendor of the X-ray unit for a tube (tungsten) voltage of $U_{tube} = 35\,\mathrm{kV}$ with Bragg reflection [33]

Part III

Methods

8 Measuring Methods

In this chapter the measurement techniques and the used signal sources to achieve the energy calibration of the MuPix7 are presented.

8.1 Measured Quantities

8.1.1 Time-Over-Threshold

As shortly explained in section 6.1 the incoming pulse is added to a bias voltage, the Baseline, giving an negative pulse like presented in Figure 8.1. To produce digital output in the comparator, the pulse has to pass a threshold voltage. Duration length of the output is equivalent to the time of the incoming signal passing the threshold. This time is called Time-Over-Threshold (ToT) and can be readout directly through the hitbus. However only the ToTs for a single selectable pixel can be obtained at the same time.
Real detectors are never capable of registering the exact same signal. Therefore, the measured ToTs vary statistically. So to get a decent overview of their distribution, ToTs are filled into a histogram with a bin width of 10ns. Important characteristics of this distribution are its mean value and width. Those can be acquainted through fitting one ore more Gaussian profiles, depending on the spectrum of the source.

8.1.2 Digital Hit Information

Since start of the sensor readout, hit informations of each pixel are stored either in memory or in a binary file on hard disk. Each hit contains column, row and timestamp information. For a single sensor the distribution of timestamps is less relevant, hence only the number of pixelhits is used in the measurements. The presentation of the digital hit information can be done in hitmaps. Hitmaps are 2D contour plots, containing the number of hits for every pixel at a set threshold and a given measurement time. This gives information of how sensitive single pixels react on a continuous signal or shows the spatial intensity of a signal.

8.2 Measurement Process

8.2.1 Threshold Scan

A threshold scan describes the procedure of walking through different levels of thresholds to uncover the pulse shape of an incoming signal. For each adjusted

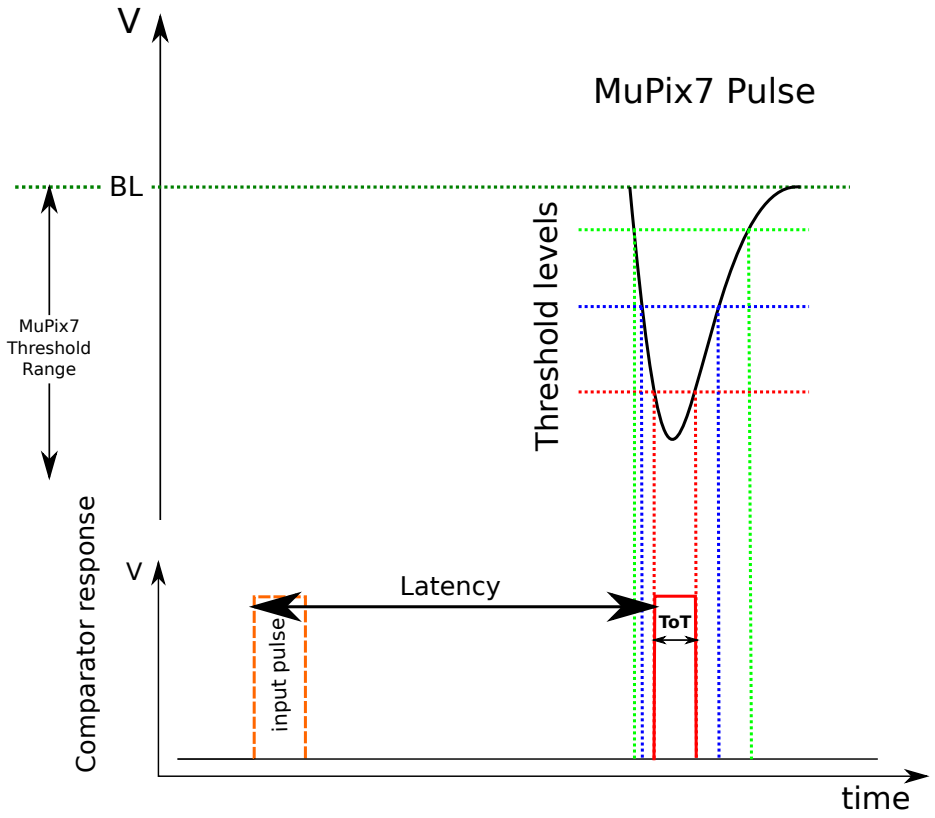

Figure 8.1: Schematic of the ToT

threshold the digital hit information for each pixel is collected. Hence the hits relay on statistical fluctuations and therefore the error is given by

$$\Delta\text{counts} = \sqrt{\text{counts}} \tag{8.1}$$

Presuming an ideal pixel, the resulting answer of the threshold scan should be an Heaviside step-function for a constant signal at the position of its signal-height U_s, which can be expressed through the baseline U_b and the threshold U_t:

$$U_s = |U_b - U_t| \tag{8.2}$$

However, signals of real pixels are always influenced by noise, which soften up the edges of the step-function creating an s-curve behaviour. It can be described by the integral of a gauss distribution with width σ as noise and the signal height at the mean value μ, given by the error function:

$$f(x) = \frac{1}{2}(1 + erf(\frac{x-\mu}{2\sqrt{\sigma}})) \tag{8.3}$$

A graphical representation can be found in figure Figure 8.2. Knowing the signal

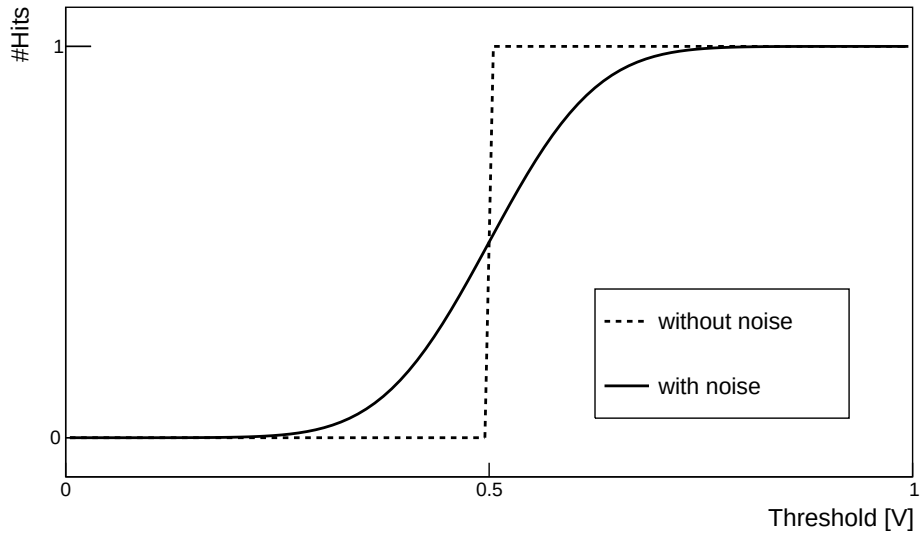

Figure 8.2: Smearing of the signal to an s-curve

height and the noise, the Signal to Noise Ratio (SNR) can be calculated:

$$\text{SNR} = \frac{\text{Signal}}{\text{Noise}} = \frac{|b - \mu|}{\sigma} \tag{8.4}$$

Because the digital hit information for the whole sensor is used in this measurement, one has to consider that hot pixels may block the whole readout column. Therefore the procedure limits the rate of each pixel to 700 Hz. If a pixel exceeds this limitation, a high TDAC is assigned to it and no further signals are detected at this pixel.
Sometimes curves of threshold scans show dips at random thresholds. These occur at the same position in every pixel and therefore the total chip. Reason for this are misconfigurations of the setup. Under the assumption of a monotonously increasing signal, the dips are later removed during evaluation and fitting of curves.

8.3 Signal Sources

In the following the used signal sources used for the measurements are presented.

8.3.1 X-Rays

As explained in chapter 4 the spectrum of X-rays from tubes can be divided into a continuous and a discrete part. To do a calibration of the sensor, well known energies have to be used. Here two different approaches are utilized. The first method applies the continuous Bremsstrahlung and thereby the endpoint energy. The X-ray spectrometer is capable for maximum energies up to 35 keV and due to small rate, a minimum endpoint energy of 7 keV can be achieved. Secondly, the

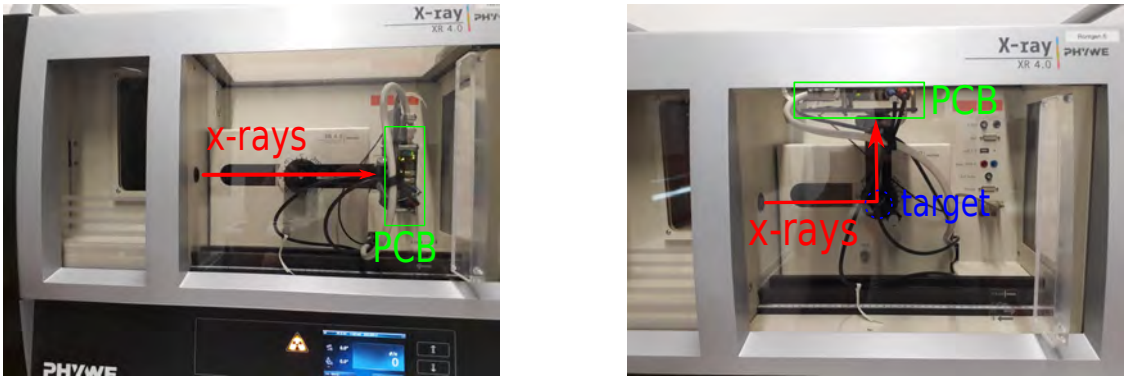

(a) Bremsstrahlung (b) X-Ray Fluorescence

Figure 8.3: Positioning of Mupix sensor in the X-ray setup for different measurement methods

characteristic lines of X-ray Fluorescence (XRF) are chosen as calibration energies, where a region of about 4−22 keV is available. An overview of the materials and their corresponding lines used during this thesis, can be found in the appendix. Regarding the lines, only $K_{\alpha 1}$-lines are usable because other lines are strongly suppressed by the low rate of the fluorescence photons.
To use the direct X-ray spectrum and therefore the endpoint energy, the MuPix has to be positioned as shown in Figure 8.3a. For the fluorescence measurements the target is rotated 45° against the incoming beam which grants the highest rate of fluorescence radiation onto the sensor (Figure 8.3b).

8.3.2 Iron-55 Source

The radioactive nucleus of iron-55 consists of 26 protons and 29 neutrons. Through electron capture (**EC**) a proton p transmutes into an neutron n through sending out an electron neutrino ν_e: $p + e^- \rightarrow n + \nu_e$.
This results in the reaction ${}^{55}_{26}\mathrm{Fe} \rightarrow {}^{55}_{25}\mathrm{Mn}* \rightarrow {}^{55}_{25}\mathrm{Mn} + \gamma$. The disexcitation of the electron is causing the emission of a X-ray photon with a characteristic energy depending on the shell level, or a Auger electron. The Auger electron can be neglected due to the fact that the probe prevents its escape. In addition to this, K_β lines (6.49 keV) will be ignored because of their strong suppression compared to the K_α line at 5.9 keV. Without any temporary decay states, Fe-55 reaches its final constitution ${}^{55}_{25}\mathrm{Mn}$ within a half-life time τ of about $\tau = 2.744$ y [34]. Figure 8.4 shows the decay scheme of iron-55.

8.3.3 Injection

Each MuPix 7 pixel has the ability to inject an signal into a group of pixels, via a capacitor, simulating charge deposit of a particle. It can be chosen whether a constant number of signals are injected or the injection is continuously. Both times

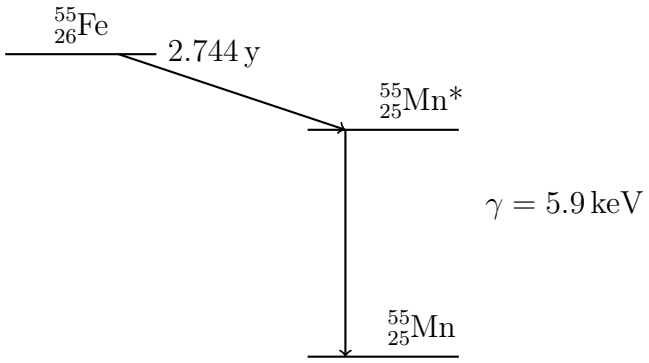

Figure 8.4: Decay scheme of the radioactive iron-55 source

the injection process can be controlled by a given rate which is capable for maximum rates up to 100 kHz. Additionally the option of injecting only in every second double row, instead of the total pixelmap, exist. This scheme is used to prevent the effect of crosstalk between neighboured pixels.

Part IV

Measurements & Results

9 Energy Calibration with X-Ray Endpoint-Energies

As presented in section 8.3, X-ray spectra from tubes have multiple known energies, which can be used for calibration purposes. The former approach to achieve an energy calibration is the usage of the endpoint energy from continuous spectra. Primal advantages of this method are its simplicity and potential of wide accessible energy ranges to get a basic impression of the calibration trend. The used MuPix7 settings for measurements in this chapter can be found in Table 13.4 in the appendix.

9.1 General Curve Inspection

The first step of a calibration procedure is to analyse the measured curve progression of the signal source. Therefore, a threshold scan using the direct X-ray spectrum was taken with standard settings (Table 13.4) and without tuning. Figure 9.1 shows the initial scan which was taken with an endpoint energy of 10 keV. The general curve can be divided into three regions. The first part of the curve is constant, because the pulse height induced by the energy deposition is too low to pass the threshold and therefore no comparator output is generated. At a certain threshold, the 10 keV-photons overcome the threshold for the first time and a rise in the curve can be seen. Due to noise and the continuity of spectrum, the transition appears continuous and not abrupt, as described in subsection 8.2.1.
Thenceforth, the progression matches the integral from right to left of the Bremsstrahlung spectrum (Figure 4.1). In higher threshold regions ($U_{thr} \leq 0.65\,\mathrm{V}$), cross talk affects the slope of the curve with a probability of 1-10% [35]. At the end of the curve a sudden rise at barely 0.7 V occurs due to noise at low thresholds. At this point even small signals generated by electronic noise create output in the comparator. Another important detail of the curve is its offset, which makes the endpoint approximation difficult. The Bremsstrahlung spectrum has a maximum energy and therefore a maximum pulse height is expected, which should lead to zero detected hits in low threshold regions, which is not the case. A look at the hitmap of the sensor at $U_{thr} = 0\,\mathrm{V}$ in Figure 9.4 reveals, that the offset is mainly induced by strong activity of few pixels. An explanation for this may be the sensitivity differences between pixels coming from the manufacturing process.
Nevertheless, the possibility of effects created by radiation influence on the readout electronics were investigated. For this, the outgoing X-rays were focused using a collimator (diameter $d = 0.1\,\mathrm{mm}$). Through rotation of the sensor in a small angles, the beam can be collimated onto the periphery and the active pixel matrix

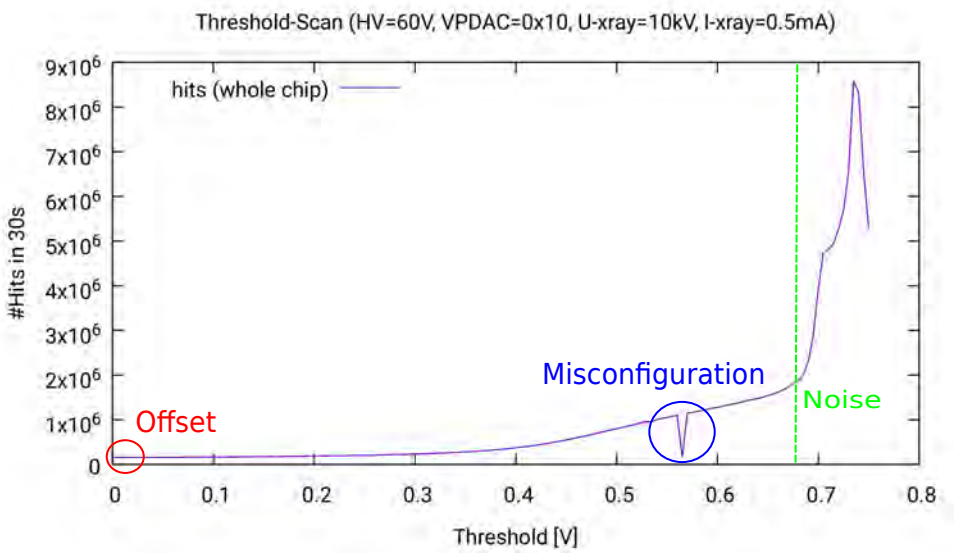

Figure 9.1: Threshold scan for 10 keV

separately. Figure 9.2 displays the measured hitmaps for both cases. Comparison of both hitmaps indicates that the high number of hits for individual pixels is not created by radiation of the digital chip part.

In order to exclude that the effect is created by the interference of two gammas, the rate is varied by changing the current of the X-ray tube. A linear behaviour is observed and fitted, thus indicating no event overlays

9.2 Influence of Tuning

As stated above, the offset of the curve received from the threshold scan is mostly generated by few very sensitive pixels. A solution for this problem would be tuning of such sensitive pixels. Therefore, the influence of varying TDACs for a single pixel is examined in the following. For this, pixel (7,30) is chosen due to its high activity at an threshold of 0 V, see Figure 9.4 for further studies. The influence of different TDACs onto the number of hits for this pixel is studied at $U_{thr} = 0\,\mathrm{V}$ with a measurement time of 60 s. The range covered by the TDACs can be controlled with a global DAC (VPDAC), which is also tested for different values. Figure 9.5 shows clearly that for higher TDACs the pixel registers less hits and at certain TDAC-VPDAC combinations hits vanish completely. Additionally, the number of hits decreases even more if the VPDAC is raised. This can be explained with the functionality of the VPDAC: The value of the VPDAC determines the absolute voltage which is added to the baseline by the bias voltage TDAC. Increasing the VPDAC increases therefore the new value of the baseline for this pixel, which leads to a higher distance of the baseline to the set threshold. Now a higher pulse height is needed to generate a signal in the comparator and therefore less or even no hits

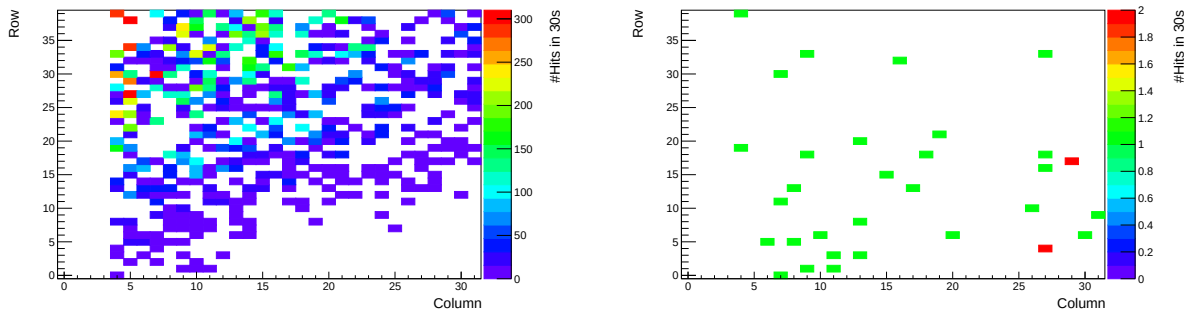

(a) Pixelmatrix (b) Periphery

Figure 9.2: Hitmaps for different parts of the chip being irradiated separately with collimated X-rays at a threshold of 0 V and a endpoint energy of $E = 10\,\mathrm{keV}$

were produced.
As a final result, tuning can be used to eliminate the offset at the beginning of the threshold scan. Because of this measurements, needed for the energy calibration, were done with a tuned MuPix7 sensor.

9.3 Baseline Shift Due To Noise Tuning

When the sensor is tuned, a voltage depending on the TDAC and VPDAC is added onto the global baseline of $b = 0.8\,\mathrm{V}$. Due to sensitivity differences, the baseline for each pixel is individually adjusted. This shift introduces a systematic error in the signal hight determination with equation (8.2), as the baseline varies now from pixel to pixel and is set to 0.8 V for the fit. The noise level for each pixel is not changed by the tuning. Therefore, equal noise thresholds can be compared and their difference corresponds to the shift of the baseline. To overcome this obstacle, the shift caused by the tuning has to be determined for each pixel separately. For this purpose, threshold scans were made for a tuned and untuned sensor without using any signal sources. The effect of tuning can be clearly seen in Figure 9.6: The distribution of noise is narrowed and the overall mean of the noise distribution is shifted roughly by 0.06 V. An exemplary noise threshold scan for a single pixel with and without tuning is shown in Figure 9.7a. The untuned sensors noise rises earlier compared to the tuned sensor. In the region between 2000 to 10000 hits the curves are parallel. Five different noise rates are used to calculate the shifts. This shift is later used to correct the signal heights. All results and distributions of the shift calculation are presented in Figure 9.7. The correlation of TDAC and calculated shift in Figure 9.7b shows a linear dependence as expected. To get an exact view on the dependency, a profile of the correlation is created and fitted with a linear function in Figure 9.8. Although shifts for TDACs bigger than 10 exhibit a non-linear behaviour, the shift calculation is applicable, because almost all TDACs

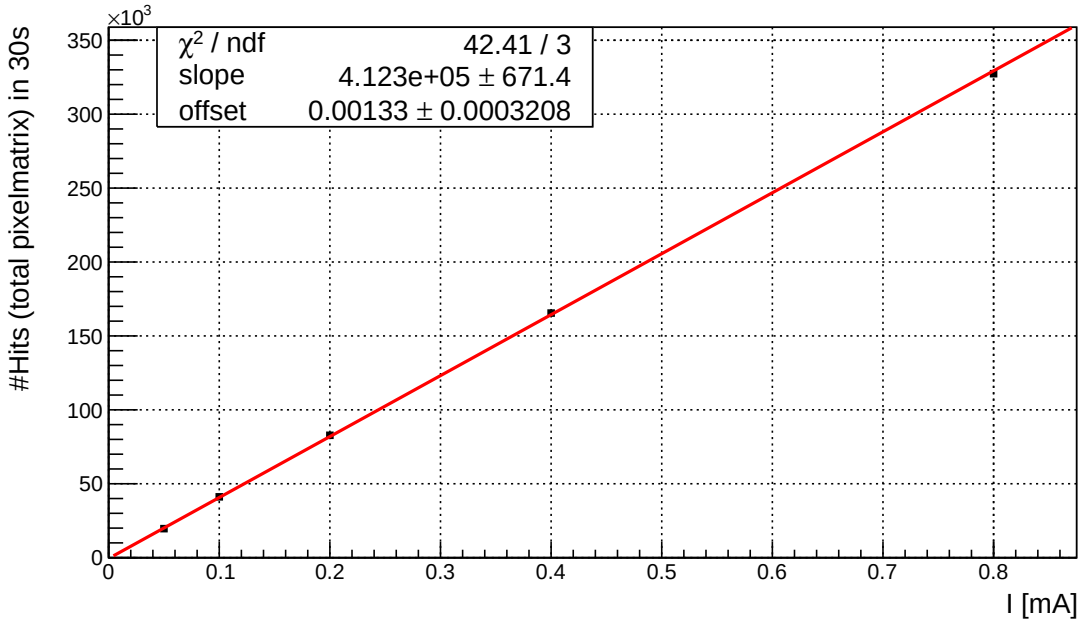

Figure 9.3: Number of detected hits as function of the tube current with a linear fit

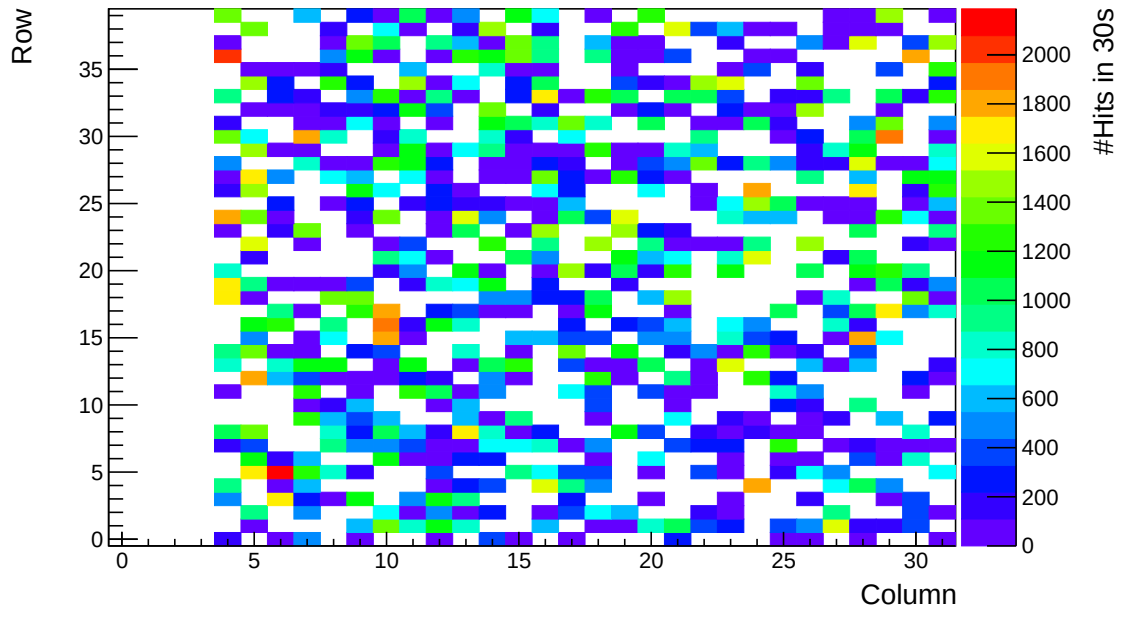

Figure 9.4: Hitmap at $U_{thr} = 0\,\mathrm{V}$ for $E = 10\,\mathrm{keV}$ without tuning of the sensor

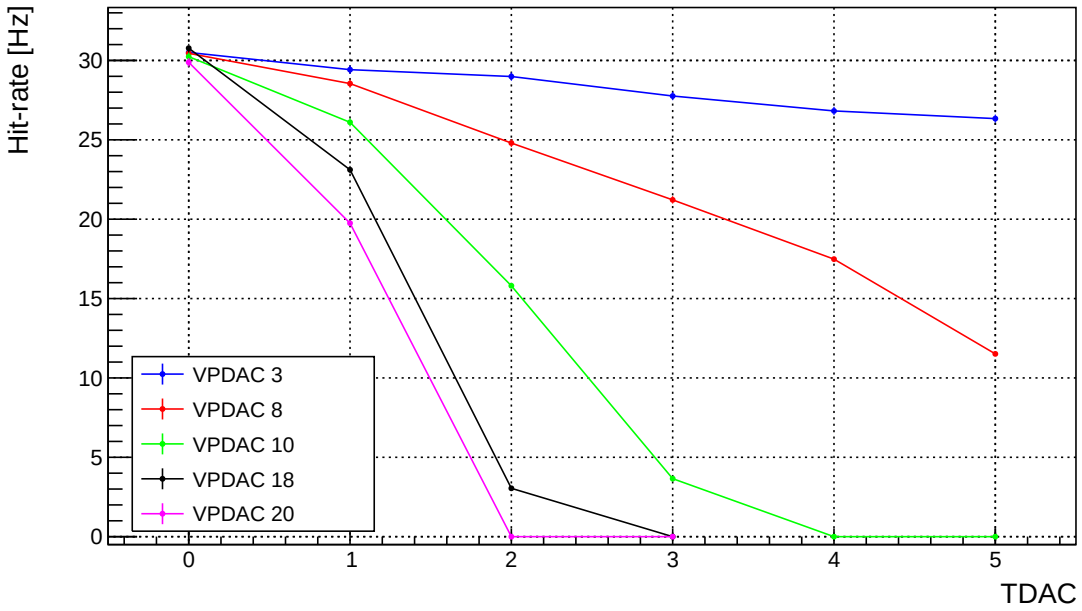

Figure 9.5: Hit rate of pixel (7,30) as function of the TDAC for different VPDACs at $U_{thr} = 0\,\mathrm{V}$

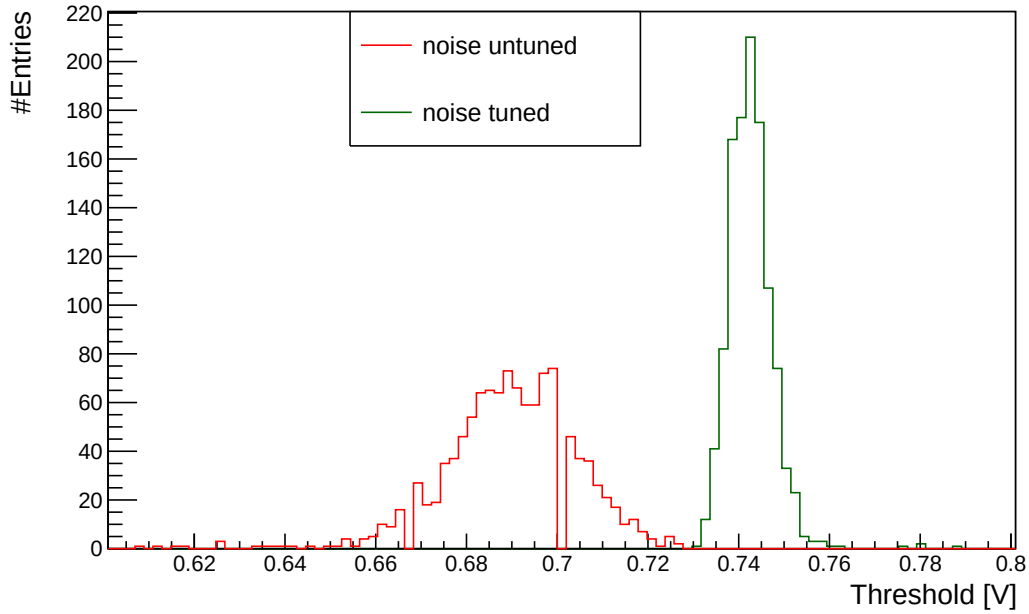

Figure 9.6: Threshold distributions for 1 Hz noise

are distributed around 6 (Figure 9.7d), where the determined shifts behave linearly. In addition to this, the curve has an offset very close to zero, which is presumed, because a TDAC of 0 is equal to a shift of 0 V. Comparing both, the shiftmap and the tunemap of the sensor (Figure 9.7c and Figure 9.7e), a pattern in row 0 burr out. A possible explanation for this is the close distance of row 0 to the digital part of the chip. There local powerlines and the first row of the periphery might influence the pixels in row 0.

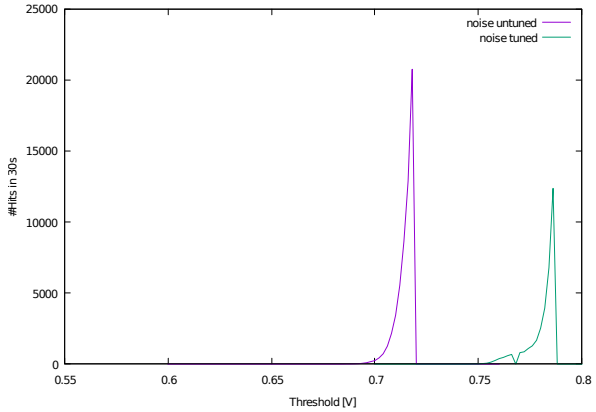

(a) Untuned and tuned noise thresholdscan

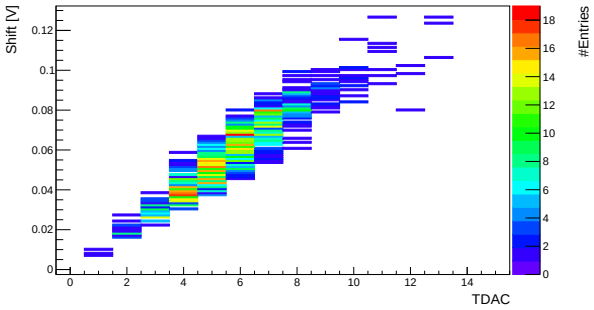

(b) Correlation between TDAC and shift

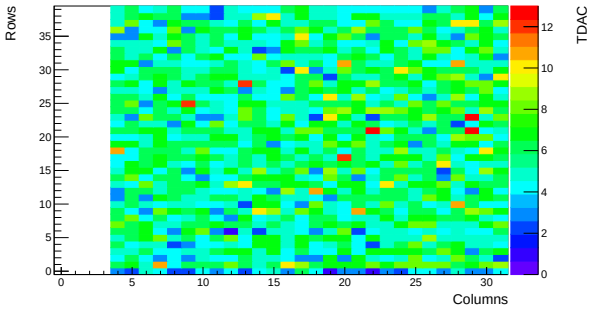

(c) TDAC-Map

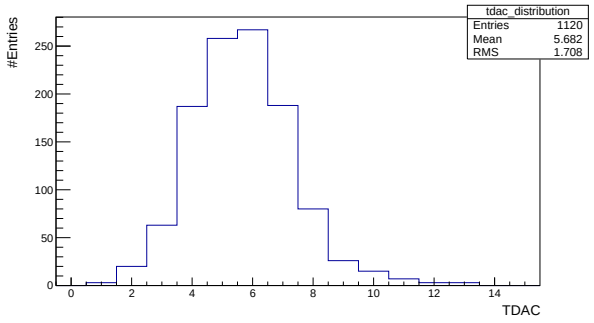

(d) Distribution of TDACs

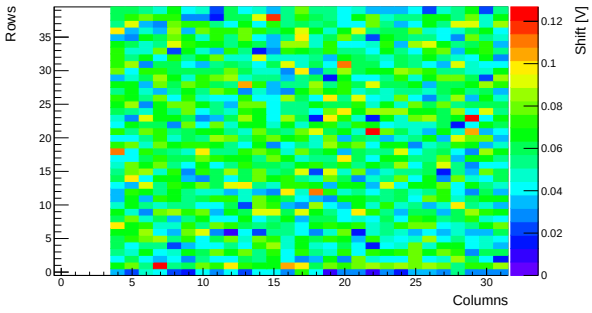

(e) Shift-Map

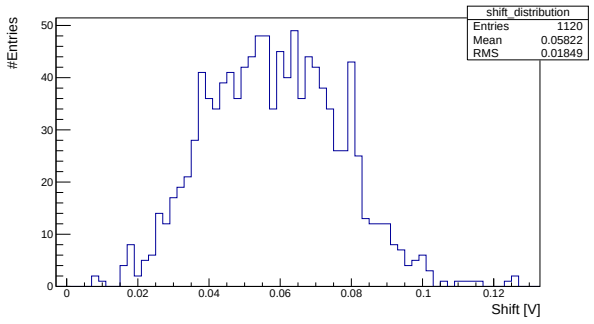

(f) Distribution of Shifts

Figure 9.7: Results from the shift calculation

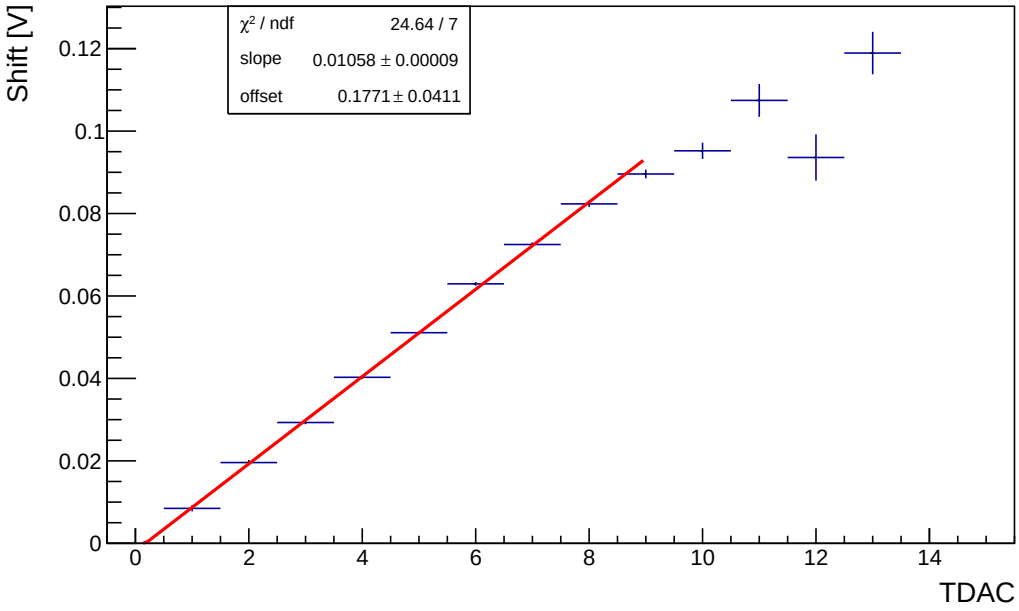

Figure 9.8: Profile of TDAC-Shift correlation with linear fit.

9.4 Calibration

To calibrate the sensor, threshold scans at various energies within a range of 7 keV to 35 keV were made. Energies below $E = 7\,\text{keV}$ were not accessible due to low photon rates. The minimal adjustable tube voltage difference is taken to estimate the energy error with equation (4.1) ($\implies \Delta E = 0.1\,\text{keV}$), because no further information on the PHYWE X-ray unit is available. For every measurement the position of the endpoint energy in each pixel is approximated via a linear fit with slope A and offset B in x-direction:

$$f(x) = A \cdot (x - B) \tag{9.1}$$

To get a good endpoint approximation, the linear fit boundaries are limited, to prevent influences from non-linear parts. An example fit is shown in Figure 9.9. The offset of the linear function directly matches the signal threshold. With Equation 8.2 the corresponding signal height is calculated and corrected with the determined shift from section 9.3. Figure 9.10 displays the calibration curve determined for a single pixel. The curve behaviour is expected to be linear due to the photo effect. Since a photon with higher energy E_γ creates more electron hole pairs n and thus a higher charge Q is collected, resulting in an higher output voltage U_0, which is given by the capacitor C equation:

$$Q = n \cdot e = C \cdot U_0 \implies U_0 = \frac{E_\gamma \cdot e}{W_{Si} C} \tag{9.2}$$

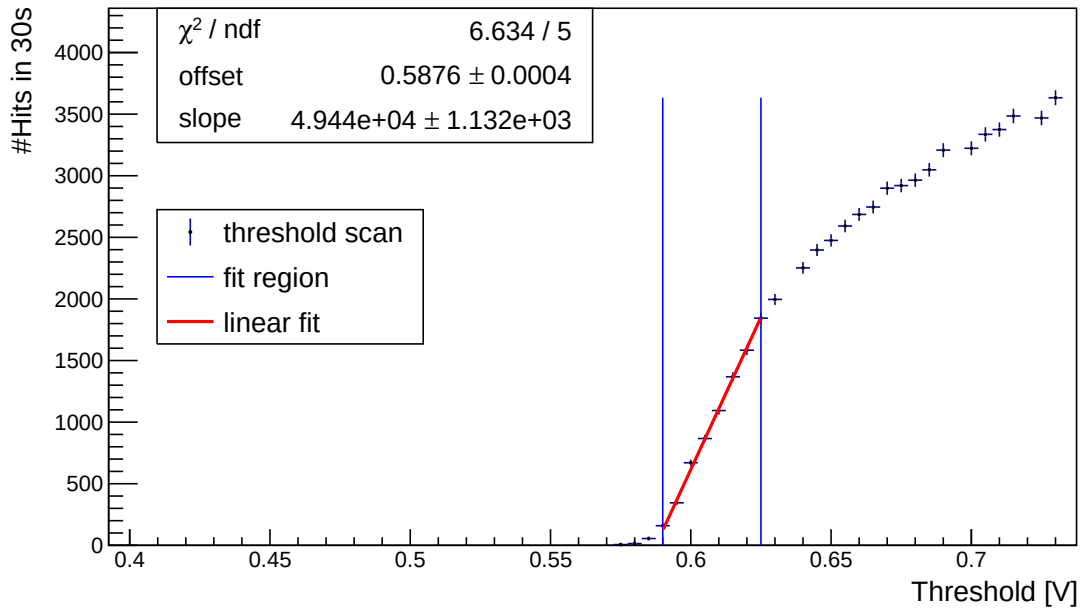

Figure 9.9: Approximation of the position of the endpoint energy in measured threshold scan at $E = 8.5\,\text{keV}$ for pixel 19-20

W_{Si} is the energy needed to create an electron hole pair in silicon.
After that the incoming pulse undergoes pulse-shaping as described in section 6.3. During this process the pulse height is modified linearly through an idealized shaping process and therefore linearity is kept. However, the measured curve doesn't show a linear behaviour. At energies higher than $\sim 12\,\text{keV}$ the signal height even begins to saturate and remains constant after. A reason for this can be a saturation or non linear behaviour of the amplifier in the pixel electronics, discussed in the next section.

9.5 Investigation on Energy-Saturation

As mentioned earlier, a possible reason for the saturation towards higher energies may be the saturation of one amplifier or the source follower in front of the comparator. Therefore threshold scans with different injection voltages were made. By using injection as signal source, the signal is directly processed towards the amplifier and therefore effects of the semiconductor/diodes the particle has to pass normally can be neglected. This ensures that only the amplifier electronics can affect the incoming pulse. The obtained scans were fitted via s-curves with mean μ, noise σ and a additional scaling factor A after Equation 8.3:

$$f(x) = \frac{A}{2}(1 + erf(\frac{x-\mu}{\sqrt{2}\sigma})) \tag{9.3}$$

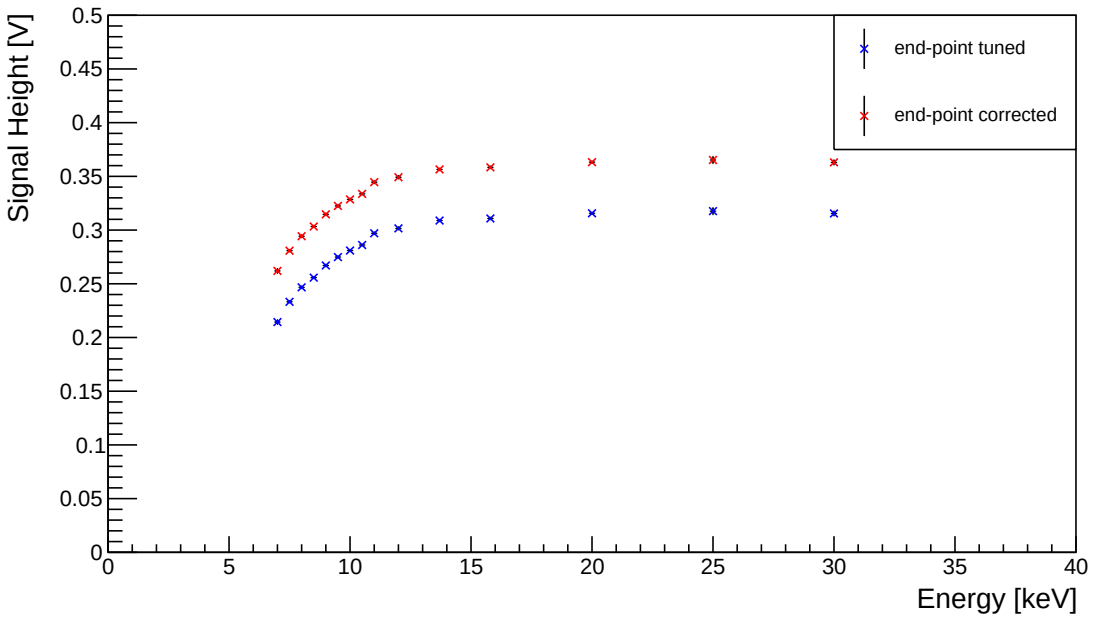

Figure 9.10: Energy calibration curve for a single pixel (25-12) measured with the endpoint energy method.

In Figure 9.11 the determined average signal height is plotted against the injection voltage. Same measurements with a MuPix6, which has the same readout electronics apart from the state machine being external, was done in [2]. There, the signal height showed a linear behaviour over an injection voltage range of 0.5 volt to 1.4 V, as is expected through charge conservation, but different DAC settings were used. Although the beginning of the curve is linear too, at injection voltages of 0.8 V, the signal height stays constant. This measurement result shows, that the electronics does not show a linear response throughout all input voltage regions, if the injection is supposed to be linear. To cross check this behaviour, same injection scans were reproduced with another MuPix7 chip (id: 7736). The results are similar, as seen in Figure 9.11.
For those curves only injection voltages between 0.5 V and 1.1 V could be used. At higher voltages 'pile-ups' appear at the end of the s-curve, which makes them impossible to fit. Additionally, if measured with close voltage steps the curve shows two structures. The cause of those problems couldn't be identified yet. Whereat comparator oscillations as shown in [2] may causing the roll-over of the s-curves.

9.6 Absorption Studies

The cross section for the photoelectric absorption σ_{abs} is energy dependent, as shown in Figure 3.1. Therefore, the mean free path of photons inside silicon is also con-

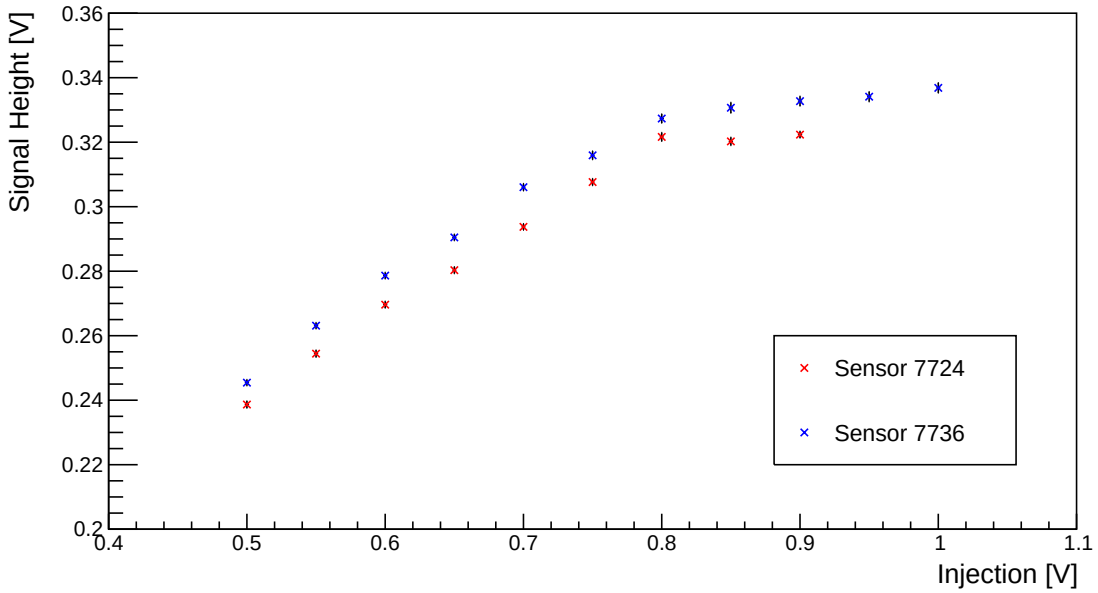

Figure 9.11: Average signal heights for different injection voltages with standard error of the mean for two different sensors.

sidered energy dependent. Photons with different energies are penetrating detector material with varying depths. Obviously not every photon from the continuous spectrum can be detected due to restriction of the sensitive region. In the following simulation studies were made, to see how much the endpoint energy determination is affected.

The initial intensity distribution of the continuous spectrum is approximated with Kramers law [36]:

$$N(E) = Z \cdot I \cdot (E_0 - E) \cdot E \tag{9.4}$$

- $N \rightarrow$ number of photons
- $I \rightarrow$ tube current
- $Z \rightarrow$ number of protons in the nucleus
- $E_0 \rightarrow$ endpoint energy

Multiple photons with random energies underlying the distribution from Equation 9.4 are simulating the X-ray source. For each created photon the corresponding mean absorption length λ is calculated from the photoelectric attenuation coefficient μ based on the data of [37] after [10]:

$$\lambda = \frac{1}{\mu} \tag{9.5}$$

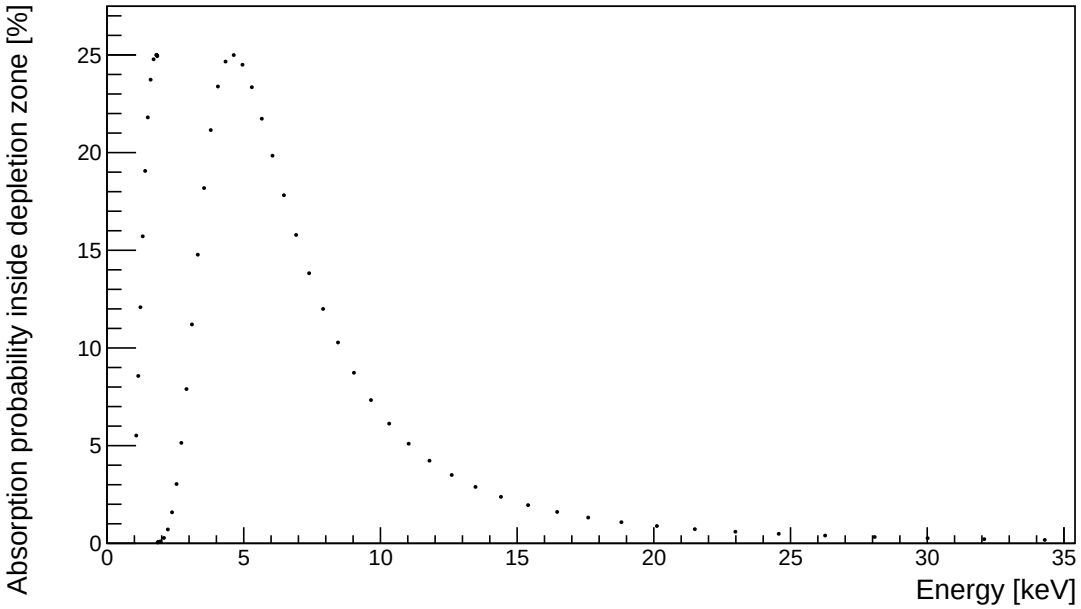

Figure 9.12: Absorption probability of a single photon inside the sensitive sensor area for different energies

The sensitive part of the MuPix is approximated as the depth from $x_1 = 10\,\mu\text{m}$ to $x_2 = 20\,\mu\text{m}$. The exact position and width of the depletion zone is unknown, but the used parameters should be sufficient enough to see qualitative influences. With Equation 3.1, the absorption probability P of a single photon is then:

$$\begin{aligned} P &= A \cdot \int_{x_1}^{x_2} \exp^{-\frac{x}{\lambda}}\ \mathrm{d}x \\ &= A \cdot (-\lambda) \cdot \exp^{-\frac{x}{\lambda}} |_{x_1}^{x_2} \\ &= A \cdot \lambda \cdot (\exp^{-\frac{x_1}{\lambda}} - \exp^{-\frac{x_2}{\lambda}}) \\ \\ 1 &\equiv A \cdot \int_{0}^{\infty} \exp^{-\frac{x}{\lambda}}\ \mathrm{d}x \\ \Leftrightarrow A &= \frac{1}{\lambda} \\ \Longrightarrow\ P &= \exp^{-\frac{x_1}{\lambda}} - \exp^{-\frac{x_2}{\lambda}} \end{aligned} \tag{9.6}$$

The energy dependence of the absorption probability is plotted in Figure 9.12. At an energy of roughly 2 keV a sharp drop can be seen, which is induced by the K absorption edge. Absorption of the photon is determined by the generation of a random number u in the interval $[0, 1]$ and by the comparison with the value P. For $u \leq P$ the photon is absorbed and for $u > P$ it is not. In the resulting intensity distribution of detected photons (Figure 9.13), a smaller slope towards the endpoint

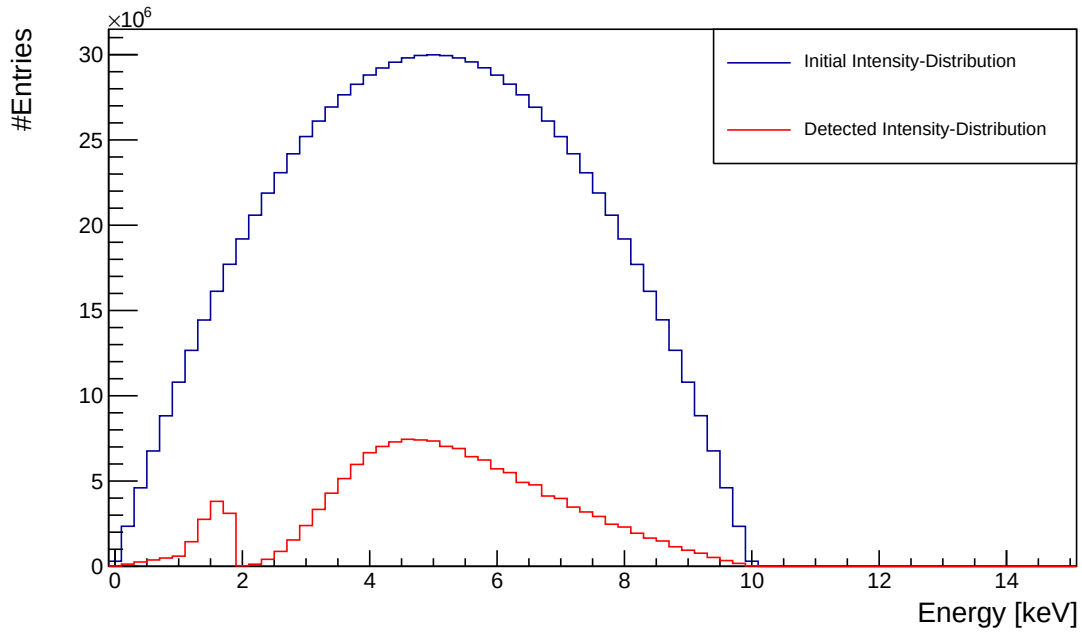

Figure 9.13: Simulation of photon absorption for a continuous spectrum with endpoint energy $E = 10\,\mathrm{keV}$

energy can be seen. This slope is also visible in the threshold scan and is used to determine the endpoint energy. In a idealized case, where noise is not existent, the differing slope does not affect the endpoint energy determination. However, if noise is applied to this intensity distribution, a changed behaviour of the endpoint determination can be expected. The small slope can lead to a systematic overestimation of the signal height, depending on the noise rates of the noise influence. Unfortunately the magnitude of this effect could not be determined due to lack of time during this thesis. Depending on the magnitude, corrections of the signal heights determined through endpoint energy measurements may be necessary and should be investigated in further researches.

9.7 Calibration Fit

As discussed in the section 9.5, the saturation of an amplifier or other electronic components causes a signal height saturation at higher energies. Therefore, the general concept of saturation $\sim (1-\exp^{-x})$ is a reasonable assumption for description of the calibration curve. Due to missing data points in the lower energy range, only extrapolations can be defined. Therefore, this model only gives an estimation of the signal height progression outside the measured area, which motivates the use of a variable energy offset E_0 in the fit. With this it is possible to extrapolate an estimated value for the minimal detectable photon energy of the MuPix. An exact

Parameter	Mean	Sigma	Unit
s_{max}	0.340	0.024	V
E_0	3.27	0.45	keV
F	2.38	0.34	keV
n_{min}	893	123	electrons

Table 9.1: Table with results from Gaussian fit of results distribution from single pixels.

starting point of the calibration cannot be set anyway, because noise dissolves signal heights in the mV-region Applying a scaling factor s_{max} for the maximum signal height and a saturation factor F results in the following fit function:

$$s(E) = s_{max} \cdot (1 - \exp^{\frac{E-E_0}{F}}) \tag{9.7}$$

The fit for the total sensor and distributions of fit parameters can be found in Figure 9.14, whereas corresponding values of the pixel fit distributions are in Table 9.1. The minimal number of created electron hole pairs n_{min} is calculated by dividing the minimal visible energy through the average electron-hole pair creation energy $W = 3.66\,\text{eV}$ [38] in silicon:

$$n_{min} = \frac{E_0}{W} = \frac{E_0}{3.66\,\text{eV}} \tag{9.8}$$

A look at the total sensor calibration curve reveals that the measured region is well described by the fit. However, the intersection with the x axis at about 3 keV doesn't match with the expected minimal detectable energy of the MuPix7, because several systematic effects, for instance the energy dependence of the free mean path length are not taken into account. Photons either deposit their full energy by absorption or proceed further inside the material. For energies below 4 keV, photons are likely to be absorbed before the depletion zone due to a short mean free path length. At this point photons can't be detected, which means that the minimum energy of the fit is only a valid assumption for photons. Other particles, for instance electrons, deposit energy via ionisation or Bremsstrahlung over a distance, which leads to a different energy deposition and therefore different detection behaviour. Additionally, the absorption behaviour of photons lead to a deformation of the continuous X-ray distribution which can cause a systematic uncertainty for the signal height determination, as stated in the section above. When calibration curves of endpoint and fluorescence method are being compared, an offset between signal heights of both methods should appear, if the effect influences the endpoint energy determination. Due to the usage of discrete energies in the fluorescence radiation, only a constant absorption length is given, which cannot create deformations in the intensity distribution. With additional measurement points below 7 keV, a better description of the calibration curve can be achieved. Using fit parameters from single

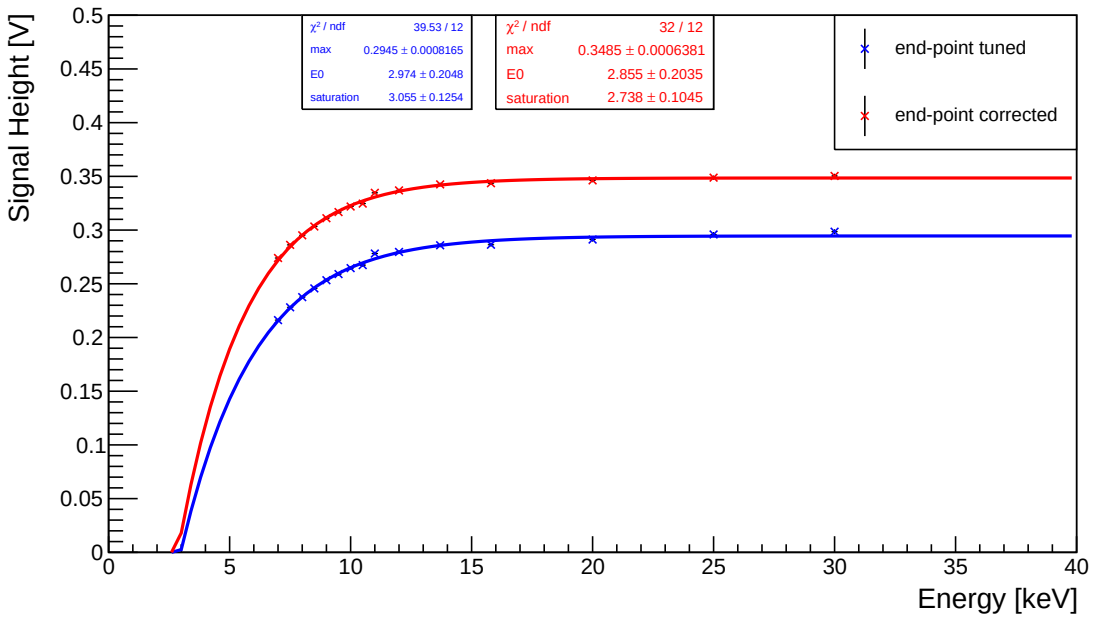

(a) Energy calibration curve with saturation fit for total sensor.

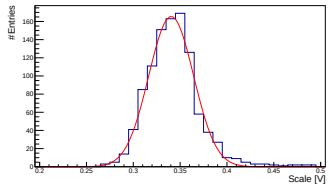

(b) Distribution of maximum signal height s_{max} with Gaussian fit.

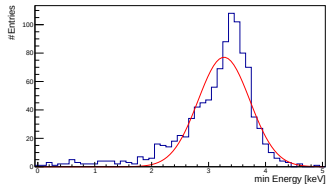

(c) Distribution of energy offset E_0 with Gaussian fit.

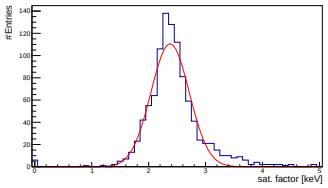

(d) Distribution of saturation factor F with Gaussian fit.

Figure 9.14: Results for endpoint energy calibration

pixels, an average signal height of at least $s = (0.09 \pm 0.02)$V is expected for a 4 keV energy deposition of electrons inside Mu3e under the assumption of using MuPix7 sensors. For the error calculation, error propagation is used with the sigma values of the Gaussian pixel fits due to strong pixel fluctuations.

10 Energy Calibration with X-Ray Fluorescence

As counter draw to the first approach of using endpoint energy from Bremsstrahlung, a second method to achieve an energy calibration is performed. The usage of spectral lines from characteristic spectra via X-ray Fluorescence (XRF) is expected to give more accurate results due to the fact that a lot of effort was put into the exact determination of their energy (ex.: [39]). Additionally, X-ray fluorescence gives the opportunity to measure at lower energy ranges, which is a matter of particular interest because electrons in Mu3e will deposit an energy of about 4 keV.

10.1 Curve Characteristics

At the beginning the shape of the measured curve has to be understood before evaluation and fitting techniques can be used. To get a first impression, a threshold scan with copper ($K_{\alpha 1} = 8.048\,\text{keV}$, [39]) was performed, which is exemplary illustrated in Figure 10.1. A tuned sensor is used for this measurement with the same argumentation as for the endpoint energy method. The main component of the scan response is an s-curve originating from the $K_{\alpha 1}$-line of copper. Other lines from the discrete spectrum cannot be seen due to strong suppression through high differences in intensity and a minimal energy resolution of intrinsic silicon, which is described through the Fano formula [25]:

$$\Delta E \approx 2.35 \cdot \sqrt{F_{Si} \cdot E \cdot W_{Si}} \tag{10.1}$$

- $F_{Si} \rightarrow$ Fano factor of silicon (Table 13.1)
- $W_{Si} \rightarrow$ Average energy needed to create a electron-hole pair in silicon (Table 13.1)

Around the s-curve the scan is behaving linearly. In these parts the continuous spectrum is visible due to Compton scattering at the fluorescence target which is investigated in the next section. Additionally, cross-talk influences the curve at higher thresholds slightly (1-10%), as seen in [35]. Compared to the endpoint energy measurement a strong rise at the end of the curve is not visible, because the measurement range excludes regions dominated by noise.

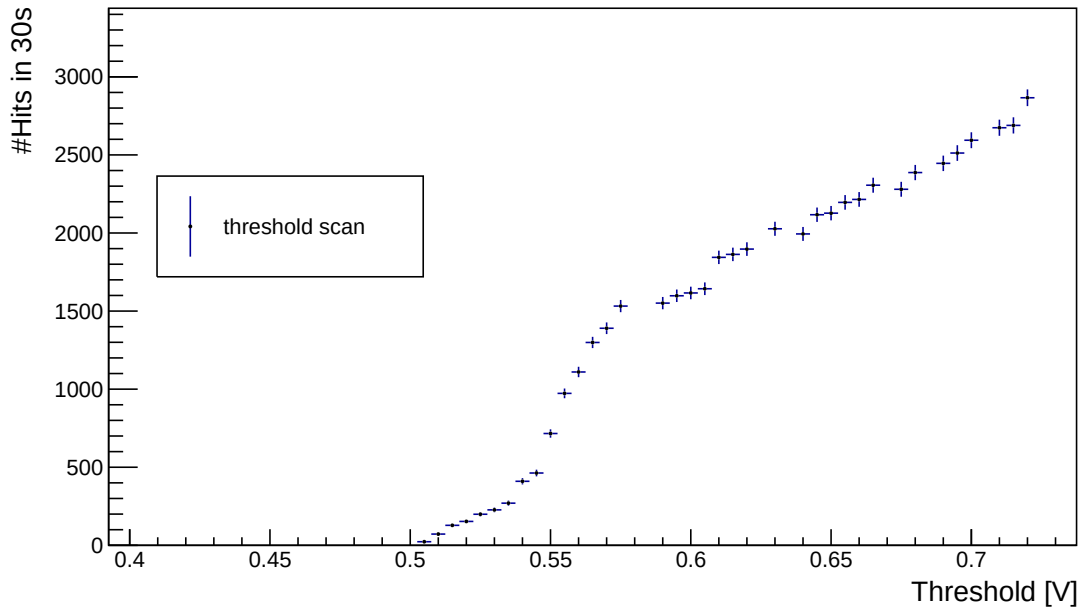

Figure 10.1: Measured XRF curve for total sensor (copper) with tuning

10.2 Background Estimation

Apart from fluorescence radiation, Compton scattered photons contribute with a significant percentage to the incident X-rays. This effect can not be eliminated, because without using the maximum energy ($E = 35\,\text{keV}$) delivered by the X-ray unit, the rate of the pure fluorescence radiation is too low. To analyse the background, a pure aluminium target with a K_α-line at $E \approx 1.5\,\text{keV}$ [39] was used. The energy of the aluminium K_α-line is too small to advance deeply inside silicon due to a high absorption probability and therefore a short free mean path at available rates. Another advantage of choosing aluminium is its equality towards the other fluorescence probes, which consist out of aluminium holders with metallic probes inside. In Figure 10.2 the ToTs of fluorescence measurements from aluminium and titanium are plotted together. Here titanium is chosen, as its K_α-line is at roughly 4.5 keV and therefore the background produced by higher energies can be clearly identified. Both histograms were normalized by scaling with the inverse maximum. Scaling the aluminium again down to the maximum next to the peak in the titan spectrum shows that the aluminium measurement represents the background well. Additionally, the fluorescence aluminium ToTs and the ToTs of the total X-ray tube spectrum are depicted together in Figure 10.3. Here the normalization from aluminium is the same as before and the other histogram is scaled down by the inverse maximum. Both histograms show the same total width. This suggests that the background contains the same energy range as the Bremsstrahlung from the X-ray tube. The distribution of 35 keV-ToTs has a strong peak building up,

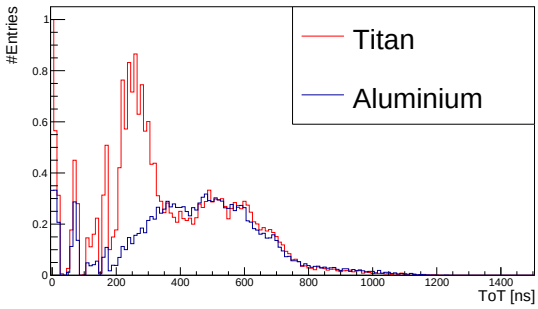

Figure 10.2: Normalized ToT histogram of titanium and aluminium at $U_{thr} = 0.7\,\mathrm{V}$

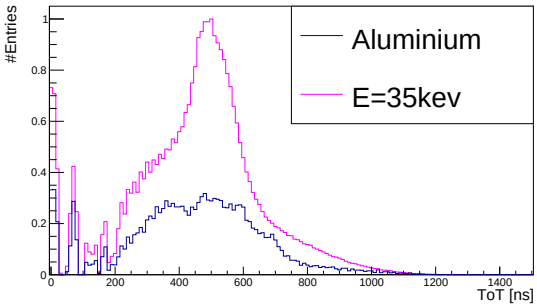

Figure 10.3: Normalized ToT histogram of aluminium and Bremsstrahlung at $E = 35\,\mathrm{keV}$, $U_{thr} = 0.7\,\mathrm{V}$

which is not seen in the aluminium measurement. An explanation for this is the fact that the aluminium histogram has much less entries compared to the other histogram due to the loss of photons in absorption, not accessible scattering angles and not detectable line emissions. Therefore, the real shape of the distribution can't evolve compared to the full spectrum measurement. Also, the threshold scan of the aluminium measurement shows the same endpoint energy and same behaviour in the lower threshold region as the endpoint measurements, displayed in Figure 10.4. Here, both curves are normalized by their integral.
To approximate the background for later uses a linear model is not sufficient in most cases and therefore a polynomial of third order is used as shown in Figure 10.5.

10.3 Fluorescence Calibration

For the energy calibration multiple scans with different materials were made. A table with the used materials and their corresponding fluorescence lines can be found in the appendix. Energies from about 4.5 keV to roughly 22.2 keV were accessible, allowing for measurements with even lower energies compared to the endpoint method. Due to low rates, a measuring time of at least 5 min per data point is needed to gain useful results. Again every pixel is fitted individually. Fitting only the s-curve in the scan data is not feasible due to additional background, which results in increasing slopes at both endings. Therefore, the total measurement region is fitted on purpose. The used fit-function consists of a linear function, which represents the background and a added s-curve. After the s-curve another linear function is added:

$$f(x) = A \cdot (x - B) + \frac{C}{2} \cdot (1 + erf(\frac{x - \mu}{\sqrt{2} \cdot \sigma})) + \Theta(x - D) \cdot E(x - D) \qquad (10.2)$$

- A - slope of linear 1

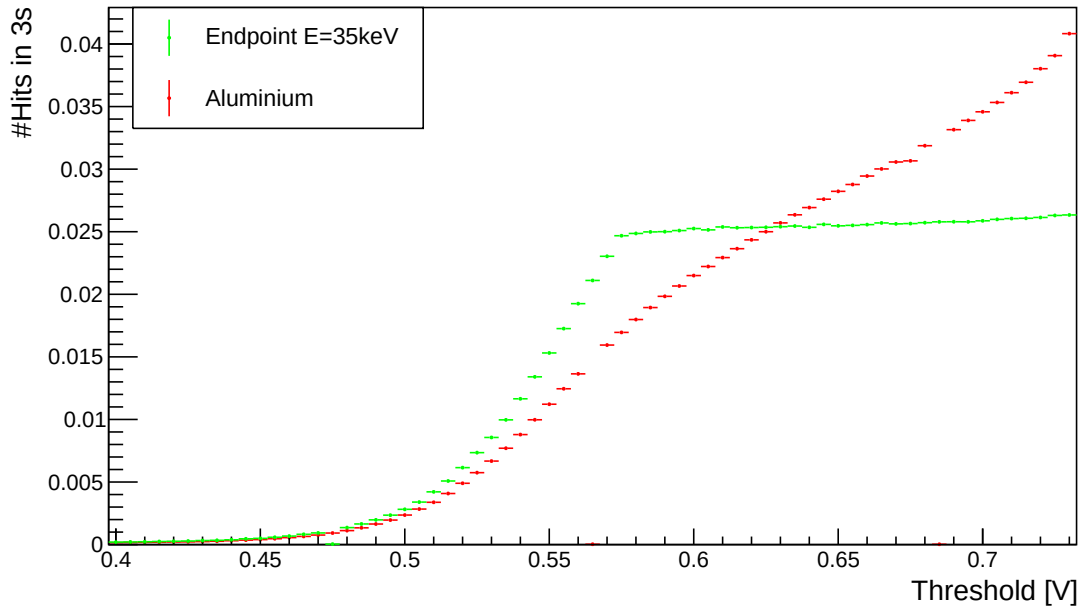

Figure 10.4: Threshold scan of aluminium with fluorescence and a 35 keV scan

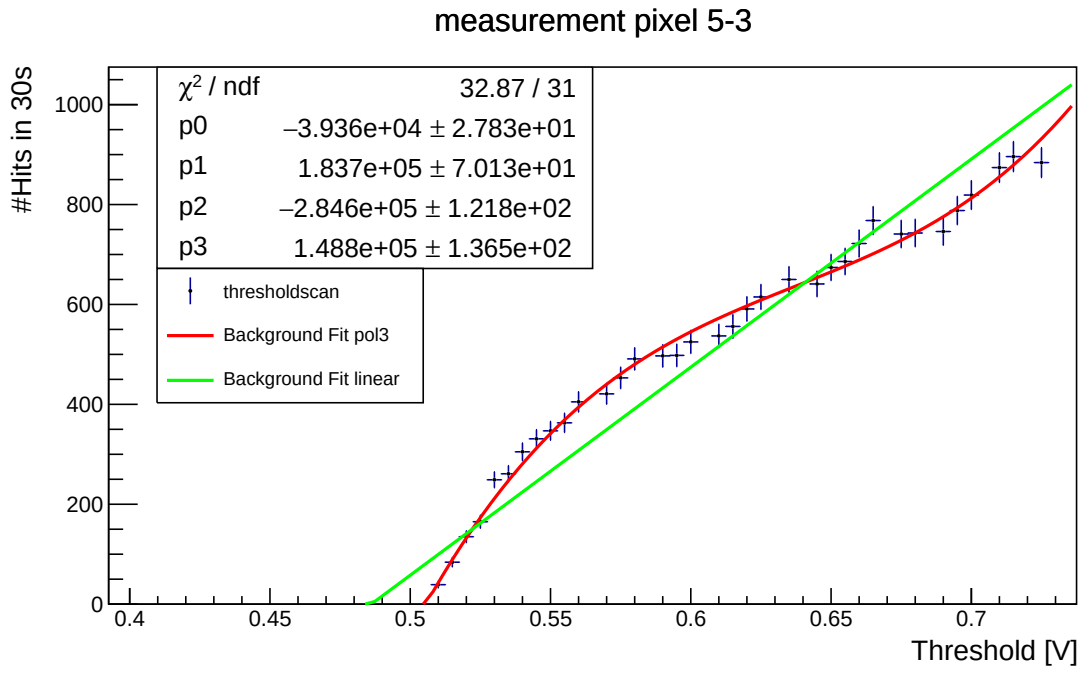

Figure 10.5: Threshold scan of aluminium with fluorescence and approximation through a polynomial

- B - offset in x-direction of linear 1
- C - scale of s-curve
- D - end of s-curve / begin of second slope
- E - slope of linear 2

This approach can't be used on measurements with low energy K_α-lines (titanium and iron), as the background is dominant in leading parts of the curve. A linear slope is not sufficient to describe the background any more. A third degree polynomial is a reasonable empirical background model. Adding an s-curve to this background is a working solution. Multiplication of an additional factor B, respects possible scaling differences between the probes.

$$f(x) = \frac{A}{2} \cdot (1 + erf(\frac{x-\mu}{\sqrt{2}\cdot\sigma})) + B \cdot (p_0 + p_1 x + p_2 x^2 + p_3 x^3) \tag{10.3}$$

- A - scale of s-curve
- B - scale of background
- $p_0 - p_3$ - polynomial coefficients, taken from aluminium measurements and are fixed

Due to the high number of free parameters, both fit methods are likely to fail or give no physical results (for example: $\mu > D$). To prevent this, the fit parameters need seeding to work. Figure 10.6 shows an example for both fitting techniques, whereas examples including pre-fits and fit regions are presented in the appendix. For higher energies both fit methods give insufficient results due to difficulties in recognising s-curve structures due to steep steps and limited threshold scan binning. Therefore, materials with K_α-lines greater than $E \approx 10\,\mathrm{keV}$, except zirconium, were not used in this calibration approach. An exemplary calibration curve is plotted in Figure 10.7.

10.4 Calibration Fit

Fitting of the measured calibration curve is done with the same saturation function (Equation 9.7) and argumentation as for the endpoint approach. The results are displayed in Figure 10.8 and Table 10.1. Again, the minimal number of electrons n_{min} is calculated with Equation 9.8 from E_0.
As visible in Figure 10.8, the χ^2_{red} of the fit is very high, due to an underestimation of the energy error. Fluorescence energies are often determined with high precision [39](for example up to $\Delta E = 0.01\,\mathrm{eV}$). In this thesis errors were approximated to be $\Delta E = 0.001\,\mathrm{keV}$, because not every characteristic line emission inside [39] is given within the exemplified accuracy. But the MuPix can't resolve energies within this

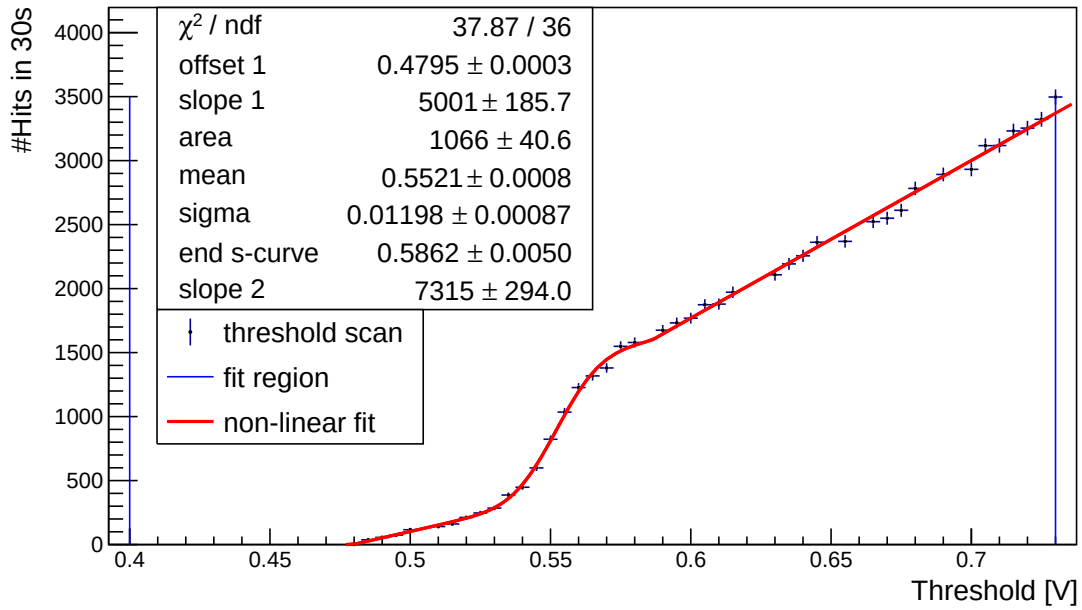

(a) Fluorescence fit with linear approximation for copper, pixel (14,0)

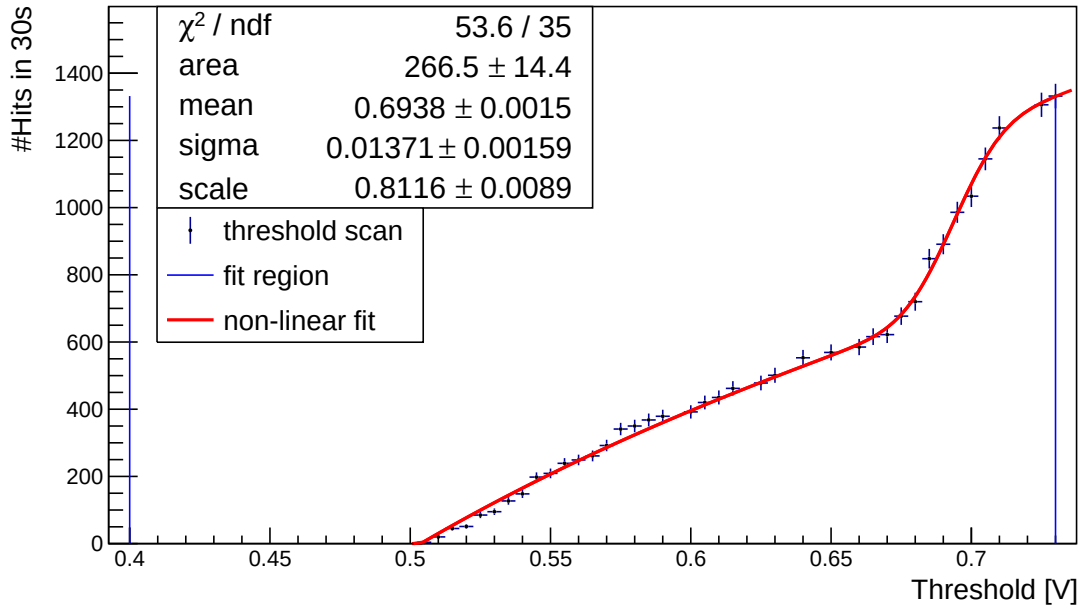

(b) Fluorescence fit with background from aluminium for titanium, pixel (28,0)

Figure 10.6: Fluorescence fits with two different fitting methods

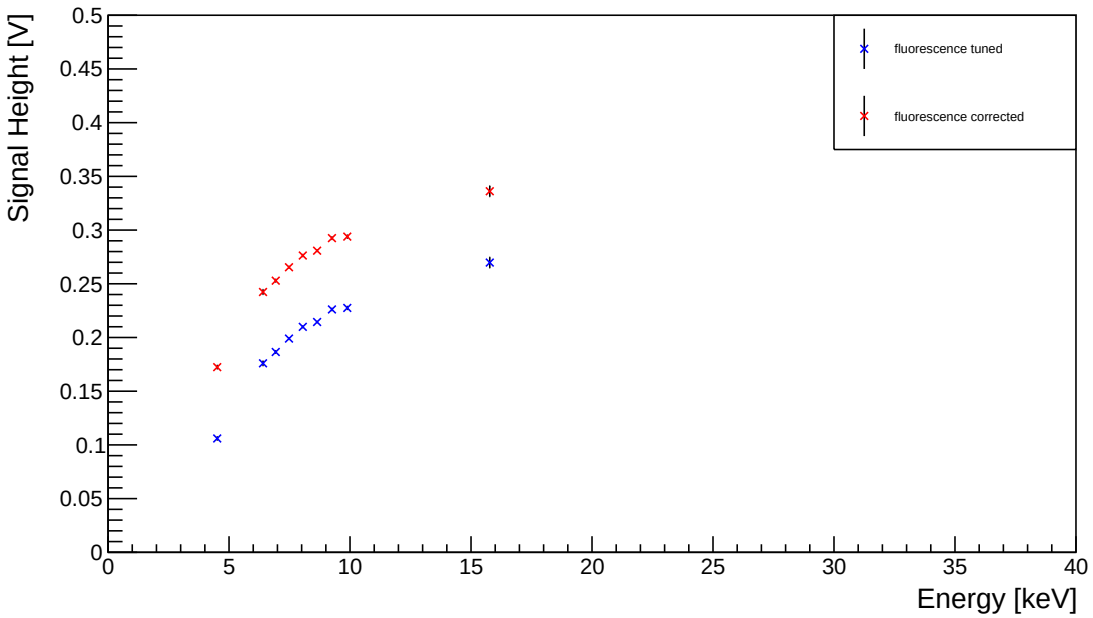

Figure 10.7: Calibration curve with fluorescence method for a single pixel (4,6)

Parameter	Mean	Sigma	Unit
s_{max}	0.334	0.030	V
E_0	2.31	0.36	keV
F	2.69	0.77	keV
$numberofe^-$	631	98	electrons

Table 10.1: Table with results of single pixel distributions

precision, as shown in [1] and described by the intrinsic energy resolution of silicon through Fano [25]. In addition to this, failed fits for higher energies ($> 9.5\,\text{keV}$) are degrading the calibration fit. This is reflected inside the fitted curve, which doesn't stick well to some of the data points. But the saturation assumption is still a good description of the measured data region. With using fit parameters, the average expected signal height of the 4 keV-electrons is at least $s = (0.16 \pm 0.04)0.16\,\text{V}$ for MuPix7, which can be clearly distinguished from noise.

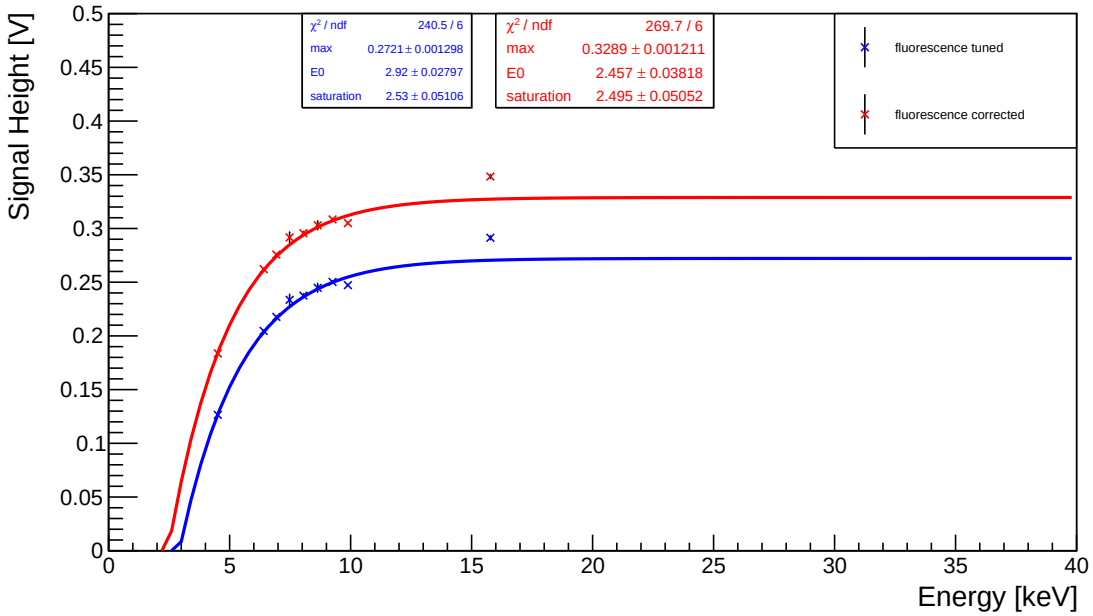

(a) Energy calibration curve with saturation fit for the total sensor.

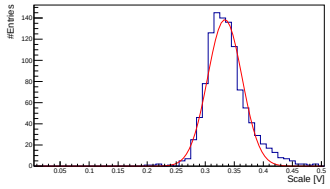

(b) Distribution of maximum signal height s_{max} with Gaussian fit.

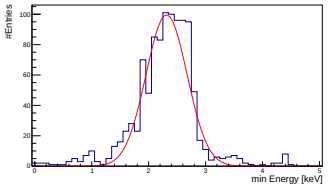

(c) Distribution of energy offset E_0 with Gaussian fit.

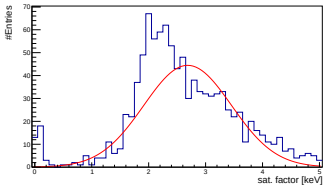

(d) Distribution of saturation factor F with Gaussian fit.

Figure 10.8: Results of fluorescence energy calibration

11 Comparison of Methods

11.1 ToT-Histograms

In the following, ToT histograms of the different methods are being compared. To achieve a comparison, each histogram is scaled to 1 by its maximum. The characteristic shape of the endpoint ToT-histogram (Figure 11.1) is a wandering peak, which has a slow outfall to the left side and a strict fall to the right side. For higher energies a tail to high ToTs is visible. This behaviour is imitating the Bremsstrahlung spectrum, displayed in Figure 7.6. A reason for the peak, seen in ToTs of continuous spectra, is the absorption behaviour of photons. Photons with low and high energy are absorbed with less intensity, which causes the suppression of low and high ToTs and a peaking region. ToT-Histograms from fluorescence measurements, Figure 11.2, behave a bit different. They have the underlying continuous spectrum, as showed in the fluorescence background investigation, with clearly visible peaks coming from the K_α-line emission of the target. In Figure 11.3 the conformity between endpoint ToT and fluorescence peak for close distant energy ranges is recognisable. An energy calibration with ToTs is possible too and already done in [1] and [2]. When knowing pulse heights for corresponding ToTs, a pulse height energy calibration, as done in this thesis, is also possible.
Eye caching phenomena, visible in all measured ToT-histograms, are the spikes in lower ToT ranges up to 200 ns. They are almost always at the same position in every histogram and have same heights for energies close to each other. A reason for this is cross talk [40] which can create low pulse heights, leading to small ToTs in the measured threshold region of 0.7 V.

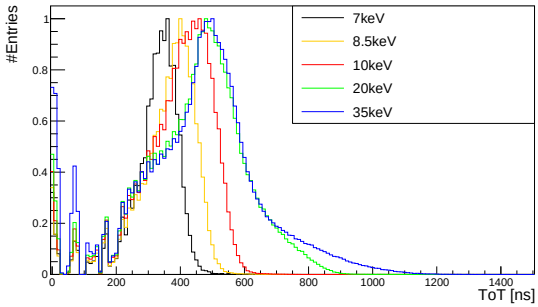

Figure 11.1: ToTs for different endpoint energies at $U_{thr} = 0.7\,\mathrm{V}$

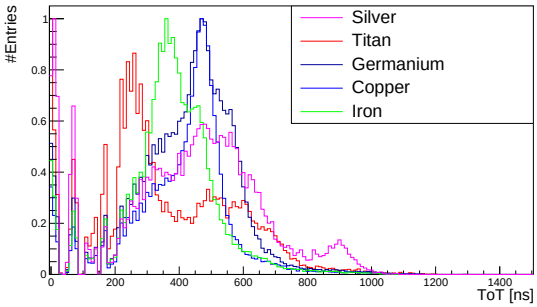

Figure 11.2: ToTs for different fluorescence energies at $U_{thr} = 0.7\,\mathrm{V}$

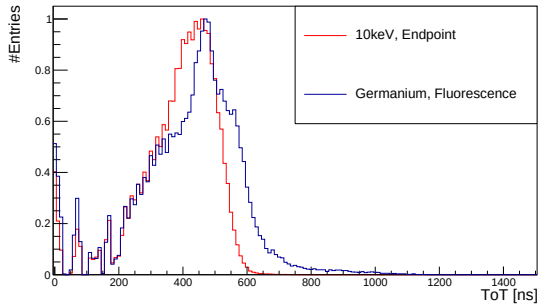

(a) 10 keV and Germanium

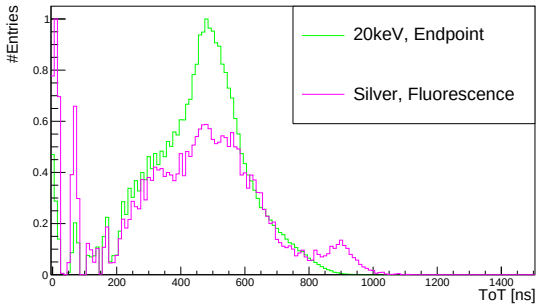

(b) 20 keV and Silver

Figure 11.3: Comparison of ToTs from Endpoint and Fluorescence method with approximately same energies at $U_{thr} = 0.7\,\mathrm{V}$.

11.2 Calibration Curves

To see similarities and differences between calibration curves of endpoint and fluorescence approach, both calibration curves are pictured together in Figure 11.4. Both calibration curves are looking very similar. For the fluorescence method, only a few data points above 9 keV are available and therefore a determination of the maximum signal height can't be done properly as it is possible through endpoint measurements, leading to slightly different saturation levels. In return data points at lower energies, which are making up an sensitive part of the curve, can be better resolved via X-ray fluorescence, resulting in a lower detectable energy. However, very conforming results of both methods can be achieved for several pixels, as exemplified in Figure 11.4. This indicates that the determined signal heights via endpoint regression are slightly, or even better, not influenced through deformation of the intensity distribution via energy dependent absorption lengths. Another visible difference is the fit quality $\chi^2_{red.}$, which is far better for the endpoint method. A reason for this is mostly the bigger energy error of the endpoint data and the stated energy error underestimation of the fluorescence method.

11.3 Combined Calibration

Both methods show, that in general a calibration approach is working and similar curves can be achieved, but different energy ranges are addressed. Using data from both methods, a combined energy calibration over a wide energy range can be determined, as pictured in Figure 11.5. This calibration curve also benefits from a higher number of data points, which will result in a better calibration and reduced errors.
As one can see, values from pixel fits are nicely Gauss distributed with a smaller width, compared to endpoint and fluorescence method results. From the combined calibration fit, a signal height of $s = (0.16 \pm 0.02)\mathrm{V}$ is expected for the 4 keV energy

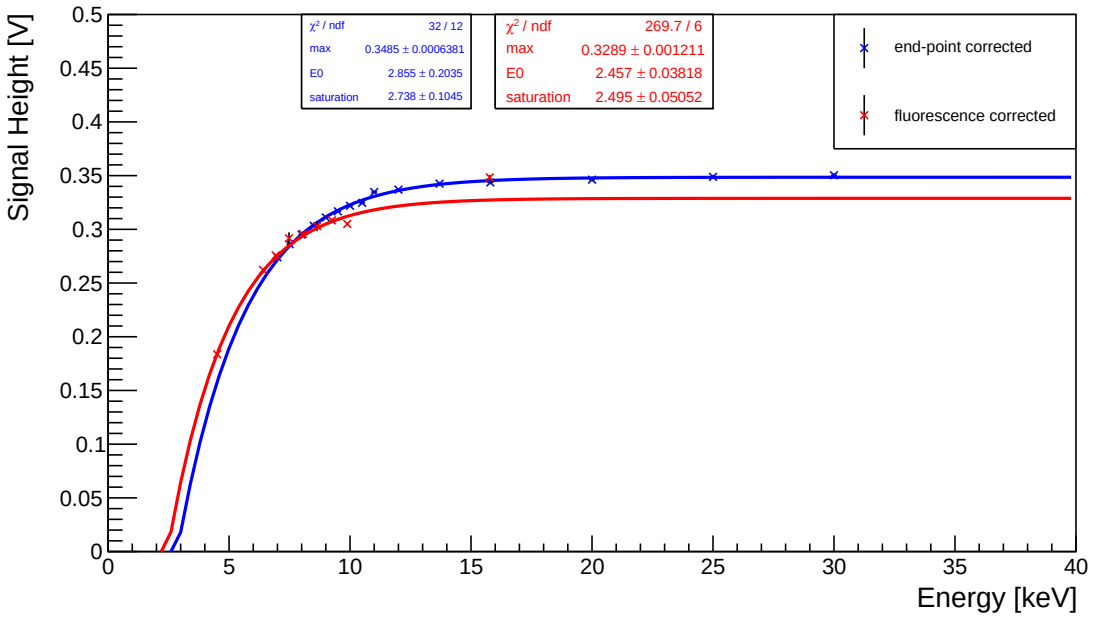

(a) Total Sensor

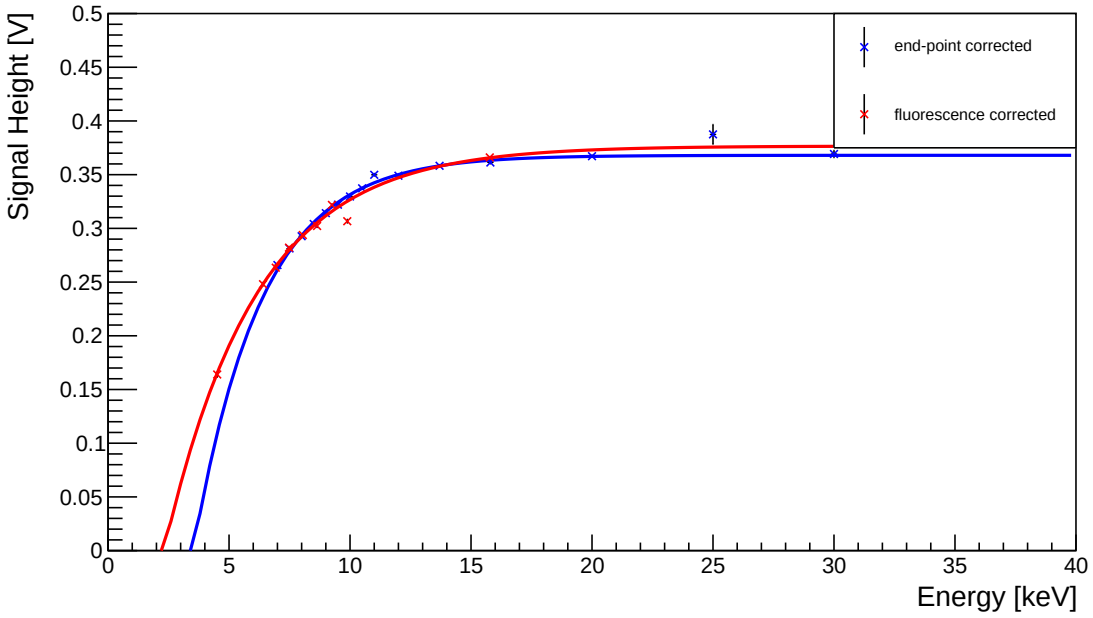

(b) Single Pixel (12,2)

Figure 11.4: Comparison of Energy Calibration curves.

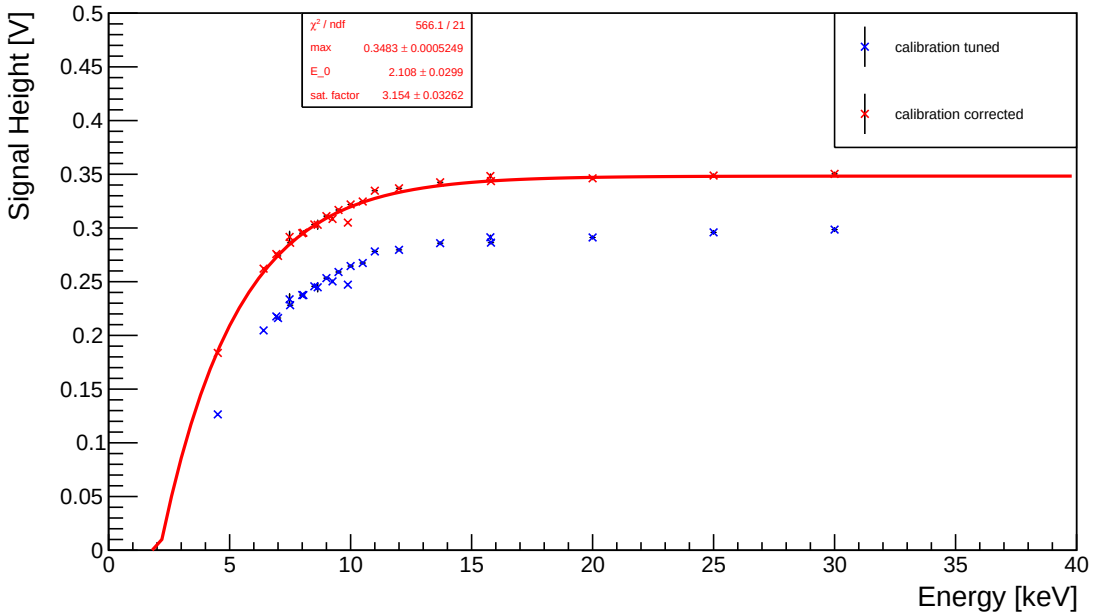

(a) Energy calibration curve with saturation fit for total sensor

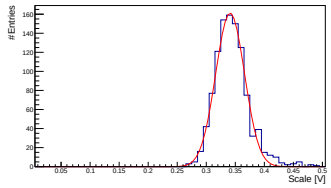

(b) Distribution of maximum signal height s_{max} with Gaussian fit

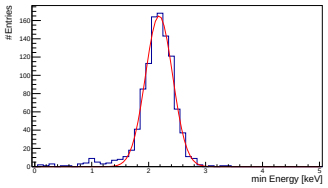

(c) Distribution of energy offset E_0 with Gaussian fit

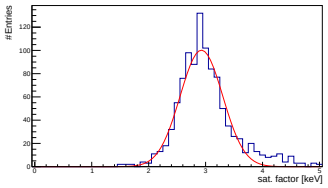

(d) Distribution of saturation factor F with Gaussian fit

Figure 11.5: Results for combined energy calibration

Parameter	Mean	Sigma	Unit
s_{max}	0.341	0.025	V
E_0	2.18	0.24	keV
F	2.93	0.37	keV
$numberofe^-$	596	66	electrons

Table 11.1: Table with results from Gaussian fit of results distribution from single pixels for the combined calibration.

deposition of electrons in Mu3e, under the assumption of using MuPix7.

11.4 Validation

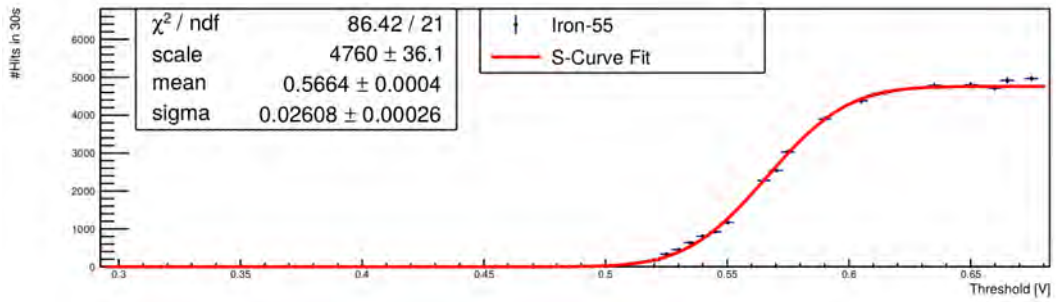

Figure 11.6: Curve of the iron-55 source from a single pixel with s-curve fit (pixel 4-10).

A possibility to check the accuracy of the energy calibration with X-rays, is to take a reference signal with a well known energy. In this case iron-55 is chosen, which is often used to calibrate sensors. The measured threshold scan of iron-55 can be fitted with a scaled s-curve as in equation (8.3), because only the K_α-line is visible. The result for a single pixel is drawn as example in Figure 11.6, whereas the distribution of the signal heights is shown in Figure 11.7. Out of both single calibration methods and the combined one, the minimum expected energy from the measured signal height of the iron source can be calculated. Therefore the inverse of equation (9.7) has to be developed:

$$E(s) = E_0 - F \cdot ln(1 - \frac{s}{s_{max}})$$

$$\Delta E(s) = \sqrt{(\Delta E_0)^2 + (\Delta F \cdot ln(1 - \frac{s}{s_{max}}))^2 + (F\frac{\Delta s}{s - s_{max}})^2 + (F\frac{s \cdot \Delta s_{max}}{s \cdot s_{max} - s_{max}^2})^2} \tag{11.1}$$

- $E(s) \rightarrow$ energy at pulse height s
- $E_0 \rightarrow$ minimal detectable energy
- $F \rightarrow$ saturation factor
- $s_{max} \rightarrow$ maximal pulse height

The resulting values are presented in Table 11.2. Here the energy is taken from the mean of the $E(s)$-distribution and the energy error from the mean of the $\Delta E(s)$-distribution. The endpoint method is the only one, laying within the 2σ range of the expected value of 5.9 keV from iron-55 due to a big error, which is caused by

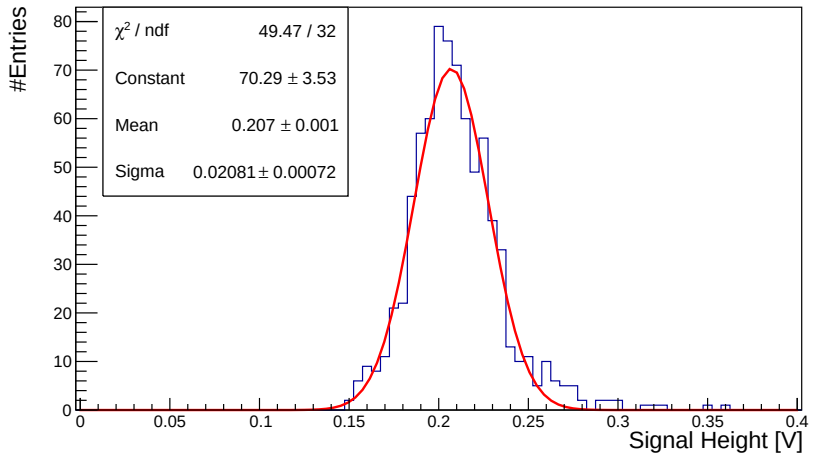

Figure 11.7: Distribution of determined signal heights for iron-55 with Gaussian fit

Method	Value	Error	Unit
Endpoint Energy	5.57	0.26	keV
Fluorescence	5.04	0.11	keV
Combined Calibration	5.08	0.08	keV

Table 11.2: Overview of results for total sensor

lacking data points in the low energy range. Compared to this, the fluorescence and combined calibration results have a significant deviation. As seen in all three variants, the calibrations gave almost lower energy values than expected, because with the saturation fit no exact description of progression for low signal heights is given. Other important influence are the fits of the iron-55 measurement, which doesn't work properly for lots of pixels, especially in the region of the mean from the s-curve. To improve calibration results, the iron-55 measurement could also be considered as another measuring point, mainly because it is in the low energy region, where data points are lacking.

Part V

Discussion

12 Summary & Discussion

12.1 Summary

The energy calibration approach of the MuPix7 was carried out with two different methods using X-ray radiation. The first method takes the endpoint energy of the continuous Bremsstrahlung spectrum, whereas the second method uses characteristic line emissions from X-ray fluorescence as reference. With both approaches, a total energy range from roughly 4.5 keV to 35 keV was accessible.
First curve investigations showed, that sensitive pixels were causing an offset to the curve, which would make fitting of curves more difficult. Random coincidences and effects from the irradiation of the periphery could be excluded. Tuning of the sensor was used to eliminate the big sensitivity differences between pixels successfully, removing the offset created by few active pixels. Tuning measurements were made to calculate the shift for every pixel caused by the tuning. As expected, a linear behaviour between TDAC and shift was seen.
With both methods, calibration curves could be created and corrected by the shift. However, for higher energies a saturation of the pulse height was observed. A reason for this was located in amplifier electronics in front of the comparator, through measurements with different injection voltages. For reproducibility, injection scans were done with a second chip which also shows the same saturation behaviour inside the injection curve. The saturation of the amplifier motivates the fit of an exponential saturation function which describes the data points in the measured regions very well and gives a rough overview in energy ranges lacking data points. Both methods yielding similar results. Using data points from both methods a combined calibration was achieved. For this, the expected signal height for electrons in Mu3e is 0.16 V. With an iron-55 source, a consistency check of calibration curves was presented.

12.2 Discussion

As the results show, for both methods an energy calibration is possible. However, a general problem which prohibits precise results is the limited rate of the available X-ray tube. As a consequence of this circumstance, fits for threshold scans of single pixels often fail or gave even wrong results due to barely visible structures and strong fluctuations of data points. With a high rate X-ray tube or enough measuring time, the curve and fit quality can be strongly improved. In case of need shorter measurement ranges would help at time issues. In addition to this, a higher rate of X-rays may help to identify K_β-lines. With those, a calibration could be achieved with less

measurements or a wider range of energies could be covered. Due to the low rate and the bad energy resolution of the MuPix, the advantage of precise energy emissions from X-ray fluorescence could not really be exploited, but is still the best way to get exact calibration curves and should be used in further calibration approaches, too. With using the endpoint energy, also very conforming results are possible, but they are limited by X-ray unit resolution and different mean free paths of photons in silicon. Advantageous of using this method is its simplicity. Measurements can be performed swiftly and only a linear fit is needed to get data for the calibration curve. Compared to the necessary effort, good calibration results were achieved. The disadvantage of this method, as highlighted in this thesis, is the accessible energy range. Only energies down to 7 keV were be achieved, which doesn't give a sufficient range for low energies. With the usage of fluorescence lower energies were possible, but the corresponding elements needed for this were not available, except titanium. Another big influence on both calibration approaches not covered in this thesis is the temperature, which affects the pulse height and therefore the calibration as measured in [26]. Within the used single setup a constant environmental temperature could not be guaranteed due to a not isolated setup. To prevent negative effects of the temperature on the measurement, following calibration measurements should be done in a more temperature stable environment. Also it has to be considered that the energy calibration curve does not represent energies below 3 keV well due to total absorption of photons. One measurement below 3 keV would be possible, because the K absorption edge of silicon (at roughly 1.8 keV) leads to a sharp drop in the photoelectric cross section and thus a higher mean free path (see Figure 13.2), which can be exploited. Its questionable, if the signal height can be distinguished from noise. The approximation of the minimum detectable energy is therefore only valid for photons and the real value should be closer to zero.

12.3 Outlook

In further calibration approaches, also Bragg reflection should be taken into account as a third X-ray calibration method. Furthermore the absorption behaviour of Bremsstrahlung should be simulated more precisely to achieve possible correction factors for the endpoint calibration method. Also, the coverage of low energy ranges would be an interesting investigation, especially to measure the minimal detectable energy. Additionally, the usage of a more powerful X-ray unit is recommended.

Part VI

Appendix

13 Appendix

13.1 Properties of Silicon

Property		Value	Unit
Atomic number	Z	14	
Nucleon number		28.09	
Density	ρ	2.33	g/cm^3
Dielectric Constant	ϵ	11.9	
Band gap	indirect	1.12	eV
Electron-hole pair creation energy	W	3.66	eV
Fano factor	F	0.115	
Mobility	μ_n	1450	cm^{2}s/V
	μ_p	500	cm^{2}s/V

Table 13.1: Physical Attributes of Silicon [25], [38], [41], [42], [43], [44]

13.2 DAC-Values

Bias Voltage	Origin	Circuit Part	Function	Effect
VN	DAC	CSA	Current Source	On/Off switch steers current
VNLoad	DAC	CSA	Voltage divider	adjusts amplification
VPCasc	External	CSA		
VNFB	DAC	CSA	Resistance	linear CSA feedback
VNFoll	DAC	SF	Current source	SF output voltage control

Table 13.2: Overview of pixel bias voltages taken from [45]

Bias Voltage	Origin	Circuit Part	Function	Effect
VN2	DAC	Amp2	Current Source	On/Off switch steers current
VNLoad2	DAC	Amp2	Voltage divider	adjusts amplification
VPCasc	External	Amp2		
VNFB2	DAC	Amp2	Resistance	linear CSA feedback
VPComp	DAC	Comparator	Current source	Current & speed control On/Off switch
BL	External	Comparator	Baseline	Voltage offset for signal Comparator input
THR	External	Comparator	Threshold	Comparator reference
BLRes	DAC	Comparator	Resistance	Shaping
VPDAC	DAC	Comparator		Tuning
VNDel	DAC	Edge detector		Delay

Table 13.3: Overview of periphery bias voltages taken from [45]

13.3 MuPix Measurement Settings

DAC	Value [dec]	Value [hex]
VN	20	0x14
VNLoad	4	0x4
VNFB	8	0x8
VNFoll	10	0xA
VNDel	10	0xA
VN2	20	0x14
VNLoad2	4	0x4
VNFB2	8	0x8
VPComp	20	0x14
VPDAC	10	0xA
BLRes	10	0xA
BLRes2	10	0xA
THRes	0	0x0

Setting	Value	Unit
HV	-60	V

Table 13.4: DAC-Settings for MuPix 7224, also reffered as LMPS and additional settings

13.4 Materials for X-Ray Fluorescence

Material	Symbol	$K_{\alpha 1}$ [keV]	$K_{\beta 1}$ [keV]
Aluminium	Al	1.487	1.557
Titanium	Ti	4.511	4.923
Iron	Fe	6.404	7.058
Cobalt	Co	6.930	7.649
Nickel	Ni	7.478	8.265
Copper	Cu	8.048	8.905
Zinc	Zn	8.639	9.572
Gallium	Ga	9.252	10.264
Germanium	Ge	9.886	10.982
Zirconium	Zr	15.775	17.668
Molybdenum	Mo	17.479	19.608
Silver	Ag	22.163	24.942

Table 13.5: Materials for X-ray fluorescence available in this thesis with data from [39]

13.5 Prefits

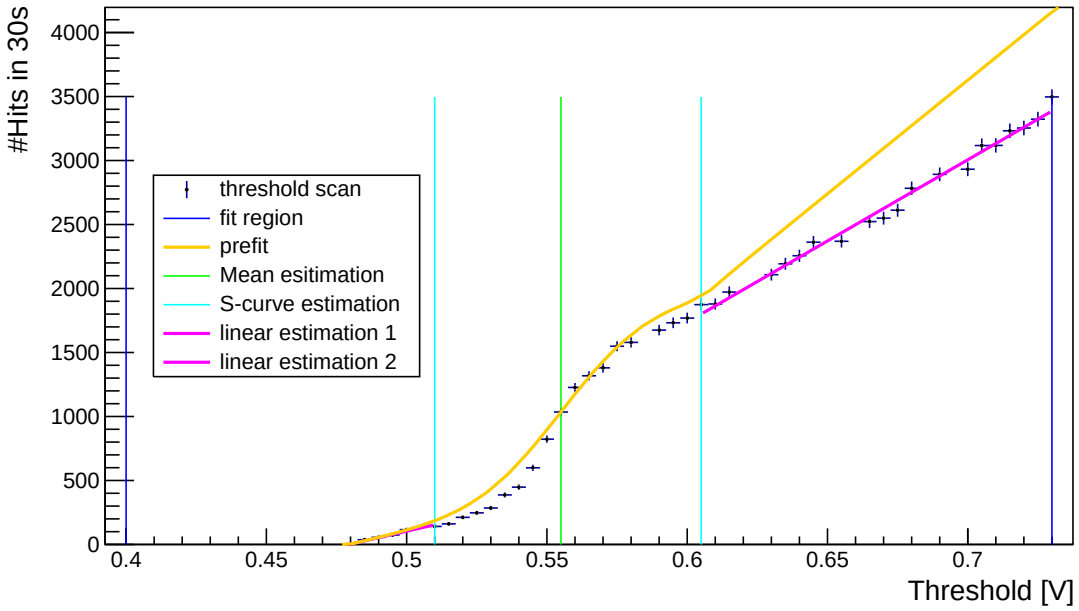

Figure 13.1: Exemplary pre-fit for copper.

13.6 Mean Free Path in Silicon

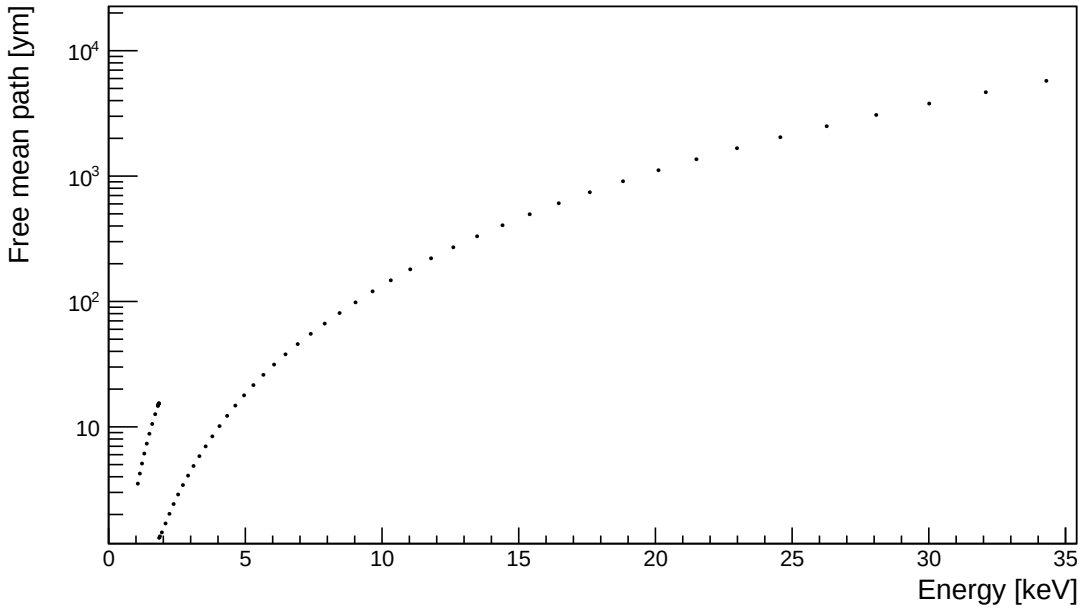

Figure 13.2: Energy dependency of free mean path in silicon

14 Bibliography

[1] Ann-Kathrin Perrevoort. *Characterisation of High Voltage Monolithic Active Pixel Sensors for the Mu3e Experiment*. Master Thesis, University Heidelberg, **2012**.

[2] Jan Hammerich. *Studies of HV-MAPS Analog Performance*. Bachelor Thesis, University Heidelberg, **2015**.

[3] W. J. Marciano, T. Mori and J. M. Roney. *Charged Lepton Flavor Violation Experiments*. *Ann.Rev.Nucl.Part.Sci.*, **58**: pp. 315–341, **2008**. doi: 10.1146/annurev.nucl.58.110707.171126.

[4] Wikimedia Commons. *Standard Model of Elementary Particles*. https://upload.wikimedia.org/wikipedia/commons/0/00/Standard_Model_of_Elementary_Particles.svg, **2017**. [accessed 11-July-2017].

[5] G. Aad *et al.* (ATLAS Collaboration). *Observation of a new particle in the search for the Standard Model Higgs boson with the ATLAS detector at the LHC*. **2012**. 1207.7214.

[6] Christopher W. Walter. *The Super-Kamiokande Experiment*. **Feb 2008**. URL: https://arxiv.org/pdf/0802.1041.pdf.

[7] Y. Kuno and Y. Okada. *Muon decay and physics beyond the standard model*. *Rev. Mod. Phys.*, **73**: pp. 151–202, **2001**. hep-ph/9909265.

[8] C. Patrignani et al. (Particle Data Group). *The Review of Particle Physics. Chinese Physics C, 40, 100001 (2016)*, **2016**.

[9] A. Blondel *et al.* *Research Proposal for an Experiment to Search for the Decay $\mu \to eee$*. *ArXiv e-prints*, **January 2013**. 1301.6113.

[10] H. Kolanoski N. Wermes. *Teilchendetektoren - Grundlagen und Anwendung*. Springer-Verlag Berlin Heidelberg 2016, **2016**. ISBN: 978-3-662-45349-0.

[11] Nation Institute of Standards and Technology. *XCOM: Photon Cross Sections Database*. https://www.nist.gov/pml/xcom-photon-cross-sections-database, **2017**. [accessed 27-August-2017].

[12] J. Ashkin H. A. Bethe. *Passage of radiation through matter*. *Nucl. P*, **1**: p. 253, **1953**.

[13] Stephen M. Seltzer and Martin J. Berger. *Improved procedure for calculating the collision stopping power of elements and compounds for electrons and positrons. The International Journal of Applied Radiation and Isotopes*, **35**, 7, **1984**. URL: http://www.sciencedirect.com/science/article/pii/0020708X84901133.

[14] William R. Leo. *Techniques for nuclear and particle physics experiments*. Springer, **1987**. ISBN: 3-540-17386-2 ; 0-387-17386-2 ; 978-0-387-17386-3 ; 978-3-540-17386-1.

[15] B. Beckhoff B. Kangiesser N. Langhoff R. Wedell H. Wolff (Eds.). *Practical X-Ray Fluorescence Analysis*. Springer-Verlag Berlin Heidelberg, **2006**. ISBN: 978-3-540-28603-5.

[16] H. A. Kramers. *XCIII. On the theory of X-ray absorption and of the continuous X-ray spectrum. Philosophical Magazine*, **46**, 275: pp. 836–871, **1923**. doi:10.1080/14786442308565244. http://dx.doi.org/10.1080/14786442308565244, URL: http://dx.doi.org/10.1080/14786442308565244.

[17] Dr. Katarzyna Skorupska. *Intrinsic Semiconductors*. lecture notes. Accessed: 2017-09-12.

[18] Markus A. Hennig. *Dotierung im zweidimensionales Siliziumkristallgitter mit Phosphor*. https://de.wikipedia.org/wiki/Datei:Schema_-_n-dotiertes_Silicium.svg, **2017**. [accessed 29-August-2017].

[19] Markus A. Hennig. *Dotierung im zweidimensionales Siliziumkristallgitter mit Aluminium*. https://de.wikipedia.org/wiki/Datei:Schema_-_p-dotiertes_Silicium.svg, **2017**. [accessed 29-August-2017].

[20] Wolfgang Demtröder. *Experimentalphysik 3 - Atome, Moleküle und Festkörper*. Springer-Verlag Berlin Heidelberg 1996, 2000, 2005, 2010, 2016, **2016**. ISBN: 978-3-662-49093-8.

[21] Rudolf P. Huebner. *Conductors, Semiconductors, Superconductors*. Springer International Publishing Switzerland 2015, 2016, **2016**, second edition edition. ISBN: 978-3-319-24008-4.

[22] Heiko Augustin. *Characterization of a novel HV-MAPS Sensor with two Amplification Stages and first examination of thinned MuPix Sensors*. Master Thesis, University Heidelberg, **2014**.

[23] I. Perić. *A novel monolithic pixelated particle detector implemented in high-voltage CMOS technology. Nucl.Instrum.Meth.*, **A582**: p. 876, **2007**. doi: 10.1016/j.nima.2007.07.115.

[24] Phillip E. Allen and Douglas R. Holberg. *CMOS analog circuit design*. Oxford University Press, New York, NY [u.a.], **2012**, international 3. ed. edition. ISBN: 978-0-19-993742-4.

[25] Helmuth Spieler. *Semiconductor detector systems*. Series on semiconductor science and technology ; 12 ; Oxford science publications ; Series on semiconductor science and technology. Oxford Univ. Press, Oxford [u.a.], **2008**, repr. edition. ISBN: 978-0-19-852784-8.

[26] David Immig. *Charakterisierung des VCO, der PLL und der Pulsform des MuPix7 in Abhängigkeit der Umgebungstemperatur*. Bachelor Thesis, University Heidelberg, **2016**.

[27] Keithley Instruments Inc. *High Voltage Sourcemeter 2600 B*.

[28] HAMEG Instruments. *Power supply HMP 4030 HMP 4040*.

[29] Boost. *B c++ libraries*, **2017**. URL: http://www.boost.org/.

[30] The Qt Company. *Qt*, **2017**. URL: http://qt.io/.

[31] CERN. *ROOT Data Analysis Framework*, **2017**. URL: http://root.cern.ch/.

[32] PHYWE. *Operating Instructions for the PHYWE XR 4.0 expert unit, X-ray unit, 35kV*. URL: http://repository.phywe.de/files/bedanl.pdf/09057.99/d/0905799d.pdf.

[33] PHYWE. *Characteristic X-Radiation of Tungsten*. URL: http://repository.phywe.de/files/versuchsanleitungen/p2542801/e/p2542801e.pdf.

[34] Huo Junde. http://www.nndc.bnl.gov/nudat2/indx_dec.jsp, **2008**. Nuclear Data Sheets 109, 787 (2008) - National Nuclear Data Center, Brookhaven National Laboratory [accessed 7-August-2017].

[35] Renè Hagdorn. *Performance Optimization for the MuPix7 Sensor Prototype*. Master Thesis, University Heidelberg, **2017**.

[36] E Andrade and M Castañeda. *A model to describe the bremsstrahlung spectrum produced by a positive-ion Van de Graaff accelerator*. *Nuclear Inst. and Methods in Physics Research, A*, **328**, 1: pp. 68–71, **1993**. ISSN: 0168-9002 and 1872-9576.

[37] Nation Institute of Standards and Technology. *X-Ray Form Factor, Attenuation and Scattering Tables*. https://physics.nist.gov/PhysRefData/FFast/html/form.html, **2017**. [accessed 11-September-2017].

[38] F. Scholze, H. Henneken *et al.* *Determination of the electron-hole pair creation energy for semiconductors from the spectral responsivity of photodiodes.* *Nuclear Instruments and Methods in Physics Research Section A: Accelerators, Spectrometers, Detectors and Associated Equipment*, **439**, 2-3: pp. 208 – 215, **2000**. ISSN: 0168-9002. doi:http://dx.doi.org/10.1016/S0168-9002(99)00937-7. URL: http://www.sciencedirect.com/science/article/pii/S0168900299009377.

[39] *X-Ray Data Booklet*. http://cxro.lbl.gov//PDF/X-Ray-Data-Booklet.pdf, **September 2009**.

[40] Heiko Augustin. *ToT Distributions Crosstalk*. Internal Communication.

[41] National Center for Biotechnology Information. *PubChem Compound Database; CID=5461123*. https://pubchem.ncbi.nlm.nih.gov/compound/5461123, **2017**. [accessed Sept. 3, 2017].

[42] Martin A. Green. *Intrinsic concentration, effective densities of states, and effective mass in silicon.* *Journal of Applied Physics*, **67**, 6: pp. 2944–2954, **1990**. doi:http://dx.doi.org/10.1063/1.345414. URL: http://scitation.aip.org/content/aip/journal/jap/67/6/10.1063/1.345414.

[43] B.G. Lowe and R.A. Sareen. *A measurement of the electron-hole pair creation energy and the Fano factor in silicon for 5.9keV X-rays and their temperature dependence in the range 80-270K.* *Nuclear Instruments and Methods in Physics Research Section A: Accelerators, Spectrometers, Detectors and Associated Equipment*, **576**: pp. 367 – 370, **2007**. ISSN: 0168-9002. doi:http://dx.doi.org/10.1016/j.nima.2007.03.020. URL: http://www.sciencedirect.com/science/article/pii/S016890020700527X.

[44] H. Philipp and E. Taft. *Optical Constants of Silicon in the Region 1 to 10 ev.* *Phys. Rev.*, **120**: pp. 37–38, **Oct 1960**. doi:10.1103/PhysRev.120.37. URL: http://link.aps.org/doi/10.1103/PhysRev.120.37.

[45] Heiko Augustin. *Charakterisierung von HV-MAPS*. Bachelor Thesis, University Heidelberg, **2012**.

[46] R. R. Crittenden, W. D. Walker and J. Ballam. *Radiative Decay Modes of the Muon.* *Phys. Rev.*, **121**: pp. 1823–1832, **Mar 1961**. doi:10.1103/PhysRev.121.1823. URL: http://link.aps.org/doi/10.1103/PhysRev.121.1823.

[47] Daniel Laguitton and William Parrish. *Experimental Spectral Distribution versus Kramers' Law for Quantitative X-Ray Fluorescence by the Fundamental Parameters Method.* *X-Ray Spectrometry, VOL. 6, NO. 4, 1977*, (pp. 201–203), **1977**.

[48] Mark Thomson. *Modern particle physics*. Cambridge University Press, Cambridge [u.a.], **2013**. ISBN: 978-1-107-03426-6 and 1-107-03426-4. Hier auch später erschienene, unveränderte Nachdrucke.

14.1 List of Figures

2.1 Table of elementary particles in the Standard Model [4] 12
2.2 SM Feynman graph of muon decay via neutrino oscillation 13
2.3 Feynman graph of internal conversion. 14
2.4 Combination of Michel decay and electron. 14
2.5 Detector concept for the Mu3e experiment 15
2.6 Experimental hall of the PSI with the πE5 beam. 16

3.1 Photon cross sections in silicium, based on data of [11] 18
3.2 Mean energy loss in different materials [8] 19
3.3 Different contributions of energy loss for electrons in lead [8] 20
3.4 Graphical visualisation of multiple Coulomb scattering by [8] 21

4.1 Spectrum of X-ray tube with tungsten anode [15] 23

5.1 Band model for different conductor types [17] 25
5.2 N doping of silicium [18] 26
5.3 P doping of silicium [19] 26
5.4 pn-junction and energy bands with different external voltages from [10]: a) no voltage b) forward bias c) reverse bias 26
5.5 Drawing of the HV-MAPS design [23] 28

6.1 MuPix 7 Sensor Layout 30
6.2 Layout of MuPix 7 pixel 30
6.3 Read-Out Electronic of MuPix7 31
6.4 Pulse-Shaping of MuPix7 32
6.5 Pulse shapes for different time constants ($\tau_{diff} = 100\,\text{ns}$, left) and ($\tau_{int} = 10\,\text{ns}$, right) after [25] 33

7.1 The single setup with the x-ray spectrometer (green), the sourcemeter (red) and the power supply (blue) 35
7.2 Picture of the PCB with colored components, taken from [26] and edited. (yellow) MuPix7, (light green) carrier socket, (black) single LVDS, (blue) low voltage, (red) high voltage, (purple) hitbus, (pink) readout/control, (orange) clock, (cyan) injection 36
7.3 Screenshot of the GUI from the single setup software with different constituent parts colored from [26]. (orange) Board DACs, (black) Chip DACs, (light green) Monitoring, (cyan) Testbeam Control, (blue) Information Console, (red) Clock, (magenta) Measurements, (dark green) Additional Controls 37
7.4 Fixture for the PCB 38
7.5 X-ray fluorescence probe holder and example probes 38
7.6 Measured X-ray spectrum by the vendor of the X-ray unit for a tube (tungsten) voltage of $U_{tube} = 35\,\text{kV}$ with Bragg reflection [33] 38

8.1 Schematic of the ToT . . . 41
8.2 Smearing of the signal to an s-curve . . . 42
8.3 Positioning of Mupix sensor in the X-ray setup for different measurement methods . . . 43
8.4 Decay scheme of the radioactive iron-55 source . . . 44

9.1 Threshold scan for 10 keV . . . 47
9.2 Hitmaps for different parts of the chip being irradiated separately with collimated X-rays at a threshold of 0 V and a endpoint energy of $E = 10\,\mathrm{keV}$ . . . 48
9.3 Number of detected hits as function of the tube current with a linear fit . . . 49
9.4 Hitmap at $U_{thr} = 0\,\mathrm{V}$ for $E = 10\,\mathrm{keV}$ without tuning of the sensor . . . 49
9.5 Hit rate of pixel (7,30) as function of the TDAC for different VPDACs at $U_{thr} = 0\,\mathrm{V}$ . . . 50
9.6 Threshold distributions for 1 Hz noise . . . 50
9.7 Results from the shift calculation . . . 51
9.8 Profile of TDAC-Shift correlation with linear fit. . . . 52
9.9 Approximation of the position of the endpoint energy in measured threshold scan at $E = 8.5\,\mathrm{keV}$ for pixel 19-20 . . . 53
9.10 Energy calibration curve for a single pixel (25-12) measured with the endpoint energy method. . . . 54
9.11 Average signal heights for different injection voltages with standard error of the mean for two different sensors. . . . 55
9.12 Absorption probability of a single photon inside the sensitive sensor area for different energies . . . 56
9.13 Simulation of photon absorption for a continuous spectrum with endpoint energy $E = 10\,\mathrm{keV}$ . . . 57
9.14 Results for endpoint energy calibration . . . 59

10.1 Measured XRF curve for total sensor (copper) with tuning . . . 61
10.2 Normalized ToT histogram of titanium and aluminium at $U_{thr} = 0.7\,\mathrm{V}$ 62
10.3 Normalized ToT histogram of aluminium and Bremsstrahlung at $E = 35\,\mathrm{keV}$, $U_{thr} = 0.7\,\mathrm{V}$ . . . 62
10.4 Threshold scan of aluminium with fluorescence and a 35 keV scan . . . 63
10.5 Threshold scan of aluminium with fluorescence and approximation through a polynomial . . . 63
10.6 Fluorescence fits with two different fitting methods . . . 65
10.7 Calibration curve with fluorescence method for a single pixel (4,6) . . . 66
10.8 Results of fluorescence energy calibration . . . 67

11.1 ToTs for different endpoint energies at $U_{thr} = 0.7\,\mathrm{V}$ . . . 68
11.2 ToTs for different fluorescence energies at $U_{thr} = 0.7\,\mathrm{V}$ . . . 68

11.3 Comparison of ToTs from Endpoint and Fluorescence method with approximately same energies at $U_{thr} = 0.7\,\mathrm{V}$. 69
11.4 Comparison of Energy Calibration curves. 70
11.5 Results for combined energy calibration 71
11.6 Curve of the iron-55 source from a single pixel with s-curve fit (pixel 4-10). 72
11.7 Distribution of determined signal heights for iron-55 with Gaussian fit 73

13.1 Exemplary pre-fit for copper. 82
13.2 Energy dependency of free mean path in silicon 83

14.2 List of Tables

9.1 Table with results from Gaussian fit of results distribution from single pixels. 58

10.1 Table with results of single pixel distributions 66

11.1 Table with results from Gaussian fit of results distribution from single pixels for the combined calibration. 71
11.2 Overview of results for total sensor 73

13.1 Physical Attributes of Silicon [25], [38], [41], [42], [43], [44] 80
13.2 Overview of pixel bias voltages taken from [45] 80
13.3 Overview of periphery bias voltages taken from [45] 81
13.4 DAC-Settings for MuPix 7224, also reffered as LMPS and additional settings 81
13.5 Materials for X-ray fluorescence available in this thesis with data from [39] 82

BR Branching Ratio 11

CL Confidence Level 10

cLFV charged Lepton Flavor Violating Decay 10

CSA Charge Sensitive Amplifier 30

GUI Graphical User Interface 34

FPGA Field Programmable Gate Array 31

HiMB High intensity Muon Beamline 15

HSMC High Speed Mezzanine Card 34

HV-MAPS High Voltage Monolithic Active Pixel Sensor 3

LMPS Low-Medium-Power Settings

MIP Minium Ionizing Particle 19

PCB Printed Circuit Board 34

PLL Phase Locked Loop 31

PSI Paul Scherer Institut 10

RAM Random Access Memory 34

SF Source Follower 30

SM Standard Model of Particle Physics 10

SNR Signal to Noise Ratio 42

ToT Time-over-Threshold 31

VCO Voltage Controlled Oscillator 31

XRF X-ray Fluorescence 43

Acknowledgments

At the end I would like to thank everyone who supported me during my physics studies and this thesis.

In the first place i want to thank Prof. Dr. Andrè Schöning for offering me the opportunity to work and carrying out this thesis within the Mu3e experiment. Also I want to thank Prof. Dr. Norbert Herrmann for being my second examiner and reading my thesis.
Furthermore, a big thank-you for all the Mu3e members for the great, funny and informative time I had with them. During my stay I learned a lot and got first insights in scientific work, but also had several funny football table matches and barbecue evenings. In this case special thanks to

- Lennart Huth for all the time he patiently sacrificed to help me with programming and physics related questions and problems i got stuck with.
- Heiko Augustin for sharing a lot of his knowledge over the MuPix and giving new ideas and constructive suggestions for measurements
- Jan Hammerich for great discussions and his help at single setup, MuPix and ROOT related stuff.

Additionally i want to thank the following people, which have taken their time to read my thesis and gave me correction hints: Lennart Huth, Jan Hammerich, Oliver Drozdowski, Sven Fabian, Heiko Augustin and Sebastian Dittmeier.
Last but not least, i would like to thank my parents, family and friends for supporting me all the time during my studies and keeping me motivated in stressful situations. Without their support I wouldn't have come this far.

Erklärung:

Ich versichere, dass ich diese Arbeit selbstständig verfasst habe und keine anderen als die angegebenen Quellen und Hilfsmittel benutzt habe.

Heidelberg, den (Datum) .....